Master Thesis

Hardware Characterisation for the Construction of a Compton Camera Prototype

Masterarbeit

zur Erlangung des akademischen Grades Master of Science (M.Sc)

eingereicht bei der Naturwissenschaftlich-Technischen Fakultät

Naturwissenschaftlich-
Technische Fakultät

der Universität Siegen

Author:	Lars Maczey
	1742910
Date of submission:	28.03.2025
1st Supervisor:	Prof. Dr. Ivor Fleck
2nd Supervisor:	PD Dr. Carmen Diez Pardos

Siegen, March 27, 2025

Abstract

Radioactive tracers are often used in non-invasive diagnostic tests or medical studies to analyse functional aspects of an organ. These tracers contain unstable isotopes that decay and produce high energetic photons. A detection of these photons gives rise to an imaging of the temporal and spacial distribution of the tracers within the body. Existing detection technologies to date can only allow effective an imaging for photon energies up to 1 MeV. The Compton camera under construction at the University of Siegen aims to overcome the current limitation in medical imaging and open up an imaging for photon energies above 1 MeV. It has the potential to give rise to many new possible fields of study and improve the diagnosis and treatment of diseases in medicine. The novel approach is to track the electron of a Compton scattering process by its production of Cherenkov photons.

To meet the demands of such a Compton camera, many hardware component have to be characterised and different products have to be compared. Within the scope of this thesis, different silicon photomultipliers (SiPMs) as well as scintillators are investigated intensively to evaluate their potential use for the construction of a Compton camera prototype and parameters for the operation of the SiPMs and their readout systems are optimized.

Contents

List of Abbreviations

ADC   analogue-to-digital converter

APD   avalanche photodiode

ASIC   application-specific integrated circuit

CTP   cross talk probability

CTR   coincidence time resolution

CDF   cumulative distribution function

DAC   digital-to-analog converter

DCR   dark count rate

DOI   depth of interaction

ETCC   electron tracking Compton camera

FPGA   field programmable gate array

FWHM   full width at half maximum

GAGG   Gadolinium Aluminium Gallium Garnet $Gd_3Al_2Ga_2O_{12}$

GbE   gigabit ethernet

GUI   graphical user interface

KLauS   *Kanäle für die **La**dungs**au**slese von **S**ilizium-Photomultipliern*

LAN   local area network

LED   light-emitting diode

LGSO   Lutetium Gadolinium Oxyorthosilicate $Lu_{2-x}Gd_xSiO_5$

LSB   least significant bit

LYSO   Lutetium Yttrium Oxyorthosilicate $Lu_{2(1-x)}Y_{2x}SiO_5$

MCX   micro coaxial

MIP   minimum ionizing particle

NUV   near UV

PDE   photon detection efficiency

PDF   probability density function

p.e.   photon equivalent

PET   positron emission tomography

PHR   pulse height ratio

PMMA Polymethylmethacrylat

PMT   photomultiplier tube

PTFE   polytetrafluoroethylene

QDC   charge-to-digital converter

RMS   root mean square

SCoKa *Siegener Compton-Kamera*

SiPM   silicon photomultiplier

SMA   subminiature version A

SNR   signal-to-noise ratio

SOI   silicon-on-insulator

SPAD   single photon avalanche diode

SPECT single photon emission computed tomography

TDC   time-to-digital converter

TIA   transimpedance amplifier

ToA   time-of-arrival

ToF   time-of-flight

ToT   time-over-threshold

TPC   time projection chamber

USB   universal serial bus

UV   ultraviolet

1 | Introduction

Imaging of high energetic gamma radiation is of great interest not just as part of medical examinations for diagnostic purposes but also in medical and biological research. A widely used method is to inject radioactive tracers into patient containing unstable isotopes that emit gamma radiation when decaying. These tracers can be e.g. sugar complexes that accumulate in cancer tissue and thus enable a localisation of the cancer. To date, existing detection technologies can only enable effective imaging for energies up to 1 MeV. Consequently, radioactive tracers can only resort to the use of isotopes with gamma radiation below this energy. This limitation is to be overcome with the planned Compton camera that shapes the focus of this thesis. The goal of this thesis is to present characterisation measurements of hardware components that are needed for the construction of a Compton camera prototype and identify suitable products as well as challenges that need to be managed in the future.

In chapter 2, the theoretical background is established to lay a foundation of physical concepts and detector technologies that are necessary for this thesis. Chapter 3 aims to motivate the Compton camera project and the measurements presented in this thesis. The characterisation measurements and their results are explained in two chapters, with chapter 4 focusing on SiPM measurements and chapter 5 focusing on measurements with scintillators.

Well-established imaging methods such as positron emission tomography (PET) and single photon emission computed tomography (SPECT) are explained in chapter 3. To overcome the current limitation in medical imaging, the concept of a Compton camera is introduced and a selection of already existing Compton camera prototypes is presented. Their performance and why existing prototypes fail to open up an imaging above 1 MeV are discussed. Building on this, the Compton camera project at the University of Siegen in the context of which this thesis was written is explained as well as its significance in a medical context.

In chapter 4, the four different SiPM products available for this thesis are compared extensively. Two different readout methods are introduced, one relying on a data acquisition with an oscilloscope and an offline analysis, the other performs an online charge integration using the TOFPET ASIC from PETsys Electronics. Noise characteristics of the SiPMs are investigated intensively by evaluating charge histograms, inter-time distributions and staircase plots. The operating bias voltage of the SiPMs is optimised regarding its future application in the Compton camera prototype. The influence of certain parameters of the TOFPET ASIC is discussed in this chapter as well.

The scintillators are characterised in chapter 5 by recording spectra of different radioactive sources. Thus firstly, the sources available are examined and their most intense radiation lines are identified in order to understand the recorded source spectra. Comparative measurements between the three available scintillators are discussed for their most important properties. With regard to their future use in the Compton camera, exemplary energy calibrations are performed and the saturation behaviour of the detection system is investigated. The spreading of light signals over multiple SiPMs and measurements of the depth of interaction (DOI) are presented as well.

A conclusive summary of the findings of this thesis is presented at the end in chapter 6.

2 | Theoretical Background

In this chapter, a theoretical foundation of physical concepts and detector technologies is established. For the scope of this thesis, it is necessary to consider interaction processes of photons and charged particles in matter, because they determine the fundamental principles on which detection mechanisms are built.

A Compton camera is essentially a gamma ray detector, thus photon interactions with matter are discussed first. Interactions of charged particles, such as electrons, play a crucial role in relevant detection principles as well. Silicon photomultipliers (SiPMs) are the most frequently used detector technology in this thesis. Their working principle and characteristics will be introduced extensively in this chapter. Scintillators and the physical concepts of their detection mechanism are then discussed as another important method of particle detection. Lastly, the SiPM readout system that is used for the majority of the measurements presented in this thesis is introduced.

2.1 Photon Interactions with Matter

The most relevant interaction processes of photons with matter that are discussed in the scope of this thesis are:

- Photoelectric effect

- Compton effect

- Pair production

The photoelectric effect and pair production are absorption processes. The Compton effect is a scattering process. Unlike charged particles (see section 2.2), it is not possible to define a range of a gamma beam, since all of the listed interactions are statistical processes. Instead, a gamma ray is attenuated exponentially while traversing through matter

$$I(x) = I_0 \cdot e^{-\mu_{\text{att}} x}, \tag{2.1}$$

where μ_{att} is the mass attenuation coefficient and x is the depth [1]. The mass attenuation coefficient is defined as

$$\mu_{\text{att}} = \frac{N_A}{A} \sum_i \sigma_i, \tag{2.2}$$

where N_A is the Avogadro constant, A the atomic mass number and σ_i the cross section of the process i.

The total cross section $\sigma_{\text{tot}} = \sum_i \sigma_i$ together with different partial cross sections σ_i are displayed in figure 2.1 for different photon energies in tungsten. The different processes will be discussed in more detail in the following subsections.

Which fo these processes is dominant depends on the photon energy E_γ but also on the atomic number Z of the material that is traversed. The ranges in which the different interaction processes dominate are highlighted in figure 2.2.
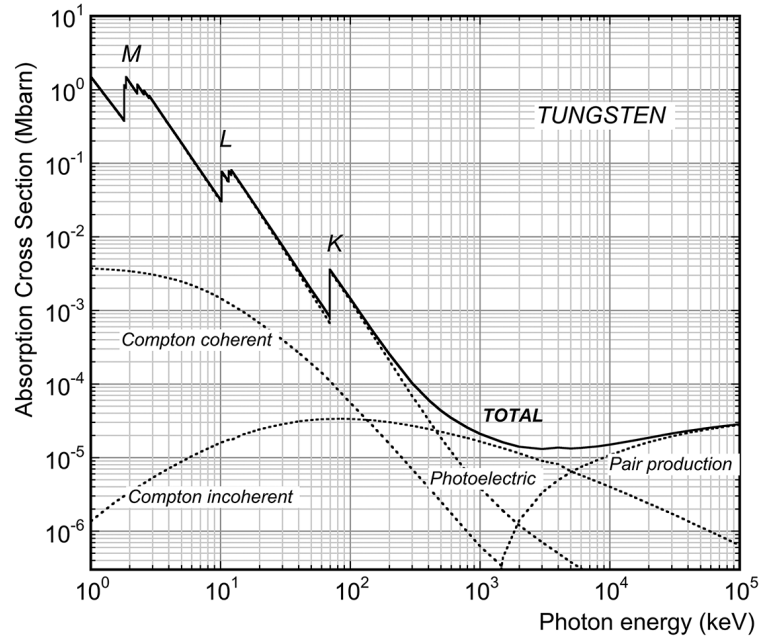
Figure 2.1: Total cross section for a photon that is traversing tungsten at different photon energies [2, p. 47].

2.1.1 Photoelectric Effect

The photoelectric effect describes the absorption of a photon by an atom. The photon transfers all its energy to an electron that is bound in the atomic shell. Due to momentum conservation, this is not possible for a free electron, but a nucleus is needed to take the recoil. After the photon absorption, the electron is released from the atom with the energy

$$E_e = E_\gamma - E_{\text{binding}}, \tag{2.3}$$

where E_{binding} is the binding energy. The atom is consequently ionised after this process [3].

The cross section of the photoelectric effect $\sigma_{\text{p.e.}}$ depends on the shell in which the electron is bound. Generally, the closer the electron is to the nucleus the more likely is the interaction, i.e. electrons in the K-shell have the highest interaction probability [1]. On the other hand, the binding energy E_{binding} is higher for shells closer to the nucleus such that higher photon energies are needed, since due to equation (2.3) the interaction can only take place if $E_\gamma > E_{\text{binding}}$. As a consequence, sharp edges are visible in the total cross section displayed in figure 2.1, because the cross section of the photoelectric effect rises rapidly when the photon energy exceeds the binding energy of an atomic shell.

In addition, the cross section $\sigma_{\text{p.e.}}$ has a strong dependence on both the photon energy E_γ and the atomic number Z of the target material. This dependency can be approximated with [3]:

$$\sigma_{\text{p.e.}} \sim \frac{Z^5}{E_\gamma^{3.5}} \tag{2.4}$$

The photoelectric effect can lead to secondary processes. The emitted electron may leave a hole in the atomic shell which can be filled up by an electron from an outer shell. The energy difference between the binding energies of these shells is emitted in the form of a photon which is typically in the X-ray range. This secondary photon might even interact with another electron of the same atom, e.g. in the L-shell. This second emitted electron is then called Auger electron [1].

2.1.2 Compton Scattering

The Compton effect is a scattering process that takes usually place between a photon and an electron. The electron can be regarded as quasi-free, i.e. its binding energy can be neglected due to $E_\gamma \gg E_{\text{binding}}$. In a coherent Compton scattering process, the electron is not transferred any energy by the photon. Thus, the
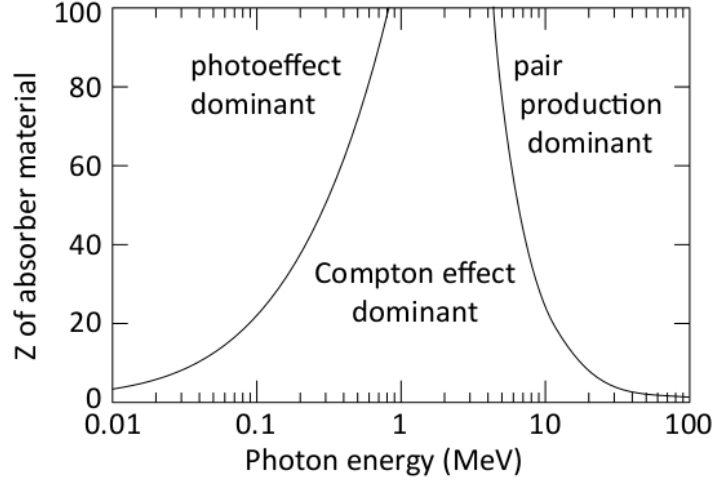
3

Figure 2.2: Dominant photon interaction processes for different photon energy E_γ and atomic number Z [3, p. 86].

electron remains in its atomic shell and the atom takes the recoil. The photon hardly loses any energy in this process but changes its direction [3]. The more relevant process in the scope of this thesis however is incoherent Compton scattering, where the photon with an initial energy of E_γ transfers a part of its energy to the electron, which then has the energy E'_e and is released from the atom (illustrated in figure 2.3). Unless stated otherwise, a Compton scattering is always assumed to be incoherent in this thesis.
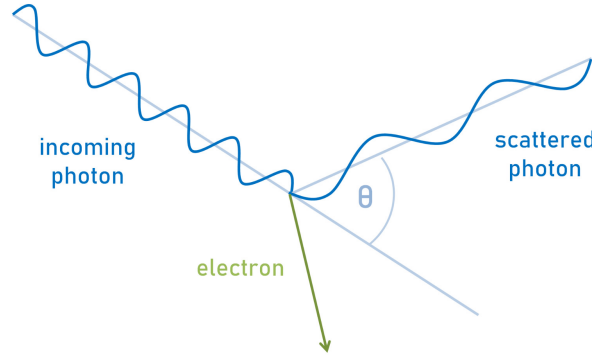
Figure 2.3: Schematic of an (incoherent) Compton scattering process.

In the Compton scattering process, the photon is scattered under an angle θ. Let $P_\gamma = (E_\gamma, \vec{k})$ be the four-momentum vector of the initial photon. Analogously, the four-momentum vector of the scattered photon is $P'_\gamma = (E'_\gamma, \vec{k}')$. The electron is assumed to be initially at rest with $P_e = (m_e, \vec{0})$ and then scattered with $P'_e = (E'_e, \vec{p_e}')$. Imposing energy-momentum conservation leads to:

$$P_\gamma + P_e = P'_\gamma + P'_e \tag{2.5}$$

$$\Leftrightarrow \quad (P_\gamma - P'_\gamma)^2 = (P'_e - P_e)^2 \tag{2.6}$$

$$\Leftrightarrow \quad P_\gamma^2 + P'^2_\gamma - 2P_\gamma P'_\gamma = P'^2_e + P_e^2 - 2P'_e P_e \tag{2.7}$$

Using $P_\gamma^2 = P'^2_\gamma = 0$ and $P_e^2 = P'^2_e = m_e^2$:

$$\Rightarrow \quad -P_\gamma P'_\gamma = m_e^2 - P'_e P_e \tag{2.8}$$

$$\Rightarrow \quad -E_\gamma E'_\gamma + \vec{k} \cdot \vec{k}' = m_e^2 - E'_e m_e = m_e(E'_e - m_e) \tag{2.9}$$

The scalar product can be expressed as $\vec{k} \cdot \vec{k}' = |\vec{k}||\vec{k}'| \cdot \cos\theta = E_\gamma E'_\gamma \cdot \cos\theta$ and together with energy

4

conservation $E_\gamma + m_e = E'_\gamma + E'_e \Rightarrow E'_e - m_e = E_\gamma - E'_\gamma$, equation (2.9) can be rewritten as:

$$E_\gamma E'_\gamma (1 - \cos\theta) = m_e(E_\gamma - E'_\gamma) \tag{2.10}$$

which can be rewritten in the form of the Compton scattering formula:

$$\Rightarrow \quad E_{\gamma'} = \frac{E_\gamma}{1 + \frac{E_\gamma}{m_e}(1 - \cos\theta)} \tag{2.11}$$

Thus, the E_γ and E'_γ are related by the electron energy due to energy conservation

$$E_{\gamma'} = E_\gamma + m_e - E'_e \tag{2.12}$$

and by the scattering angle θ as described in equation (2.11).

The differential cross section of the Compton scattering process is known as the Klein-Nishina equation

$$\frac{\mathrm{d}\sigma_C}{\mathrm{d}\Omega} = \frac{r_e^2}{2\left(1 + \epsilon(1 - \cos\theta)\right)^2}\left(1 + \cos^2\theta + \frac{\epsilon^2(1 - \cos\theta)^2}{1 + \epsilon(1 - \cos\theta)}\right), \tag{2.13}$$

where $\epsilon = \frac{E_\gamma}{m_e}$ is the reduced energy [3]. A polar representation of this equation is displayed in figure 2.4. For lower reduced energies ϵ, backscattering ($\theta \approx 180°$) and forward scattering ($\theta \approx 0°$) have a similar probability to occur. With increasing ϵ, forward scattering becomes more likely over backscattering. Due to $\sigma_C^{\mathrm{atom}} = Z \cdot \sigma_C$:

$$\sigma_C^{\mathrm{atom}} \sim \frac{Z}{E_\gamma} \tag{2.14}$$
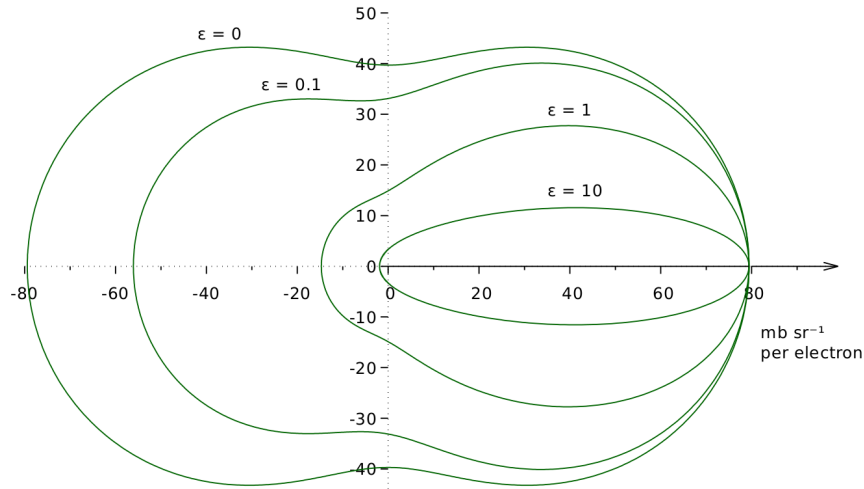
Figure 2.4: The Klein-Nishina formula for the differential cross section of Compton scattering in a polar representation [4, p. 42].

2.1.3 Pair Production

A photon can produce a particle-antiparticle pair in the coulomb field of a charge with mass M_{coulomb}. The charge is needed to take the recoil, since the process would otherwise violate momentum conservation. Let m_p be the mass of the created particle / anti-particle. The pair production process is only possible if the energy threshold condition

$$E_\gamma \geq 2m_p + \frac{2m_p^2}{M_{\mathrm{Coulomb}}} \tag{2.15}$$

5

is fulfilled [1]. The lightest particle-antiparticle pair that can be created is an electron-positron pair. While traversing through matter, a photon encounters Coulomb fields that are created by the nuclei of atoms. Since $m_e \ll M_{\text{nucleus}}$, equation (2.15) can be approximately simplified to:

$$E_\gamma \gtrsim 2m_e \approx 1\,\text{MeV} \tag{2.16}$$

The cross section of the pair production approximately scales with [1]:

$$\sigma_{\text{pair}} \sim Z^2 E_\gamma \tag{2.17}$$

2.2 Interactions of Charged Particles with Matter

The interactions of charged particles (such as electrons) with matter are exploited in many detectors. They also play a crucial role in the working principle of detectors used in this thesis (e.g. scintillators). In addition, photons are often not detected directly but through a secondary particle, e.g. through an electron that has interacted with the photon via photoelectric effect or Compton scattering. Thus, interactions of charged particles provide relevant fundamental concepts for this thesis.

2.2.1 Ionisation

A charged particle that is passing through matter constantly loses energy through interactions with the atoms of the material. The charged particle can excite the atoms or strip away an shell electron (impact ionisation) leaving behind an ion. For heavy particles (with a mass $M_{\text{particle}} \gg m_e$), the average energy loss due to these processes is described by the Bethe-Bloch equation

$$-\frac{\mathrm{d}E}{\mathrm{d}x} = 4\pi N_A r_e^2 m_e z^2 \frac{Z}{A} \frac{1}{\beta^2} \Big(\ln \frac{2m_e \gamma^2 \beta^2}{I} - \beta^2 - \frac{\delta}{2} \Big), \tag{2.18}$$

where z is the charge of the incident particle, r_e is the classical electron radius, N_A the Avogadro constant, I the mean excitation energy of the absorber material and δ a parameter for the description of the reduced energy loss due to the density effect [1]. A graphical representation of this equation can be seen in figure 2.5. The minimum around $\beta\gamma \approx 3$ corresponds to the so-called minimum ionizing particle (MIP). For momenta below the minimum, the energy loss behaves approximately according to $-\frac{\mathrm{d}E}{\mathrm{d}x} \sim \frac{1}{\beta^2}$. Above the minimum, the energy loss is plateauing with $-\frac{\mathrm{d}E}{\mathrm{d}x} \sim \ln\gamma$.

For electrons however, the Bethe-Bloch equation is not accurately describing the energy loss due to ionisation, since for electrons some processes are relevant that do not contribute to the energy loss of heavier charged particles. While traversing matter, electrons interact mostly with other electrons, which means that there are interference effects and spin configurations play a role [3]. The mean energy loss as a function of the momentum for various charged particles can be seen in figure 2.6. The functions are shifted due to the different mass of the particles. The minimum of the electron's mean energy loss is reached at very low energies outside of the scale of the plot in figure 2.6.

Since a charged particle constantly loses energy while passing through matter, it has a specific range R it can reach. The value of this range R has only a small dispersion, thus a beam of charged particles abruptly stops at a certain depth in the material. The particles lose a lot of energy over a relatively small distance at the end of their path due to the $\frac{1}{\beta^2}$ shape of the Bethe-Bloch function. This results in a peak of the energy loss which is called the *Bragg peak* as it can be seen in figure 2.7 [3].

This characteristic of charged particle beams is exploited in e.g. proton therapy.

2.2.2 Bremsstrahlung

Fast charged particles are decelerated by the Coulomb field of nuclei. The lost kinetic energy is emitted in the form of photons. This effect is called Bremsstrahlung. The energy loss due to Bremsstrahlung is proportional to [1]:

$$-\frac{\mathrm{d}E}{\mathrm{d}x} \sim Z^2 \frac{E}{m_p^2} \tag{2.19}$$

Figure 2.5: The mean energy loss of a charged particle by ionisation as described by the Bethe-Bloch equation [3, p. 39].

Because of the $1/m_p^2$ dependency, Bremsstrahlung is most relevant for light particles such as electrons. The *critical energy* E_C is defined as the energy at which the energy loss of the particle due to Bremsstrahlung becomes bigger than the energy loss due to ionisation.

The energy of the particle that is radiating Bremsstrahlung is decreasing exponentially with:

$$E(x) = E_0 e^{-\frac{x}{X_0}} \tag{2.20}$$

Here, X_0 is the so-called *radiation length*. After $1X_0$, the particle has lost $1 - \frac{1}{e} \approx 63\%$ of its energy.

2.2.3 Multiple Scattering

While passing through matter, a charged particle is scattered by the Coulomb fields created by nuclei and electrons. These scattering processes lead to small deviations from the original path. Since the particle is deflected multiple consecutive times, these deviations add up to a projected scattering angle $\theta(x)$ at depth x. The root mean square (RMS) of this angle is [1]:

$$\theta_{\mathrm{RMS}}(x) = \frac{13.6\,\mathrm{MeV}}{\beta c p} z \sqrt{\frac{x}{X_0}} \left[1 + 0.038 \ln\left(\frac{x}{X_0}\right) \right] \tag{2.21}$$

Here, z is the charge of the scattered particle and X_0 is the radiation length.

2.2.4 Cherenkov Radiation

Cherenkov radiation is emitted when a particle is traversing through a medium faster than the speed of light in this medium. Thus, there is the threshold condition

$$v > \frac{c}{n}, \tag{2.22}$$

where c is the speed of light in vacuum, n is the refractive index of the medium and $v = \beta \cdot c$ is the velocity of the particle. The effect occurs because charged particles polarise atoms along their track and hence create electric dipoles. For $v < \frac{c}{n}$, the dipoles are symmetrically arranged along the track, hence the dipole fields cancel each other. But for $v > \frac{c}{n}$, the dipoles are no longer symmetrically arranged such that there is a non-vanishing dipole moment, which leads to the emission of photons. This effect is illustrated in figure 2.8 [1].
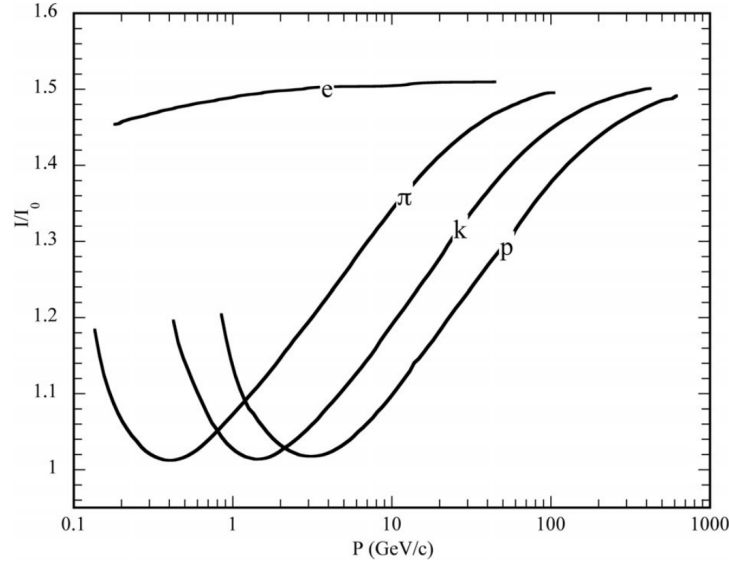
7

Figure 2.6: The mean energy loss of various charged particles against their momentum [2, p. 32].
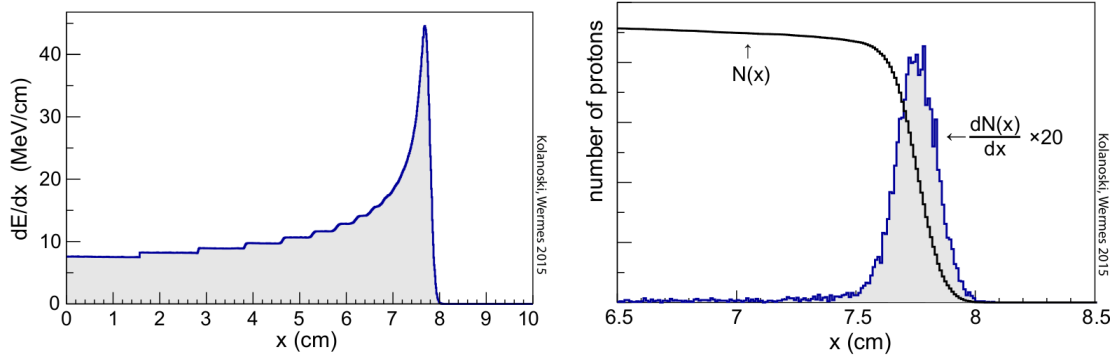

Figure 2.7: Left: Energy loss as a function of the depth x. The Bragg peak is visible at the range R. Right: Number of remaining charged particle beams in a particle beams as a function of the depth x. The number abruptly drops at $x = R$. Both pictures taken from [3, p. 49].

These Cherenkov photons are emitted under an angle φ that depends on the velocity of the particle[1]:

$$\cos(\varphi) = \frac{1}{n\beta} \tag{2.23}$$

Thus, the faster a particle the larger the emission angle φ of the Cherenkov photons [3]. The maximum Cherenkov angle $\varphi_{\max}$ is reached for $\beta = 1$ with $\cos \varphi_{\max} = \frac{1}{n}$.

The number of Cherenkov photons per unit path length can be determined with

$$\frac{\mathrm{d}N}{\mathrm{d}x} = 2\pi\alpha z^2 \int_{\lambda_1}^{\lambda_2} \left(1 - \frac{1}{n^2(\lambda)\beta^2}\right)\frac{\mathrm{d}\lambda}{\lambda^2}, \tag{2.24}$$

where z is the charge of the Cherenkov radiation producing particle, λ_1 and λ_2 are the wavelengths in between which the photons are emitted and α is the fine-structure constant [1]. Most emitted photons have small wavelengths in the ultraviolet (UV) range (see figure 2.9). Cherenkov photons do not reach wavelengths in the X-ray range because of $n(\lambda_{\text{X-ray}}) = 1$.

---

[1]This equation neglects the recoil of the Cherenkov photons on the incident particle, which, however, only makes a very small contribution.
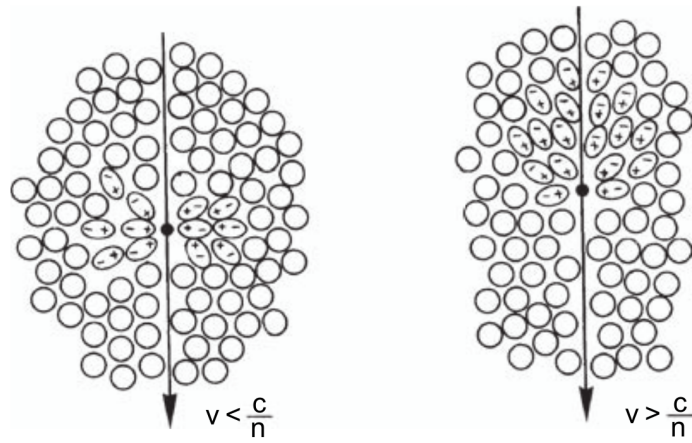
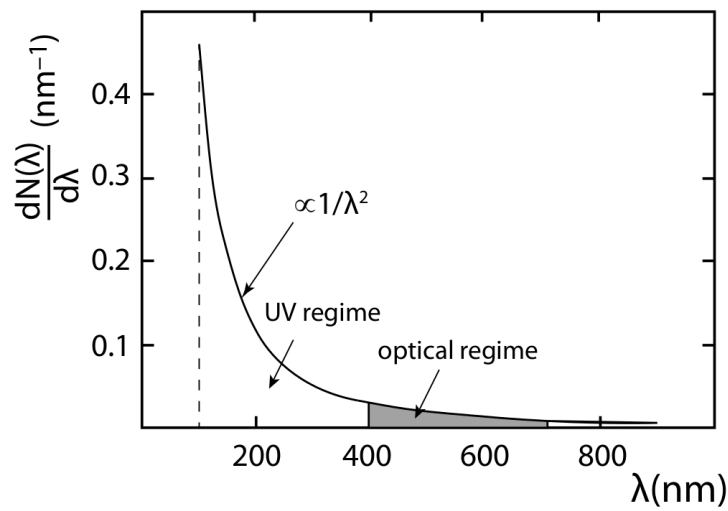**Figure 2.8:** Schematic illustration of the Cherenkov effect [1].

Figure 2.9: Schematic of the wavelength dependence of Cherenkov radiation [3].

2.3 Silicon Photomultipliers

Silicon photomultipliers (SiPMs) are light detection devices. The detection principle is based on a photo diode, which is like every diode a junction of p- and n-doped semiconducting material. The diode is operated with reversed bias, where the depletion region is used as sensitive detector material. For a PIN photodiode, the depletion zone can reach a width of about $350\,\mu m$ [1]. A photon may create an electron-hole pair in this zone. The charge carriers are then separated and drifted towards the electrodes, where they contribute to an electric signal that can be read out.

The speed with which the electrons and holes are collected depends on the applied bias voltage. If the bias voltage is increased large enough, the electrons are accelerated to such an extent that they can create further electron-hole pairs by impact ionisation. The secondary created electrons are consequently accelerated as well and may produce further charge carriers. Thus a photon can create an avalanche of electron-hole pairs. These types of photodiodes are called avalanche photodiodes (APDs). They have an intrinsic gain mechanism and are capable of detecting weak light signals that consist of 10-20 photons [5].

Increasing the bias voltage even more above the breakdown voltage of the diode will accelerate even the holes fast enough for them to create secondary electron-hole pairs. In this operation mode, the avalanche in the diode would not stop on its own, which is why these diodes are combined with quenching resistors, such that the diode can recharge itself after some time. In this detection device, an avalanche is triggered as soon as a single photon creates an electron-hole pair, which means that it is a solely binary detection process. The

9

same avalanche is triggered regardless of how many photons impinged on the detection material. For that reason, this type of diode is called a Geiger-mode APD or single photon avalanche diode (SPAD), since it is capable of detecting single photons.
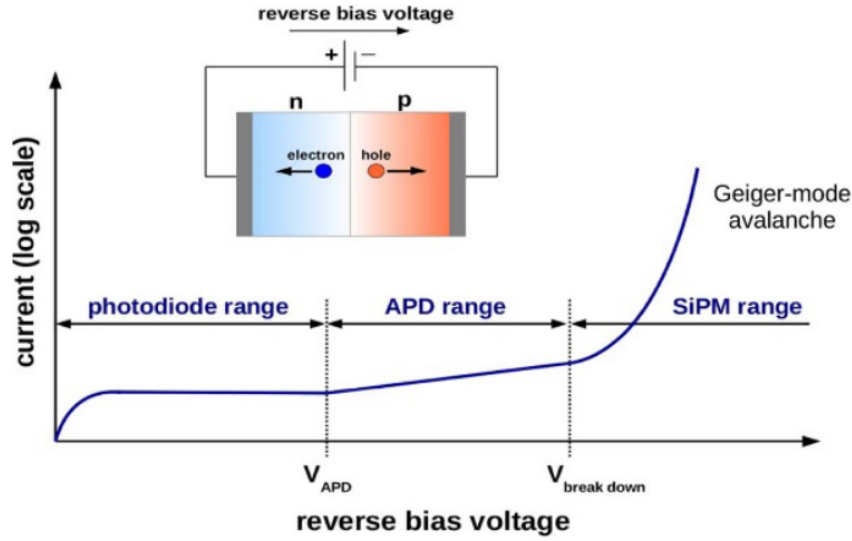

Figure 2.10: Operation regimes of the applied bias voltage for the different diodes for light detection [6, p. 3].

A Geiger-mode APD can only give information about the fact, that one or multiple photons have been detected but not how many. In order to get an information about the number of photons, these Geiger-mode APDs are arranged in a matrix structure. This is the concept of a SiPM. A SiPM has a certain number of microcells (usually several thousands), where each microcell consists of a SPAD together with a quenching resistor. An equivalent circuit of a basic SiPM design as well as a schematic drawing can be found in figure 2.11.
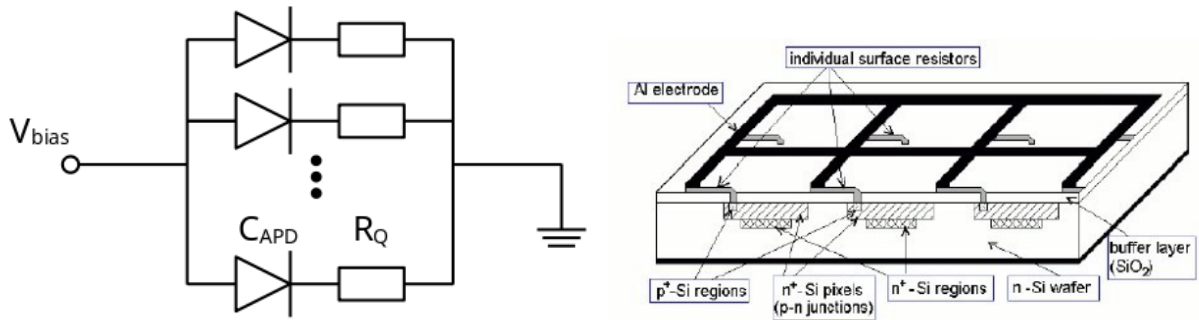
Figure 2.11: Left: Equivalent circuit of the basic design of a SiPM with APD and quenching resistor. Right: Schematic design of multiple APD microcells forming a SiPM [5, p. 22].

The quenching resistor causes the avalanche to stop, since the APD itself is a capacitance C_{APD} that forms an RC circuit together with the quenching resistor R_Q. The recovery time of the SiPM is determined by the time constant of this RC circuit:

$$\tau_{\text{rec}} = R_Q \cdot C_{APD} \tag{2.25}$$

Each microcell produces the same output signal in case they detect a photon. In case the SiPM detects n photons in total, the output signal of the SiPM is the sum of the signal of n microcells. Thus, a SiPM produces only output signals with a discrete pulse height, which means on the other hand, that a specific pulse height corresponds to a certain photon number. One can perform an integration over the SiPM output signal, which corresponds to the charge deposited in the diode, which linearly depends on the detected

photon number. The amplitude, that corresponds to one detected photon, is called the 1 photon equivalent (p.e.) amplitude, while two detected photons can induce a waveform with a 2p.e. amplitude and so on. The discrete nature of the SiPM signals can be observed in the screenshot of an oscilloscope measurement in persistence mode in figure 2.12.
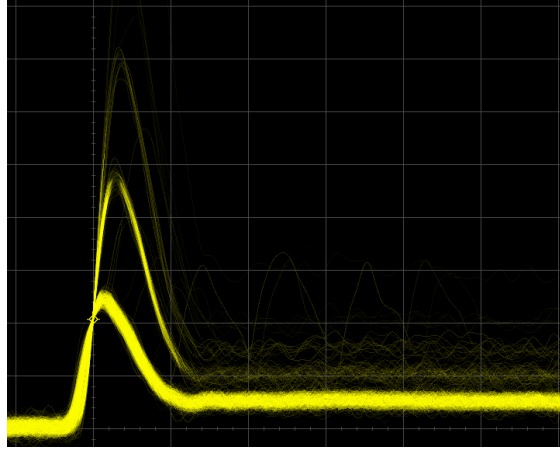

Figure 2.12: Screenshot of an oscilloscope measurement. The discrete peak heights of the SiPM signals is visible.

2.3.1 Dark Count

An electron may reach the valence band of the semiconducting material simply by thermal excitation. These thermally induced noise events are not distinguishable from an actual detection of a photon. Consequently, the SiPM also gives output signals even when the SiPM is covered in complete darkness. These events are called dark counts and the rate at which they appear is called dark count rate (DCR). The DCR depends strongly on the temperature of the SiPM and also increases linearly with the overvoltage [7], which is the difference between the applied bias voltage and the breakdown voltage.

$$V_{\text{ov}} = V_{\text{bias}} - V_{\text{bd}} \tag{2.26}$$

2.3.2 Optical Cross Talk

While an avalanche is ongoing in an APD, a photon can be created in the avalanche process and escape the microcell. These photons originate from Bremsstrahlung or inter- and intra-band transitions and can propagate to adjacent cells either on a direct path or through reflections. When reaching a neighbouring APD, they may trigger an avalanche and induce a signal. This process happens on a time scale below a few ps, which means that the primary and the secondary cell simultaneously output a signal. Thus, cross talk is a correlated noise source, because it occurs in correlation to a dark count event or an actual photon detection. The probability that a primary event induces a secondary event through cross talk is called the cross talk probability (CTP). It can be reduced by inserting trenches between individual cells. The CTP has a quadratic dependence on the overvoltage [7].

2.3.3 Afterpulses

Some electrons in an avalanche may fall into a trap state due to e.g. impurities in the material. The charge carrier gets released from this trap after some time and is then capable of triggering a new avalanche. The amplitude of this secondary signal depends on the time difference t between the first avalanche and the release from the trap state

$$Q_{\text{AP}} = Q_{\text{1p.e.}} \cdot \left(1 - e^{-\frac{t}{\tau_{\text{rec}}}}\right), \tag{2.27}$$

where τ_{rec} is the recovery time constant [8]. If the charge carrier is released sufficiently late enough, the output signal induced by this afterpulse is not distinguishable from a dark count event or an actual photon

detection any more. Afterpulses are a correlated noise source just as cross talk events. A comparison between the waveform shapes of the various noise contributions in a SiPM is illustrated in figure 2.13.
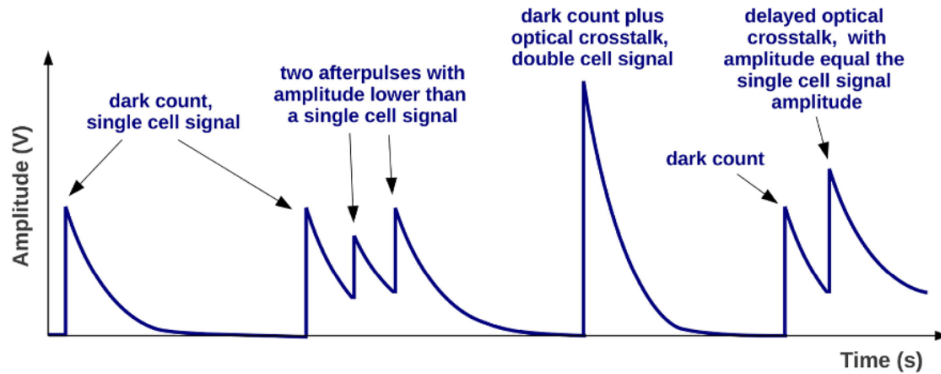

Figure 2.13: Illustrative comparison between waveforms of different noise contributions of a SiPM [6, p. 10].

2.3.4 Photon Detection Efficiency

The photon detection efficiency (PDE) is defined as:

$$\text{PDE} = \frac{\text{\# detected photons}}{\text{\# impinging photons}} \tag{2.28}$$

It depends on the quantum efficiency $\text{QE}(\lambda)$, the probability $p_A(V_{\text{over}})$ that an avalanche is triggered in case that an electron-hole pair is created and the fill factor ϵ_{fill}, which is the fraction of the detector's front face that is sensitive:

$$\text{PDE} = \text{QE}(\lambda) \cdot p_A(V_{\text{over}}) \cdot \epsilon_{\text{fill}} \tag{2.29}$$

2.3.5 Dynamic Range

The dynamic range of the SiPM depends on the number of microcells available and on the probability that two photons hit the same cell. Naturally, a SiPM cannot detect more photons than it has microcells at once. For light pulses, which have an amount of photons that is close to the number of SPADs, there is a saturation effect in the response of the SiPM. This effect is captured in the following exponential function [6]:

$$N_{\text{fired}} = N_{\text{SPADs}} \cdot \left(1 - e^{-\frac{N_{\text{photons}} \cdot \text{PDE}}{N_{\text{SPADs}}}} \right) \tag{2.30}$$

This exponential behaviour of SiPMs towards large photon numbers can be observed in figure 2.14. For small light signals, the SiPM response can be approximated well with a linear function.

2.4 Scintillators

Scintillators are one of the oldest types of detectors used for particle detection. The detection principle is based on the *scintillation* process, where the energy loss of an impinging particle leads to an excitation of the scintillator material. The de-excitation of the material causes a light emission with a characteristic spectrum, usually in the range of visible light. Thus, a scintillator can convert the deposited energy of an incident particle in an (optical) light signal. Important characteristics of a scintillator are:

- **Scintillation efficiency:** The ratio of the energy of incident photon to the absorbed energy in the scintillator material.

- **Light output:** The number of photons emitted per unit energy deposited in the scintillation material.
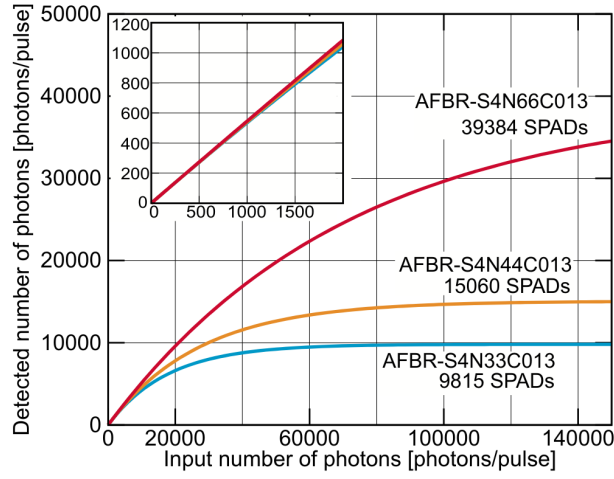
Figure 2.14: The saturation behaviour of various Broadcom SiPMs with different number of SPADs [9].

- **Emission spectrum:** The wavelengths of the emitted photons.

- **Decay time of the scintillator:** The material is excited through the energy loss of the impinging particle. This excited state has a certain decay time τ_D and scintillation photons are created on the de-excitation.

The light signal of a scintillator consists of a fast rise followed by a slower exponential decay that is characterised by the decay time τ_D. In some scintillators, there are multiple excitation states with different decay times leading to a multi-component exponential light signal [1].

There are organic and inorganic scintillators. Organic scintillators are polymerised liquids or plastics, where the scintillation mechanism is based on the electron structure of carbon atoms. Inorganic scintillators are mostly crystals, that are often doped with small amounts of other materials [1].

In the scope of this thesis, only inorganic scintillators are relevant, since they show generally better characteristics for the intended purpose in a Compton camera where scintillators will be used for a photon energy measurement. The light output is higher leading to a better energy resolution and inorganic crystals can be very dense such that the absorption cross section and thus the detector efficiency is larger.

2.4.1 Inorganic Scintillators

The scintillation mechanism of inorganic scintillators is based on the energy band structure of the crystal lattice. Inorganic scintillator crystals are insulators with a valence band that is completely filled with electrons and an electron-free conduction band. The band gap is in the range of 4 eV to 12 eV [3]. When an incident particle is depositing energy into the lattice, electrons from the valence band are lifted into the conduction band where they can move freely through the lattice and vacancy spots (*holes*) remain in the valence band which can be treated as free and positive charge carries.

The electrons and holes can recombine under the emission of photons which have the same energy as the band gap E_g which is usually outside the visible range [3]. On the other hand, an electron and a hole can also form a bound state, which acts like a quasi-particle that is called exciton. The energy level V_{ex} of this exciton bound state is slightly below the conduction band. Thus when recombining, a photon with $E_\gamma = V_{ex}$ is emitted. However, the probability for recombination is very low at room temperatures [1].

The crystal lattice is often doped with impurities in order to improve the scintillation efficiency. Additional energy levels V_{dop} are hereby created in-between the valence and conduction band which act as activator centres. When free electrons or excitons hit these activator centres, an energy transfer and thus the emission of scintillation light is likely. Due to the reduced distance between the doped energy levels and the valence and conduction band, the scintillation light is typically in the visible range. Some of the
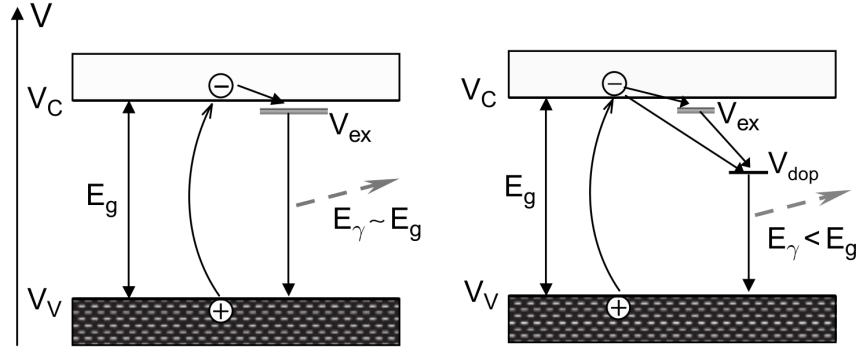
Figure 2.15: Illustration of the scintillation mechanism of inorganic scintillators with pure (left) and doped (right) crystals [1, p. 123].

energy transfer is hereby lost due to lattice vibrations (so-called phonons). The scintillation mechanism is illustrated in figure 2.15 [1].

2.4.2 Photon Spectra with Scintillators

The number of scintillation photons emitted is proportional to the deposited energy. Thus, by reading out the scintillation with a light detection device such as a SiPM or a photomultiplier tube (PMT), an energy measurement can be performed and the energy spectra of radioactive sources can be recorded. In the scope of this thesis, the recording of the gammas of a radioactive source is of most interest.

A photon with energy E_γ that enters the scintillator material has multiple ways of interaction with the material as described in section 2.1. All three processes explained in section 2.1 can lead to different structures in the recorded photon spectrum (see figure 2.16) [3]:

- In case of the photoelectric effect, a photo electron is generated with an energy according to equation (2.3). This electron will lose energy by ionisation and excitation and thus deposit all of its energy in the crystal lattice (assuming it is not leaving the crystal before getting stopped). The binding energy is often negligible or measured due to secondary effects described in section 2.1.1. In this case, the process generates the so-called photopeak in the energy spectrum corresponding to the energy of the incident gamma $E_\gamma = h\nu$.

- For higher energies (in the range of $100\,\text{keV}$ to $10\,\text{MeV}$), photons may interact by the Compton effect. As described in section 2.1.2, only a fraction of the incident photon's energy is transferred to an electron and consequently converted into scintillation light. The fraction of the captured energy depends on the scattering angle according to equation (2.11). In case the scattered photons escape the scintillation crystal, only this energy fraction is detected resulting in a continuum in the photon spectrum with a sharp Compton edge that corresponds to the maximum energy that can be transferred in a Compton scattering process. The transferred energy $T(\theta) = E_\gamma - E'_\gamma(\theta)$ with equation (2.11) is

$$T(\theta) = E_\gamma \cdot \left(1 - \frac{1}{1 + \frac{E_\gamma}{m_e}(1 - \cos\theta)}\right) \tag{2.31}$$

which has a maximum for a scattering angle of $\theta = 180°$. Thus the Compton edge corresponds to the following energy:

$$T_{\max}(\theta = 180°) = E_\gamma \cdot \left(1 - \frac{1}{1 + 2 \cdot \frac{E_\gamma}{m_e}}\right) = \frac{2E_\gamma^2}{m_e + 2E_\gamma} \tag{2.32}$$

- In case the scattered photon of a Compton scattering process interacts with the scintillation material again, more energy of the initial photon's energy is captured. If the subsequent interaction is a photoelectric effect, this interaction sequence will contribute to the creation of a photopeak. A series of

14

multiple Compton scattering processes leads to measured energies in-between the Compton edge and the photopeak.

- Pair production may occur at energies above 1 MeV, leading to the creation of an electron-positron pair. The created positron annihilates with an electron of the crystal shortly after its creation. This annihilation produces two photons. Assuming the kinetic energy of the annihilating electron and positron is negligible, each photon carries an energy of $m_e = 511\,\text{keV}$. In case both of the created photons are absorbed in the material, the event contributes to the creation of a photopeak. If one of the photons escapes, only a part of the initial energy is measured $h\nu - m_e$, resulting in the creation of the so-called *single escape peak*. The *double escape peak* corresponds to both photons escaping the scintillator such that only $h\nu - 2m_e$ is measured.
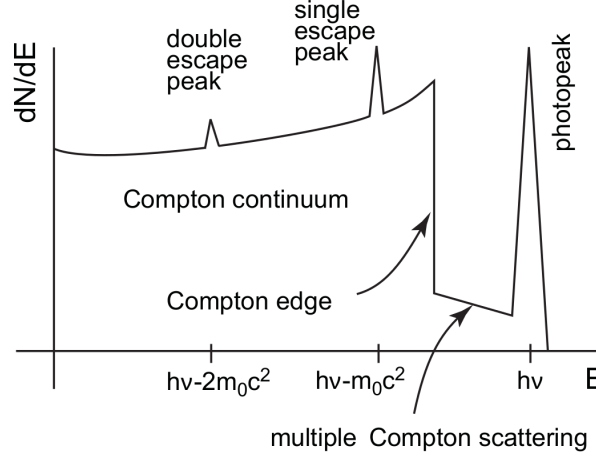

Figure 2.16: Schematic of an exemplary photon spectrum [3, p. 530].

2.5 TOFPET ASIC from PETsys Electronics

SiPM signals can be processed by an application-specific integrated circuit (ASIC) such as the TOFPET ASIC from *PETsys Electronics* [10] which is widely used for multichannel SiPM readout. The TOFPET version that was used in this thesis is TOFPET v2c. One of these ASICs is capable of processing signals from up to 64 SiPM channels. The ASIC was originally developed for time-of-flight (ToF) measurements in PET, which require a low-noise and low-power SiPM readout with an excellent coincidence time resolution (CTR) and the ability to deal with a high input and output data rate.

2.5.1 TOFPET Readout Channels

Each of the 64 channels has an independent readout chain containing amplifiers, discriminators, charge-to-digital converters (QDCs) for a charge integration and time-to-digital converters (TDCs) for a time-over-threshold (ToT) measurement. A simplified schematic of a readout channel can be seen in figure 2.17. The output signal of a SiPM is given to a preamplifier in a first step, which provides a low input impedance. The input current signal is then replicated onto three branches called T-, E- and Q-branch. The purpose of the T-branch is to perform timing measurements, while the E-branch is used for event selection and the Q-branch integrates its replica of the input current and digitises the obtained charge using a Wilkinson analogue-to-digital converter (ADC). For the integration time window, a maximum and a minimum time value can be set. The integration is performed by charging a dedicated capacitance C_Q with the current replica for the given integration time.

Both the T-branch as well as the E-branch have an independent transimpedance amplifier (TIA) with an adjustable gain. The output of the TIA in the T-branch ($V_{\text{out\_T}}$) is fed to two identical discriminators

D_T1 and D_T2. The threshold of these discriminators ($V_{\text{th\_T1}}$ and $V_{\text{th\_T2}}$ respectively) can be configured through a 6-bit digital-to-analog converter (DAC). The voltage that is corresponding to the least significant bit (LSB) of the DAC is also configurable for each discriminator individually giving rise to a variety of possible threshold settings. However, the LSB thresholds have to be set globally while the DAC can be configured channel-wise giving opportunity for fine-tuning. In the same fashion, the *E*-branch also contains a TIA with adjustable gain whose output ($V_{\text{out\_E}}$) is fed to a discriminator D_E, where the threshold can be set in the same manor.

The discriminator outputs are used for the control of an internal triggering logic. An adjustable delay can be added to the output of discriminator D_T1 [11].
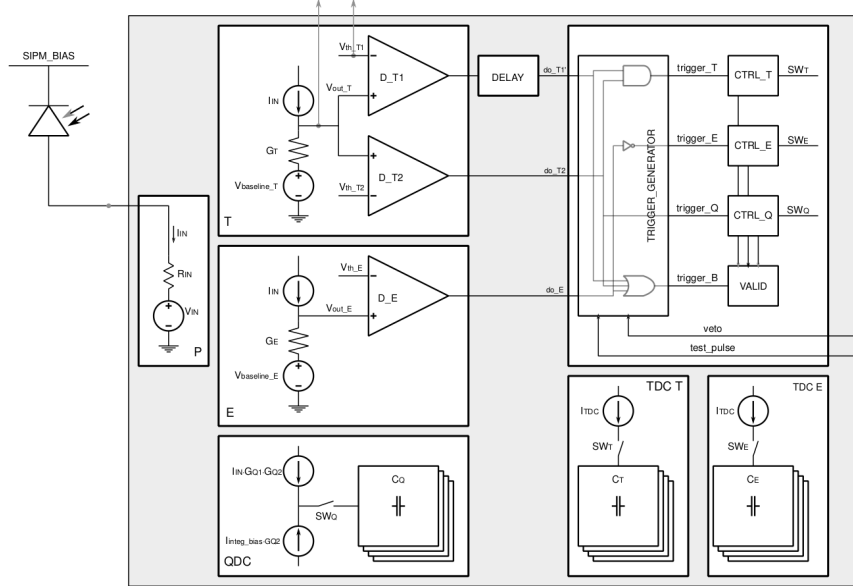

Figure 2.17: Simplified schematic of a readout channel in the TOFPET ASIC [11, p. 2].

2.5.2   Trigger Modi in TOFPET

There is a variety of trigger modi selectable for the operation of the TOFPET ASIC. Only two trigger modi are relevant in the scope of this thesis.

Single Threshold Trigger T1:   This is a simple trigger mode that only relies on the output of discriminator D_T1 (*do_T1*). No delay is added to the output. A first time stamp is taken on the rising edge of *do_T1*. This time stamps serves as the starting point for ToT and charge integration measurements. No other trigger threshold than $V_{\text{th\_T1}}$ needs to be exceeded by a signal in order to be validated. A second time stamp is taken on the falling edge of *do_T1* marking the end of the ToT measurement. The integration proceeds until the integration time either exceeds the minimum time window and surpasses the second time stamp or the maximum time window is exceeded (independent of the second time stamp). In this thesis, the minimum and the maximum integrator time were always set to the same value to guarantee a constant integration time window with a fixed length [12].

Triple Threshold Trigger with fast Dark Count Rejection: This is the default trigger modus and is suitable for measurements with a high rate of events above the dark count level. If not stated otherwise, this trigger mode was used for measurements with TOFPET. The trigger logic aims to reject noise events while also avoiding dead time due to the measurement of events that are later discarded. This modus relies on the use of all three discriminator outputs *do_T1*, *do_T2* and *do_E*. Output *do_T1* is slightly delayed to *do_T1′*. The first time stamp is taken on the rising edge of the logical conjunction of *do_T1′* and *do_T2*. The integration is started on the rising edge of *do_T2*. Events that exceed the threshold $V_{\text{th\_T1}}$ but not $V_{\text{th\_T2}}$

are discarded without any dead time. If an event exceeds $V_{\text{th\_T2}}$ but not $V_{\text{th\_E}}$, it is discarded with some dead time (5 clock periods). An event needs to trigger all three thresholds to be validated. The second time stamp is taken on the falling edge of *do_E* [12].
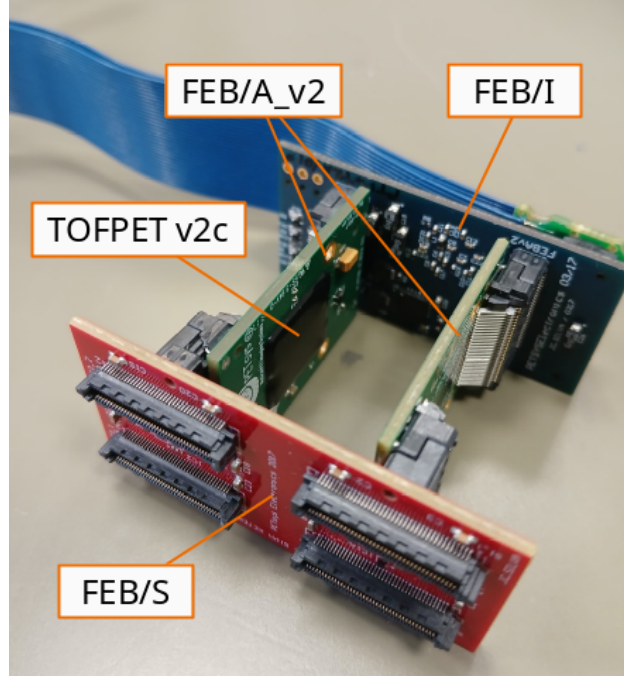

Figure 2.18: The TOFPET front-end module.

2.5.3   TOFPET Front-End Module

Figure 2.18 shows the front-end module of TOFPET. One module consists of four front-end boards. The ASIC is soldered on a front-end board called FEB/A_v2. One module contains two of these FEB/A_v2 boards possibly housing one ASIC each, such that one module can process up to 128 SiPM channels. The modules available for this thesis however are only equipped with one TOFPET ASIC. The front-end board FEB/S provides Samtec sockets for the connections of the SiPMs. Using a special Samtec cable connection on the FEB/I board, the module can be connected to a FEB/D_v2 board, where the data is further processed by an inbuilt field programmable gate array (FPGA). The FEB/D_v2 can then be linked to the PC via a gigabit ethernet (GbE) connection.

2.6   Statistical Distributions

Many of the processes that are investigated in this thesis are stochastic processes that obey statistical distribution functions. In the following, the most relevant distribution functions are introduced for later reference.

2.6.1   Poisson Distribution

The Poisson distribution describes the probability that k events occur in a given interval when λ events are expected. The events are assumed to be independent of each other. Thus, it can be applied to counting statistics. The Poisson distribution can be described by a discrete probability distribution function of the form

$$P_\lambda(k) = \frac{\lambda^k e^{-\lambda}}{k!}, \tag{2.33}$$

where $k \in \mathbb{N}$ and $\lambda \in \mathbb{R}$. The expectation value is $\mu = \lambda$ and the standard deviation is $\sigma = \sqrt{\lambda}$. For large $\lambda \geq 8$, the Poisson distribution converges to a Gaussian distribution [13].

2.6.2 Gaussian Distribution

The Gaussian distribution (also often called normal distribution) is a continuous probability distribution. The probability density function (PDF) of the Gaussian distribution has the form

$$f_{\mu,\sigma}(x) = \frac{1}{\sqrt{2\pi\sigma^2}} \cdot e^{-\frac{(x-\mu)^2}{2\sigma^2}} , \tag{2.34}$$

where $x \in \mathbb{R}$, $\mu \in \mathbb{R}$ is the expected value and $\sigma \in \mathbb{R}$ is the standard deviation [13].

2.6.3 Cumulative Distribution Function

Let X be a random variable that is evaluated at x. The cumulative distribution function (CDF) of a this random variable X is defined as

$$F_X(x) = P(X \leq x), \tag{2.35}$$

i.e. the probability that X is less or equal to x. In case of a real-valued random variable X, the distribution can be described by a continuous PDF $f_X(x)$, such that the CDF is given by:

$$F_X(x) = \int_{-\infty}^{x} f_X(\hat{x}) \mathrm{d}\hat{x} \tag{2.36}$$

In return, the PDF can be determined by differentiating the CDF [13].

3 | The Compton Camera Project

The goal of the Compton camera project at the University of Siegen is to construct a Compton camera prototype that is able to perform medical imaging for photon energies above 1 MeV. The detector called *Siegener Compton-Kamera* (SCoKa) has many potential medical application:

- **Use of isotopes with gamma energies above 1 MeV as radioactive tracers:** Radioactive tracers can be used for non-invasive diagnostic tests or medical studies to analyse functional aspects of an organ. The SCoKa device can open up the use of many isotopes which emit photons with energies above 1 MeV, e.g. 1.1 MeV and 1.29 MeV photons are emitted in the decay of ^{59}Fe which would potentially be interesting for studies of the iron metabolism or for the localisation of red blood cells. Using ^{28}Mg which decays under the emission of a 1.34 MeV gamma as a radioactive tracer, it would be possible to investigate if e.g. an Alzheimer's medicament is able to overcome the blood-brain barrier.

- **Dose monitoring in cancer therapy:** Forms of cancer treatment such as proton therapy, heavy ion therapy or targeted alpha therapy are excellent for an effective and local irradiation of cancer tissue. Proton and heavy ion therapies exploit the nature of charged particle to lose most of their energy around the end of their path in the Bragg peak (see section 2.2.1). In a targeted alpha therapy, α-emitters are accumulated in the cancer tissue. Due to the heavy mass of the alpha particles, they have a small range in the order of a few mm inside the body. A critical point in all of these therapies however is the verification of the position of the dose delivery to ensure that only cancer tissue is irradiated and healthy tissue is spared. Since in all of these therapy forms, high energetic photons above 1 MeV are created, the SCoKa device could perform a real time dose monitoring.

3.1 Established Detection Systems for Medical Imaging

Well established detection systems such as single photon emission computed tomography (SPECT) or positron emission tomography (PET) can only efficiently resolve gamma sources with photon energies up to about 600 keV.

3.1.1 SPECT

The imaging principle of SPECT relies on the use of gamma cameras, which consist of multiple collimators arranged in parallel in front of a scintillation material (see section 2.4). Paths of the gamma radiation that are in parallel to the collimators are not screened by them and reach the scintillator, where light signals are induced and read out by light detectors such as PMTs or SiPMs. In many cases, the scintillation light is guided onto the light detector by a light guide. The schematic structure of a gamma camera used in SPECT is depicted in figure 3.1. This allows the creation of a parallel image of the radiation source.

One or multiple of these gamma cameras are rotated around the radioactive source (e.g. radioactive tracers injected into a patient) creating two-dimensional pictures of the source from different spatial angles that can be combined into a 3D reconstruction of the source using inverse Radon transforms.

The energy region, in which SPECT can be used for medical imaging is limited by the photon energies that are detectable with a gamma camera which can only efficiently work up to 600 keV.
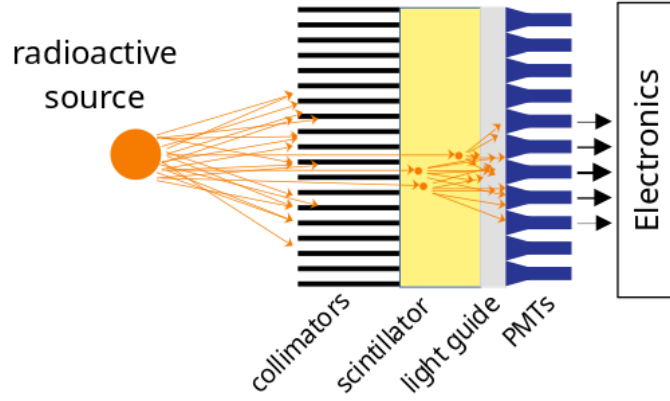
Figure 3.1: Schematic of the working principle of a gamma camera.

3.1.2 PET

In PET imaging, β^+-decaying isotopes such as ^{18}F are used that emit positrons which almost immediately annihilate with an electron of the surrounding matter. Assuming that both particles have a negligible kinetic energy, two 511 keV photons are created with opposite propagation directions in the annihilation process. PET exploits this characteristic and specifically searches for two coincident 511 keV photons, that have an angle of 180° to each other. While gamma cameras that are used for SPECT rely on the use of collimators that limit the light yield and the field of view, no collimators are needed for PET. Instead, a ring-shaped formation of scintillators coupled to PMTs or SiPMs can increase the signal-to-noise ratio by only considering coincidences on opposite sides of the detection ring. Profiting from a fast readout system, an additional spatial information can be gained by evaluating the ToF difference on both sides (see figure 3.2).
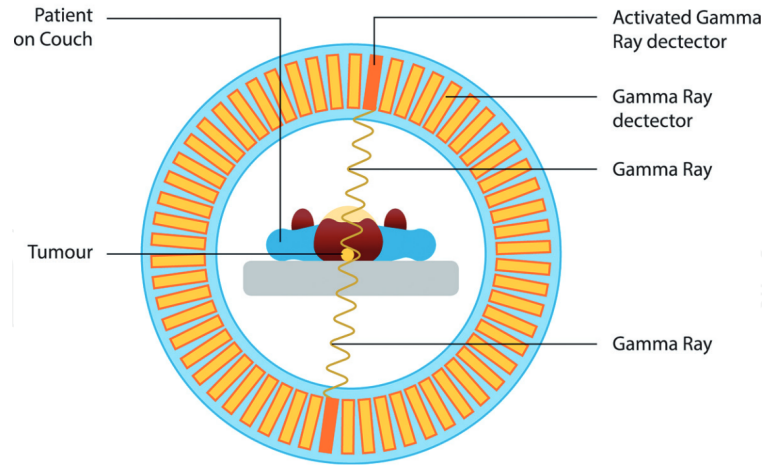

Figure 3.2: Schematic of the working principle of PET [14, p. 2].

3.2 Working Principle of a Compton Camera

Above 600 keV, Compton scattering is dominant over the photoelectric effect for most materials (see figure 2.2). Since the Compton effect is not an absorption process, collimators even built out of a high Z material such as lead ($Z_{Pb} = 82$) cannot effectively screen gamma radiation at these energies any more.

The detection principle of a Compton camera is built around the Compton scattering interaction process, where the incident gamma is scattered under an angle θ with the initial energy E_γ and final energy E'_γ (see section 2.1.2 for more details). The goal is to reconstruct the source position by reconstructing the direction from which the source photons are incident. A Compton camera usually consists of two detection layers.

In the scattering layer, the Compton scattering interaction takes places and the coordinates of the scattering point x_S, y_S and z_S are determined. The scattered photon is consequently absorbed in the subsequent absorption layer, where the energy E'_γ of the scattered photon as well as the coordinates of the absorption points x_A, y_A and z_A are determined. Figure 3.3 illustrates the basic setup of a Compton camera.
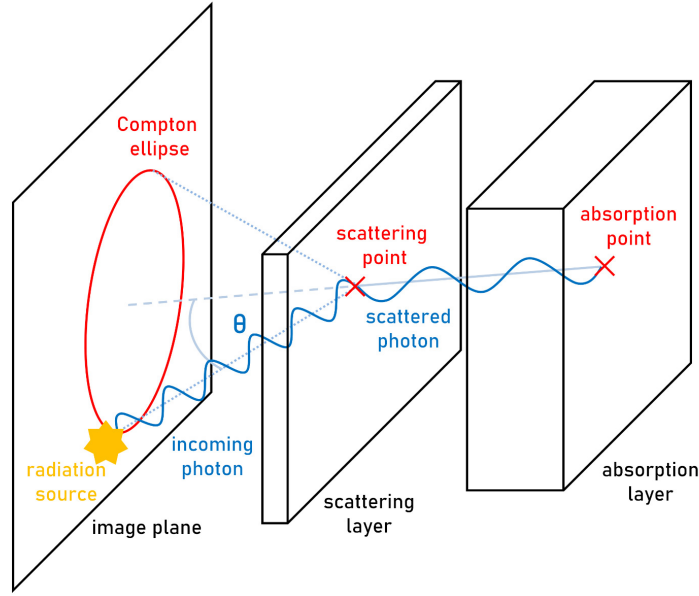

Figure 3.3: Illustration of the fundamental working principle of a Compton camera.

Depending on the application, the initial energy E_γ of the incident photons in known, e.g. in functional studies using radioactive tracers, the isotopes will emit photons with one or a few pre-determined energies. The Compton scattering angle θ can then be calculated by rearranging equation (2.11):

$$\cos\theta = 1 + m_e\left(\frac{1}{E_\gamma} - \frac{1}{E'_\gamma}\right) \tag{3.1}$$

For dose monitoring in e.g. proton therapy, the photon emission follows a non-monoenergetic spectrum such that the initial energy is not fixed. In that case it is required to also measure the initial energy E_γ in the scattering layer of the Compton camera by determining the energy loss i.e. the energy transfer to the Compton electron. Assuming that the electron is initially at rest, the energy transfer is the kinetic energy of the scattered electron: $E_{e,\text{kin}} = E'_e - m_e$. The energy E_γ can then be calculated due to energy conservation as formulated in equation (2.12):

$$E_\gamma = E'_\gamma + E_{e,\text{kin}} \tag{3.2}$$

Equation (3.1) can be expressed as:

$$\cos\theta = 1 - \frac{m_e E_{e,\text{kin}}}{E'_\gamma(E'_\gamma + E_{e,\text{kin}})} \tag{3.3}$$

An axis can be constructed between the determined absorption and scattering points. Together with the scattering angle that is calculated via equation (3.1) or (3.3), the so-called Compton cone can be constructed along this axis as depicted in figure 3.3. The radiation source is confined to be somewhere on the surface of this cone. In an image plane, the Compton cone corresponds to an ellipse. Repeating this reconstruction process for multiple incident photons produces multiple ellipses in the image plane, which ideally intersect at the source position (see figure 3.4). Thus, the source position can be detected by searching for intersections between many reconstructed Compton cones.

Incorrectly measured energies or point positions lead to a displaced ellipse in the image plane which can lead to the reconstruction of ghost sources. These result from a random accumulation of intersections. More challenging is also the reconstruction of multiple source locations simultaneously as well as non-point-like sources with a certain spatial expansion.
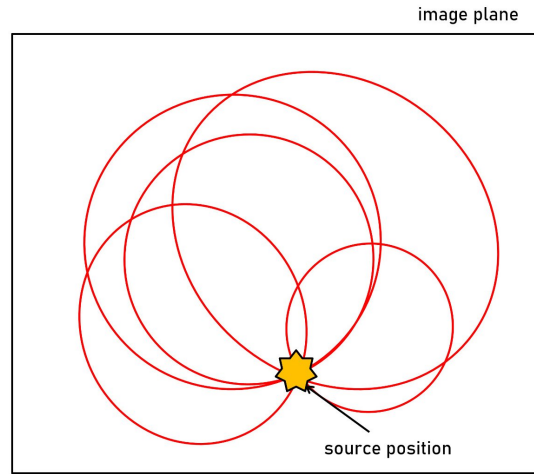
Figure 3.4: Illustration of the reconstruction principle of the source position in the image plane. Due to the kinematics of Compton scattering, each event contributes an ellipse.

3.3 Existing Compton Camera Prototypes

The concept of a Compton camera was first brought up in 1974 [15]. Since then, many further developments of the concept have been proposed. A variety of Compton camera prototypes have already been realised and some even commercialised, most of them in Japan, some of which will be discussed in more detail in the following.

3.3.1 Astrocam - Semiconductor-based Compton Camera

The *Astrocam* [16] from Mitsubishi Heavy Industries is a commercialised Compton camera. A predecessor version [17] was initially developed for astrophysics experiments and mounted on the ASTRO-H satellite. The camera consists of multiple layers of semiconductor detectors that have an excellent energy resolution. The main difference between the Astrocam and the Compton camera in [17] is the number of detector layers. With dimensions of $445\,\text{mm} \times 340\,\text{mm} \times 235\,\text{mm}^3$ and a weight of $8\,\text{kg}$ to $13\,\text{kg}$, the Astrocam can be carried to the field of application and can also be used in a medical context. The Astrocam comprises twelve detector layers, eight layers are pixelated silicon (Si) detectors that form the scattering unit, the other four are pixelated cadmium telluride (CdTe) detectors that form the absorber unit. Each Si-detector has a thickness of $0.6\,\text{mm}$ and is segmented in 16×16 pixels with an active area of $3.2 \times 3.2\,\text{mm}^2$. The CdTe-detectors are pixelated with the same dimensions.

The Astrocam can achieve an energy resolution of 2.2% and an angular resolution of 5.4° for $662\,\text{keV}$ gamma rays [16]. The resolutions were determined at full width at half maximum (FWHM). However, the sensitivity especially for gamma energies above $600\,\text{keV}$ is rather low such that data must be collected over a long period of tens of minutes in order to reconstruct an image [18].

3.3.2 Handy Scintillator-based Compton Camera

A more handy Compton camera prototype has been developed by Hamamatsu Photonics in collaboration with the Waseda University [18]. Both the scattering layer as well as the absorption layer are based on the use of inorganic scintillators. Measuring $85 \times 140 \times 160\,\text{mm}^3$ in size and weighting $1.5\,\text{kg}$, this prototype is smaller and especially much lighter than the previously discussed Astrocam. The scattering layer consists of an 50×50 array of Gadolinium Aluminium Gallium Garnet $Gd_3Al_2Ga_2O_{12}$ (GAGG) scintillator crystals doped with cerium. Each crystal has dimensions of $1 \times 1 \times 10\,\text{mm}^3$. The scintillator array is read out by 16×16 SiPMs. The absorption layer is completely identical to the scattering layer and kept at a distance of $15\,\text{mm}$.

An angular resolution of about 14° was measured for 662 keV gamma rays [18] at FWHM which is significantly worse compared to the Astrocam. On the other hand, the sensitivity is massively improved in a scintillator-based setup compared to the semiconductor-based setup. An integration time of 30 s is sufficient to generate images of weak source with $6\,\mu Sv\,h^{-1}$.

3.3.3 Electron Tracking Compton cameras

Electron tracking Compton cameras (ETCCs) aim to extract more information from each event by not just tracking the scattered photon of the Compton scattering process but also the Compton electron. The track of the electron has to be measured in the scattering layer since this is where the Compton scattering takes place. When the electrons direction and energy are measured, the entire four-momentum vector of the initial photon could by reconstructed by energy-momentum conservation in principle. Thus when neglecting uncertainties, the source position could be confined to lie in a point of the image plane. Considering uncertainties, the Compton ellipses are reduced to arcs in the image plane by the additional information about the electron's direction due to kinematics of Compton scattering which is illustrated in figure 3.5. This increases the signal-to-noise ratio (SNR) and reduces the probability to reconstruct ghost sources. Many concepts of an electron tracking scattering layer have been proposed already.
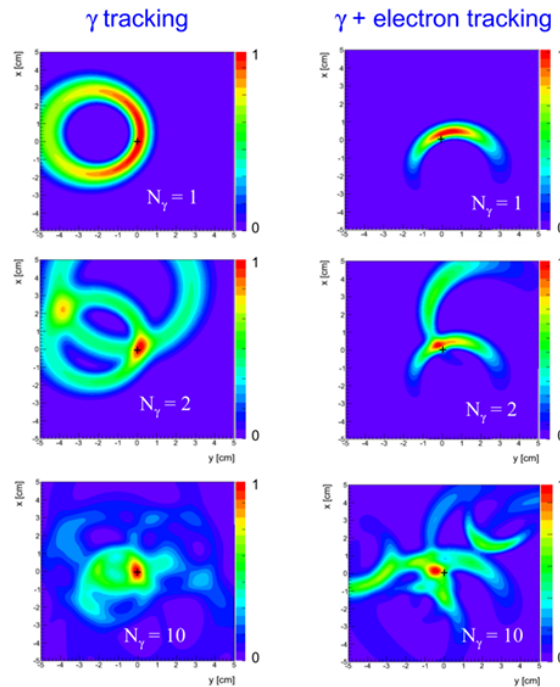

Figure 3.5: Comparison of Compton ellipses in the image plane if only the scattered photon is tracked (left) and if the Compton electron is tracked in addition (right). The events were generated using a Geant4 simulation [19, p. 68].

In [20], an ETCC prototype using a small version of a time projection chamber (TPC) (here called μ-TPC) was constructed by the Kyoto University. The μ-TPC has a fiducial volume of $8 \times 8 \times 7.5$ cm^3 and the drift volume is filled with an Ar+C$_2$H$_6$ (90:10) gas mixture with an electric field of $400\,V\,cm^{-1}$. It is surrounded by a monolithic NaI-scintillator doped with thallium. Although the track reconstruction of the electron in a TPC works very well, the interaction probability of high energetic photons with gas is low especially compared to solid-state materials. For this prototype, an efficiency of 3.5×10^{-6} was reported for 356 keV gamma rays. In addition, the energy of the electron cannot be measured with this setup, since high energetic electrons leave the relatively small fiducial volume of the μ-TPC before depositing all of their energy. Images of gamma rays with energies between 0.3 MeV and 1.3 MeV could be obtained. The angular resolution of the scattering angle was 18° and of the electron track angle was 35° for 356 keV gamma rays.

A semiconductor-based ETCC is presented in [21]. It was developed by a collaboration of the Tokyo University, Tohoku University, Kyoto University and the Japanese research organisation KEK. The scattering layer is made out of a silicon-on-insulator (SOI) pixel detector with a thickness of $500\,\mu m$ segmented into 144×144 pixels, each $30 \times 30\,\mu m^2$ in size. The absorption layer is made out of an 8×8 array of GAGG crystals, each $3 \times 10 \times 10\,mm^3$ in size. An angular resolution of $14.29°$ was reported for $662\,keV$ gamma rays. Since the SOI detector plane is very thin, the efficiency at higher energies is very low and it was suggested in [21], that the device is suitable for an energy range between $100\,keV$ and $300\,keV$.

3.4 Compton Camera with Cherenkov Photon Detection

While the examples given in the previous section 3.3 demonstrated that the Compton camera concepts works in principle, they can only provide effective imaging for photon energies below $1\,MeV$. The main issue is the dimension of their scattering layers which needs to be thin for the necessary spatial resolution of the determination of the scattering point. However, this heavily limits the probability of an interaction especially at higher energies. An exception are gas-based detectors such as [20], which can have larger dimensions and still accurately resolve the scattering point, however the interaction probability of photons in gases is heavily reduced compared to solid-state materials such that the effectiveness cannot be increased in this way.

The Compton camera under construction at the University of Siegen pursues the novel approach to track the electron of the Compton scattering process by its radiation of Cherenkov photons in the scattering layer. This approach was first proposed in [22]. A schematic illustration of the SCoKa scattering layer can be found in figure 3.6.
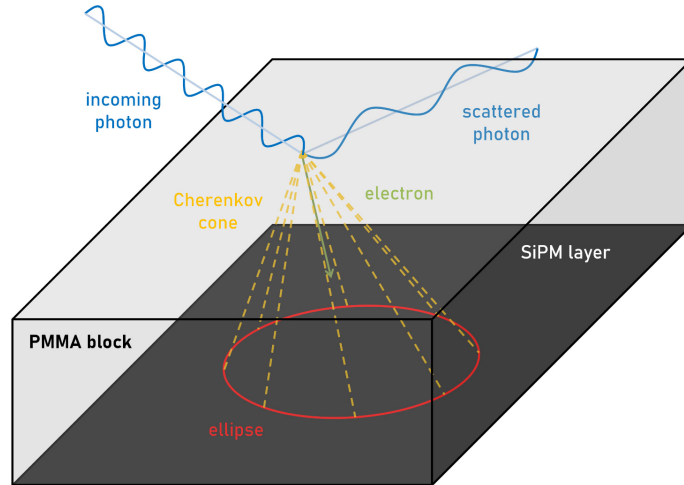

Figure 3.6: Illustration of the SCoKa scattering layer with electron tracking by Cherenkov cone detection.

The scattering layer is planned to be made out of Polymethylmethacrylat (PMMA), which has a refractive index of $n_{PMMA} = 1.49$ [3]. Since Cherenkov radiation is dominantly emitted in the UV range (see figure 2.9), it is crucial to use UV-transparent PMMA material. Assuming the electron to be sufficiently relativistic with $\beta_e \approx 1$ and together with equation (2.23), this leads to an emission angle of $\varphi \approx 47.8°$ for the Cherenkov photons which are detected by a matrix of SiPMs attached to the PMMA. The Cherenkov cone produces an ellipse on the SiPM matrix. Since the emission angle φ is known, a reconstruction of the cone is possible on the basis of this ellipse. The scattering point can be extracted from the apex of the Cherenkov cone. Thus this scattering layer design does not rely on thin dimensions for the determination of the scattering point but it can be optimized for the efficient detection of high energetic photons. Additionally, the electron direction can be extracted from the Cherenkov cone shape such that the SCoKa device provides

benefits similar to other ETCCs as described in section 3.3.3.

For high energetic electrons with $\beta \approx 1$, the emission rate of Cherenkov photons becomes constant according to equation (2.24). Thus the total number of emitted photons approximately linearly depends on the range R which depends approximately linearly on the kinetic energy $E_{e,\mathrm{kin}}$ of the electron. The electron's energy can thus be measured by counting the total number of detected Cherenkov photons on the SiPM plane, such that the SCoKa device can potentially also be used for applications in which the initial photon energy is unknown such as proton therapy.

The electron will undergo multiple scattering while traversing the PMMA, which means that a variety of ellipses might be detected on the SiPM plane that are slightly displaced to each other. Since the electron travels faster in the PMMA than the Cherenkov photons, earlier emitted photons that carry the cleanest information about the Cherenkov cone of interest arrive later on the SiPM matrix. However, the arrival time difference of the Cherenkov photons is in the order of a few ps which is not detectable with SiPMs. Since all photons essentially arrive simultaneously for the detector, it is not possible to differentiate clearly between the ellipses. Another challenging factor for the cone reconstruction is the fact, that the SiPMs have a certain dimension meaning that the ellipses are detected with a certain granularity. Limited efficiency and noise of the SiPMs make the ellipse detection harder as well. To face these challenges, neural networks will be used in the future, which are implemented on special FPGAs with integrated AI cores for fast data processing. The planned data flow for the reconstruction of the Cherenkov cone is illustrated in figure 3.7
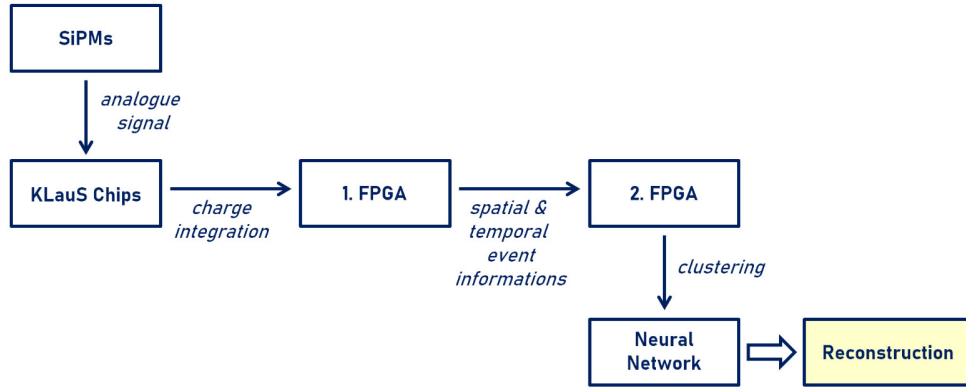

Figure 3.7: Data flow for the reconstruction of Cherenkov cones in the SCoKa scattering layer.

The SCoKa absorption layer will be similar to designs that already showed good results in other Compton camera prototypes. The sensitive volume of the absorber will be made out of scintillation crystals which have a good energy and time resolution. The scintillators under investigation in the scope of this thesis are GAGG and Lutetium Gadolinium Oxyorthosilicate $Lu_{2-x}Gd_xSiO_5$ (LGSO) which have similar properties to Lutetium Yttrium Oxyorthosilicate $Lu_{2(1-x)}Y_{2x}SiO_5$ (LYSO) crystals (see section 5 for more details). A possible design of the absorber is depicted in figure 3.8, where small-sized crystals are arranged in a matrix structure. The crystals would be isolated by a reflective material in this case. One can implement an one-to-one coupling between scintillators and SiPMs or put light spreading material in-between which distributes the light signal over multiple SiPMs. With this setup, it would be possible to resolve crystals of smaller size then the size fo the used SiPMs. Another alternative design would include a double-sided SiPM readout, which is further discussed in section 5.5.

It is currently planned to construct two slightly different scintillator-based absorber blocks allowing for a direct comparison e.g. between different scintillator or SiPM types. It also allows to test different detector geometries in the future. Since the electron needs to receive a significant amount of energy from the Compton scattering interaction in order to produce detectable Cherenkov radiation (at least 180 keV are necessary for the emission of any Cherenkov radiation), the photon will also be scattered under a significant angle. It might be beneficial to neglect certain angles in the future prototype for a better resolution at more relevant angles.

The discussed concept of a Compton camera sets some requirements to the hardware components. The
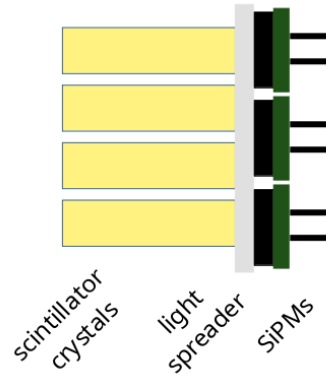
Figure 3.8: Illustration of a possible design for the SCoKa absorption layer.

scattering layer needs

- a UV-transparent and dense scattering material with a high refractive index,

- small-sized SiPMs with a high PDE in the UV range and low noise behaviour and

- a multi-channel readout system with good time resolution, low dead time and precise charge integration.

PMMA fulfils the requirements for the scattering material. A possible multi-channel readout system is the TOFPET ASIC, which is to be investigated in this thesis. An alternative ASIC is a chip called *Kanäle für die Ladungsauslese von Silizium-Photomultipliern* (KLauS) [23]. The KLauS chip is currently foreseen for the scattering layer, but it was not available in the scope of this thesis and has yet to be characterised. UV-sensitive SiPMs are discussed in chapter 4 for the use in the scattering layer.

The absorption layer requires

- scintillator crystals with a good energy resolution and low decay constant,

- low-noise SiPMs with good PDE for the emission spectrum of the scintillators and large fill factor and

- a multi-channel readout system with good time resolution, low dead time and large dynamic range to deal with larger charge values.

In principle, the same SiPMs that are promising candidates for the scattering layer could also be used in the absorption layer. Possible scintillator crystals are extensively discussed in chapter 5. The TOFPET ASIC and the KLauS chip can potentially be a suitable readout system for this layer as well.

4 | Characterisation of SiPMs

SiPMs play a crucial role in the construction of the Compton camera. They are needed for both the scattering layer, in order to detect Cherenkov light, and the absorption layer, in order to detect the light output of scintillators. The SiPMs in both layers have to meet different requirements. The detection of Cherenkov light demands for a large PDE for wavelengths in the UV and near UV (NUV) range. Additionally, the reconstruction of Cherenkov cones requires a good spatial resolution and thus a matrix of small-sized SiPMs. On the other hand, the SiPMs used in the absorption layer must have a decent PDE for the wavelength emitted by the scintillators. In order to perform an energy measurement with a scintillator, many SPADs per unit area are needed for a large dynamic range in order to handle a large amount of scintillation light. Both layers profit from SiPMs with low noise behaviour.

In this thesis, four different SiPM products are investigated. The company *Broadcom Inc.* produces a series of UV- and NUV-sensitive SiPMs, from which three versions in different dimensions are available. Their spectral sensitivity according to the manufacturer is depicted in figure 4.1 on the left side. Besides that an array of 16 SiPMs produced by *Hamamatsu Photonics* arranged in a 4×4 matrix is available as well. These SiPMs are UV-sensitive as well (see figure 4.1 on the right side). Although the PDE is generally lower than that of the Broadcom SiPM products, the Hamamatsu SiPMs combine a relatively good fill factor with low noise behaviour. An overview of the SiPMs under investigation and some properties according to their data sheets can be found in table 4.1.
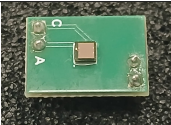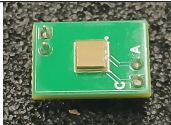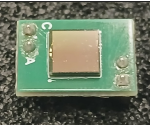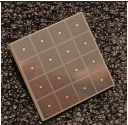
	2×2 **Broadcom**	4×4 **Broadcom**	6×6 **Broadcom**	3×3 **Hamamatsu**
Product Number	AFBR-S4NyyP014M			S13361-3075AS
Active Area [mm^2]	2×2	3.72×3.62	6×6	3×3
Cell Size [µm]	40			75
Fill Factor [%]	60	75	83	82
N_{SPADs}	2464	8334	22428	1600
Breakdown Voltage [V]	32.5			53
1p.e. amplitude [mV]	2.3	0.9	0.45	N/A
DCR[1] [Mcps]	0.5	1.7	4.4	0.5
CTP [%]	23			< 7
Temp. Coef. [$\frac{\text{mV}}{\text{°C}}$]	30			54
Data Sheet	[24]	[25]	[26]	[27][2]
Pictures				

Table 4.1: Properties of the available SiPMs taken from the data sheets. The values apply to a temperature of 25 °C and an overvoltage of 12 V for the Broadcom products and of 3 V for the Hamamatsu product.

---

[1] at the 0.5 p.e. amplitude threshold

[2] No data sheet of the exact product from Hamamatsu is available. However, the used detector is very similar to the S13360-3075CS product in the referenced data sheet. All important characteristics can be assumed to be identical except the CTP which is improved in the S13361 series compared to the S13360 series. Thus, no exact value can be given for the CTP of the used Hamamatsu SiPM.
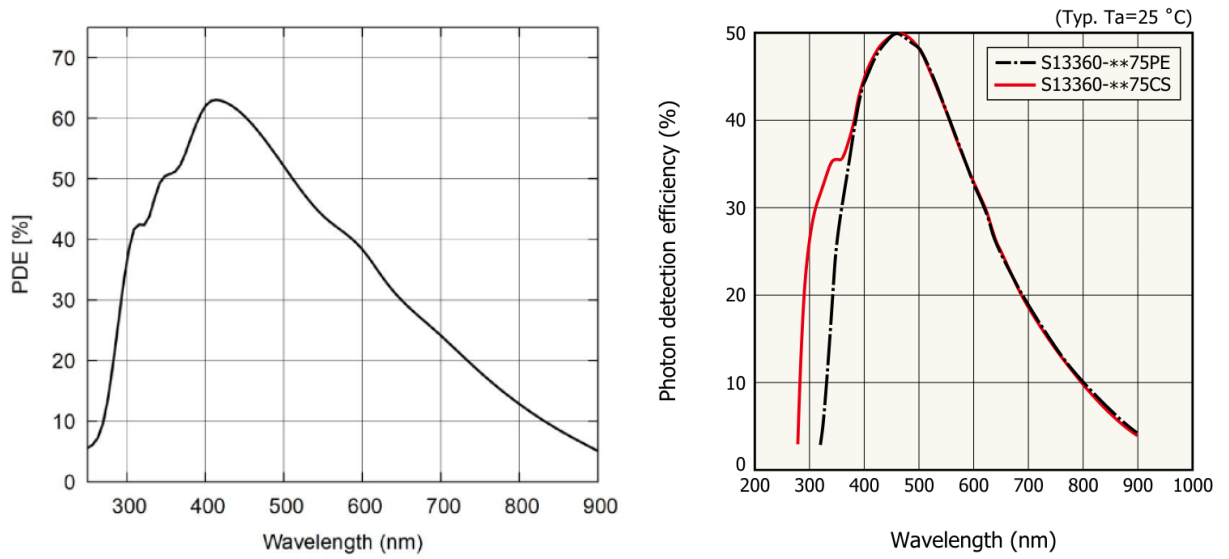
Figure 4.1: The PDE versus the wavelength of the photon for the SiPM products of Broadcom on the left side [24, 25, 26] and Hamamatsu on the right side [27].

A SiPM candidate for the construction of the scattering layer is the 2×2 Broadcom SiPM. Although the fill factor is quite low and thus the dead space quite large, this SiPM could provide a decent spatial resolution due to its small dimension, while also having a very good PDE in the UV and NUV range. Hence there will be a focus on the 2×2 Broadcom SiPM in the following sections. Properties of the other SiPMs are studied as well but less intensively.

4.1 SiPM Signals

The SiPM waveforms have a fast and a slow component. The fast component originates from the primary avalanche multiplication of the APDs and occurs in a time window below 10 ns. The slow component is an exponential decay due to the recharging of the APD by the quenching resistor and takes up to a few 100 ns, which is determined by the recovery time formulated in equation (2.25).

How prominent the slow and the fast component in a SiPM's waveform are depends on many aspects of the specific manufacture of the SiPM. The three Broadcom SiPMs are identical in their construction except for the dimension of their active area. Yet, this difference has a strong influence on the shape of their waveforms. This is due to the parasitic capacitances which are caused by the SiPM grid. Together with an external load resistor, these capacitances form an RC low-pass filter [28], which especially affects the fast component of the SiPM signal. Thus, the Broadcom SiPMs with a larger active area have a more suppressed fast component, while it is very prominent for the Broadcom SiPM with the smallest active. This can be seen in the waveform comparison shown in figure 4.2. In the slow component, SiPMs with a smaller number of SPADs have a slightly steeper exponential decay.

The waveforms of the Hamamatsu SiPMs are comparable to the waveforms of the 4×4 Broadcom SiPM (see figure 4.3). A fast component can be clearly identified, but it is not as pronounced as for the 2×2 Broadcom SiPM.

The deposited charge in a SiPM is proportional to the integration of these output waveforms. At the same time there is an approximately linear correlation between charge and the number of detected photons. Thus creating histograms out of the values obtained from a charge integration will result in a spectrum with discrete peaks, where each peak corresponds to a certain photon number. These histograms are sometimes referred to as *finger plots* due to their resemblance with a human hand and they are a useful tool for the characterisation of SiPMs. The charge integration can be performed offline or online using an ASIC.
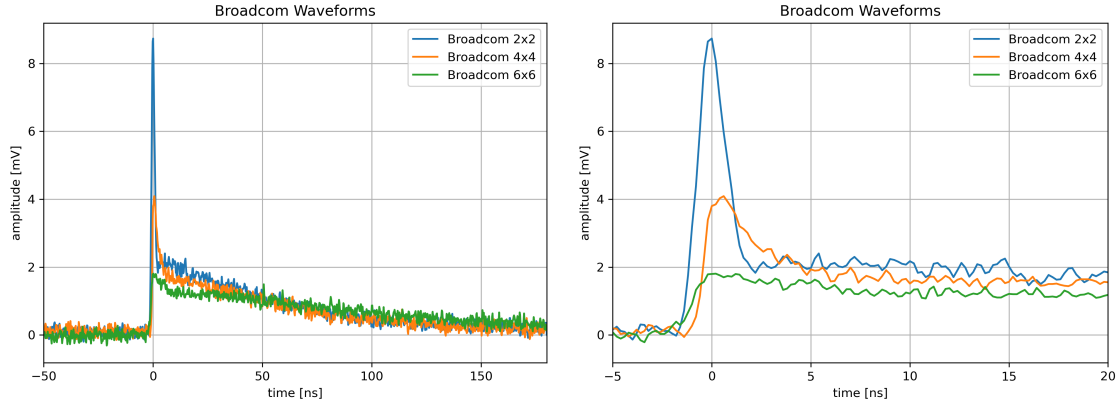
Figure 4.2: Waveform comparison between the three different SiPM products from Broadcom. Depicted are waves with a 4p.e. amplitude. The waveforms were taken for a bias voltage of 45 V and a bandwidth of 1 GHz.
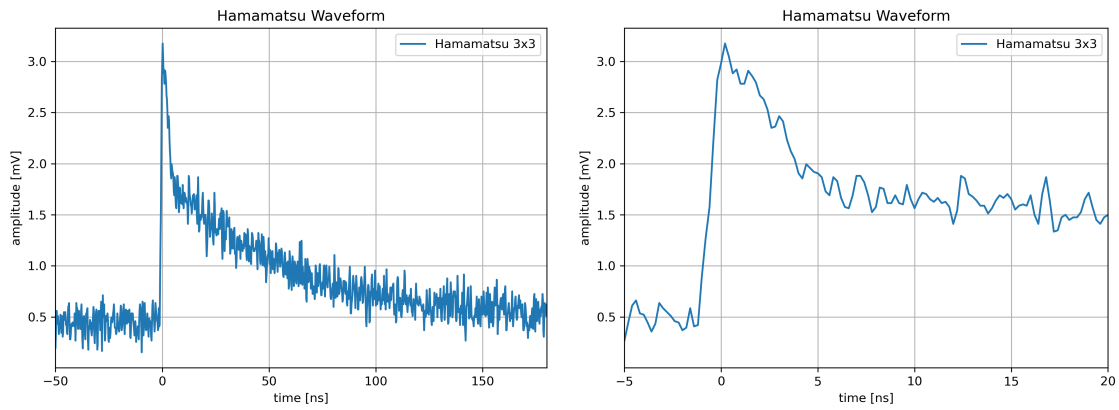

Figure 4.3: Waveform of the Hamamatsu SiPM. The waveform was taken for a bias voltage of 56 V and a bandwidth of 1 GHz.

4.2 Offline Charge Integration

The waveforms depicted in figure 4.2 and 4.3 can be integrated over numerically. An oscilloscope[3] was used for data taking in this section.

4.2.1 Experimental Setup for Data Acquisition with the Oscilloscope

The Broadcom SiPMs can be placed on special sockets with micro coaxial (MCX) connectors for the bias voltage supply and output signal readout. The 3D printed setup shown in figure 4.4 provides the opportunity to cover the SiPM in darkness. Light-emitting diodes (LEDs) can be inserted through a small pinhole in the lid of the 3D print while the SiPM is still sealed from ambient light. The bias voltage is supplied by a power supply from Keithley[4].

To connect a signal from the Hamamatsu SiPM array to the oscilloscope, a dedicated board is available, shown in figure 4.5, where each one of the 16 SiPM channels can be readout through a subminiature version A (SMA) connector. The bias supply can be controlled through a dedicated LabVIEW software using a universal serial bus (USB) connection.

The oscilloscope was connected to a computer via a local area network (LAN) cable where waveforms were captured as a text file using PyVISA. The text files were stored on the computer for further analysis.

---

[3]Rhode&Schwarz RTA4004 Digital Oscilloscope
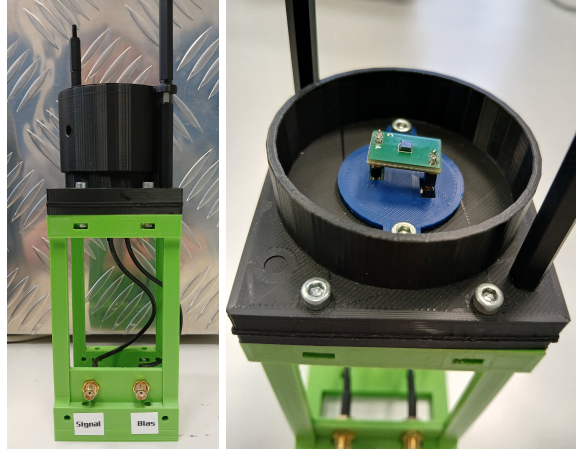[4]Keithley 2410 1100V SourceMeter

Figure 4.4: 3D printed setup for measurements with the Broadcom SiPMs using the oscilloscope.
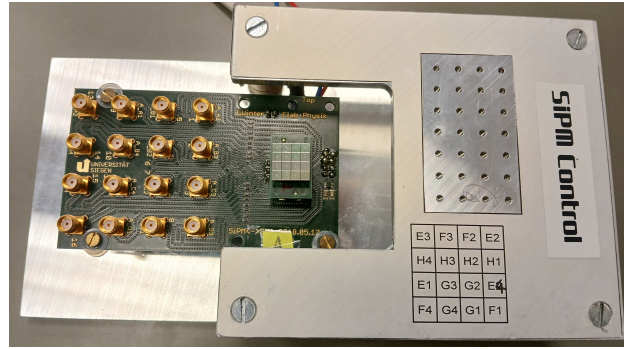

Figure 4.5: Test board for measurements of the Hamamatsu SiPM array using the oscilloscope.

4.2.2 Python Analysis Code for an Offline Charge Integration

The charge integration was then performed offline using a dedicated python code. The time stamp of the trigger of the oscilloscope is set to 0 s by default. However, this time stamp is not the best starting point for the integration, especially in case of an external trigger (as it will be used in section 4.5), where the waveform may arrive slightly sooner or later. The offline charge integration gives opportunity to define a new trigger level (called b-trigger) to find a more suitable time stamp that can serve as a marker for the beginning of the waveform. A search window around the 0 s mark can be defined, in which the first exceedance of the b-trigger level is defined as the starting point of the waveform $t_{\text{b-trigger}}$. This point lies somewhere on the rising flank of the waveform. In order to also include the rising flank in the integration window, a pregate t_{pregate} can be defined. The starting point of the integration is then set to $t_{\text{int}}^{\text{start}} = t_{\text{b-trigger}} - t_{\text{pregate}}$. The integration time window t_{int} determines how long the waveform is integrated over: $t_{\text{int}}^{\text{end}} = t_{\text{int}}^{\text{start}} + t_{\text{int}}$. For the calculation of the integration, it is necessary to determine the baseline, which can differ from 0 V. A time interval with an adjustable length right before the start of the integration $t_{\text{int}}^{\text{start}}$ is used to calculate the baseline by taking the average of all data points within this region. The integration is then performed by taking the difference of each data point of the waveform within the integration window to the baseline level and multiplying it with the time difference between two consecutive data points. The sum of these values gives the integration value. Figure 4.6 shows an exemplary waveform with highlighted integration window, baseline level and baseline region.

4.2.3 Dark Count Measurements with the Oscilloscope and an Offline Charge Integration

Waveforms of the 2×2 Broadcom SiPM were captured with the setup described in section 4.2.1 and analysed with the python code described in section 4.2.2. A trigger level of 1.7 mV was set, which is well below the 1p.e. amplitude of this SiPM even at a reduced bias voltage of 43 V. The measured charge values from the
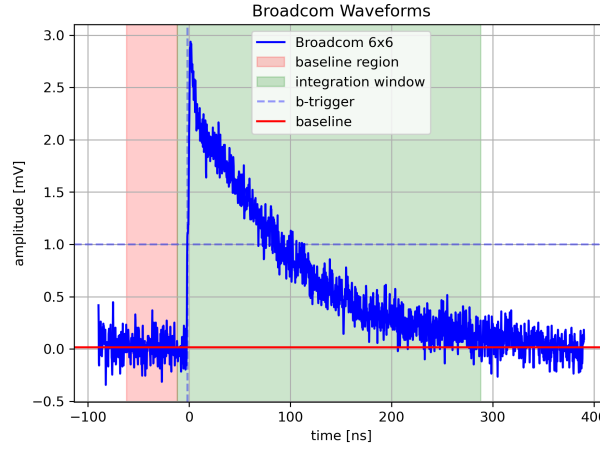
Figure 4.6: Example of a waveform integration with highlighted baseline, baseline region and integration window. The b-trigger level was set to 1 mV, the integration time window to 300 ns, the pregate to 10 ns and the length of the baseline region to 50 ns.

integration were stored in a text file and then plotted in the form of a histogram. For the creation of each histogram in this subsection, 10,000 waveforms were captured. The pregate was set to 5 ns and the length of the baseline region to 20 ns in the analysis.

Influence of the Bias Voltage

Charge spectra obtained for different bias voltages can be seen in figure 4.7 on the left side. The characteristic structure of discrete peaks is visible in all of these spectra, where the left most peak is the 1p.e. peak. By increasing the bias voltage, the values from the charge integration generally become bigger such that there is a shift to the right observable in the spectra. Additionally, the distance between the individual peaks increases with the bias voltage as well.
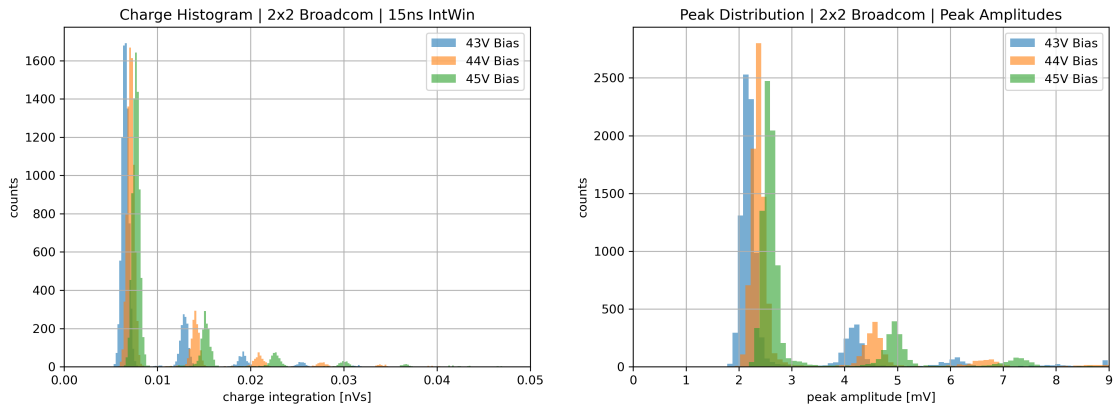

Figure 4.7: Comparison of data obtained with the 2×2 Broadcom SiPM with an integration time of 15 ns and different bias voltage. On the left are charge spectra from charge integrations and on the right distributions of the peak amplitude that were obtained for different bias voltages.

The peak amplitude of the SiPM waveforms can be obtained by taking the maximum amplitude value within the integration region. The distribution of these peak amplitudes can be seen in figure 4.7 on the right side. The 1p.e., 2p.e. and 3p.e. amplitudes are well distinguishable in these distributions and a similar shift towards higher values as in the charge spectra can be observed.

31

Influence of the Integration Time Window

In a similar fashion, charge spectra were obtained for a constant bias voltage and varying integration time window. The results are displayed in figure 4.8. For small integration windows below 100 ns, the waveform is not entirely captured in the time window. Since the fast component of the waveform already carries a lot of information about the discrete nature of the SiPM signals, it is nevertheless sufficient to integrate only over the first 10 ns of the wave in order to obtain discrete peaks in the charge spectra. This works especially well for waveforms of the 2×2 Broadcom SiPM which has a very pronounced fast component.
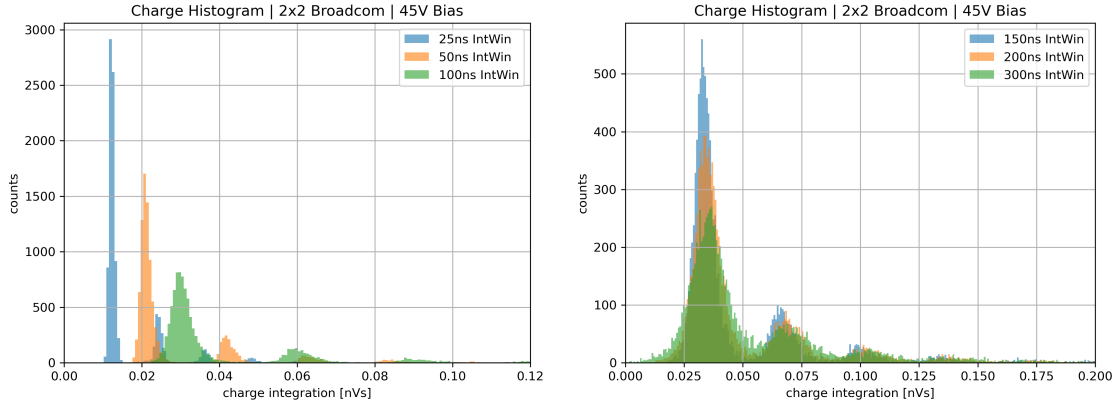

Figure 4.8: Comparison of charge spectra obtained with the 2×2 Broadocm SiPM for a bias voltage 45 V and different integration time windows. For small integration windows below 150 ns (left), larger charge values are obtained when prolonging the integration time. For larger integration windows above 150 ns (right), peaks become wider when prolonging the integration time.

More of the wave is captured in longer integration windows, thus prolonging the integration time leads to larger charge values, which can be seen in figure 4.8 on the left side. The waveforms of the 2×2 Broadcom SiPM are entirely captured for time windows of about 150 ns. Consequently, no or hardly any information about the wave is gained by using an integration time above 150 ns. Instead the integration is partially performed over the baseline. The part of the integration over the baseline does not increase the charge integration value, since a baseline integration should be close to zero, however it adds more statistical fluctuations to the measurements. This results in the spectra on the right side of figure 4.8, where there is no shift towards larger charge values any more but the peaks instead become wider due to more fluctuation. Long integration windows also risk to capture a subsequent wave in the same integration process as demonstrated in figure 4.9 which can lead to even higher fluctuations in the charge value of high photon numbers.

4.3 Online Charge Integration with TOFPET

Even-though it is useful for characterisation measurements, an offline analysis is naturally not practical for the SCoKa device since the imaging is supposed to be performed in real time, which means that SiPM signals have to be evaluated online. The TOFPET ASIC can perform an online charge integration and ToT measurement. Each measurement is saved with a time stamp in ps together with the absolute channel ID of the SiPM channel. The measurement mode can be set for each channel individually. In the following it is investigate how the TOFPET ASIC performs for the readout of small SiPM signals such as dark count events.

4.3.1 Experimental Setup for Data Acquisition with TOFPET

Special adapters were used for the connection of SiPMs to the TOFPET front-end module as shown in figure 2.18. These adapters can be plugged onto the Samtec connectors on the FEB/S front-end board and provide
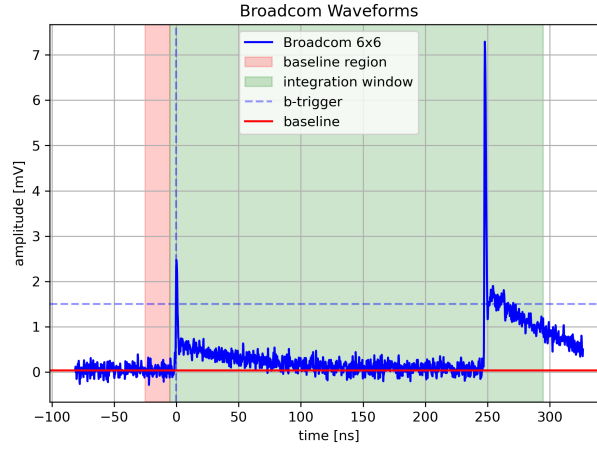
Figure 4.9: Example of a waveform integration with a pregate of 5 ns and an integration window of 300 ns. The integration window is so long that it captures the subsequent wave.

sockets for the SiPMs. The module together with an adapter board equipped with SiPMs was held by a 3D printed setup as it can be seen in figure 4.10. A fan was placed close to the module to cool the ASIC.
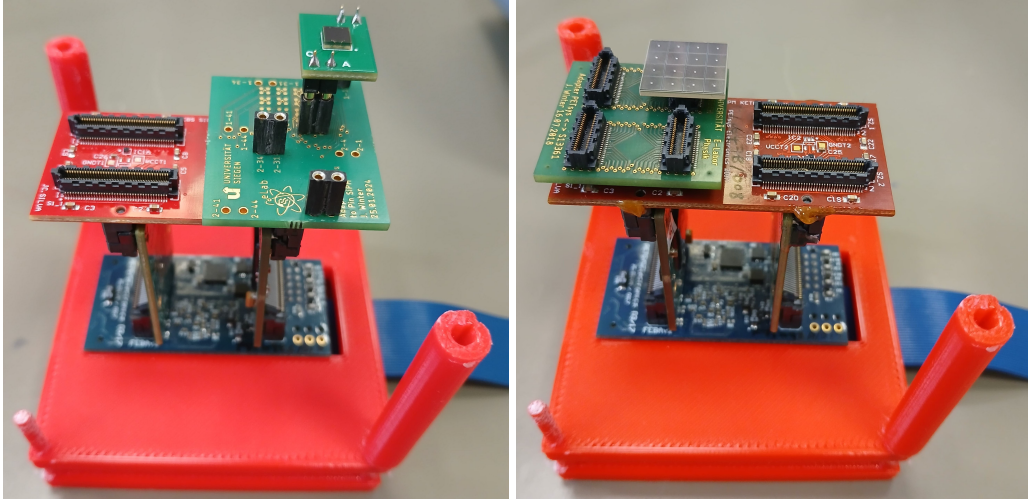

Figure 4.10: 3D printed setup for measurements with the TOFPET front-end module. On the left side, an adapter board for the Broadcom SiPMs equipped with a 4×4 Broadcom SiPM was used. On the right side, a Hamamatsu SiPM array was attached to the front-end module with another adapter board.

The front-end module is connected to a FEB/D_v2 board as described in section 2.5.3. The board is covered in a 3D printed housing (see figure 4.11) together with a fan to cool the FPGA. The data is transmitted to a PC via a GbE connection.

The most important parameters for the data acquisition can be set in a dedicated graphical user interface (GUI) from *PETsys Electronics*. It also provides a simple way to control and monitor the data taking process. The GUI can be seen in figure 4.12. The bias voltage is set globally for each front-end module. The pre-breakdown voltage (PreBDV) is set to approx. 75% of the SiPM's breakdown voltage. The 6-bit DAC for the threshold settings of the ASIC (see section 2.5.1) can be configured channel-wise in the GUI as well.

The ASIC needs to be calibrated in order to perform a measurement which can take up to 30 minutes. The behaviour of the ASIC is temperature dependent, hence it is important to cool the ASIC in order to prevent the accumulation of hot air around it. The TOFPET front-end module has two inbuilt temperature sensors. One sensor is close to the ASIC on the FEB/A_v2 board. Another sensor on the FEB/S board monitors the temperature of the SiPMs. The reading of both these sensors can be monitored in the GUI. An exemplary temperature curve is displayed in figure 4.13. The ASIC usually takes about 100 s to reach a
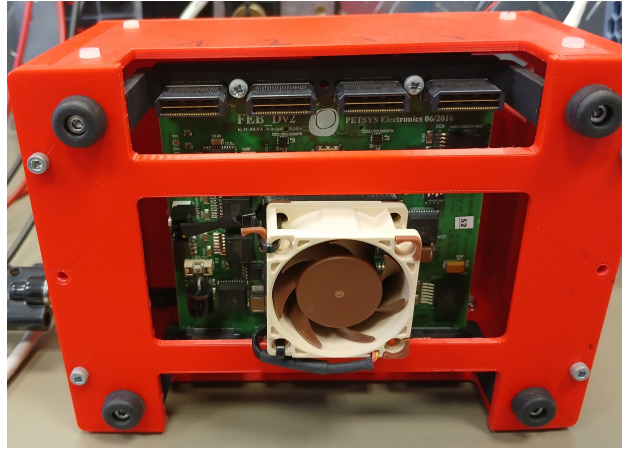
Figure 4.11: The FEB/D_v2 board in a 3D printed housing together with a fan to cool the FPGA.
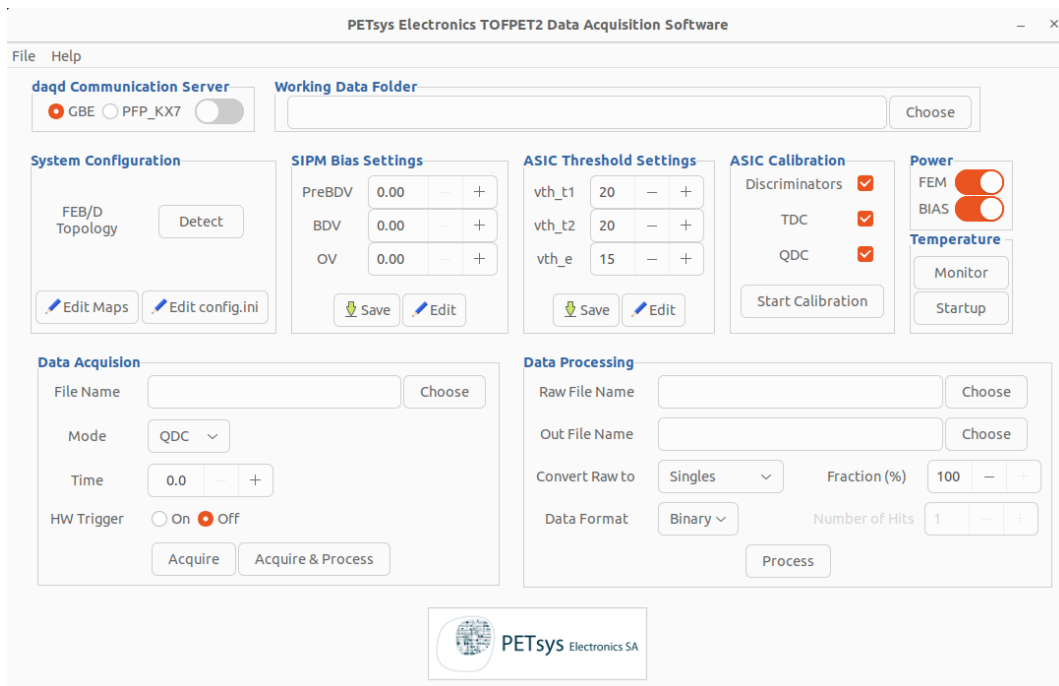

Figure 4.12: The GUI to control the data acquisition with the TOFPET ASIC.

stable temperature. Thus, all measurements and calibrations were not started before 2 min have passed.

In order to obtain good results, the ASIC's temperature during the measurement should not differ from the temperature during the calibration by more than 5 °C. In particular, QDC values that have been obtained with different calibration files do not necessarily correspond to the same charge. Recalibrating is needed when changing certain parameters such as the gain of the TIA in the *T*- or *E*-branch.

More parameters for the data acquisition can be changed in a `config.ini` file that is placed in the working folder. Here, the trigger mode can be defined and the LSB value for the thresholds settings for each discriminator can be set.

4.3.2 Dark Count Measurements with TOFPET in QDC Mode

The TOFPET ASIC is not suited to perform good measurements of dark count events in QDC mode. An issue is that a lot of the charge information of small waveforms is lost due to the triggering logic of the ASIC. The charge integration is started when exceeding a certain threshold level, but any information before this time stamp is not captured in the measurement.
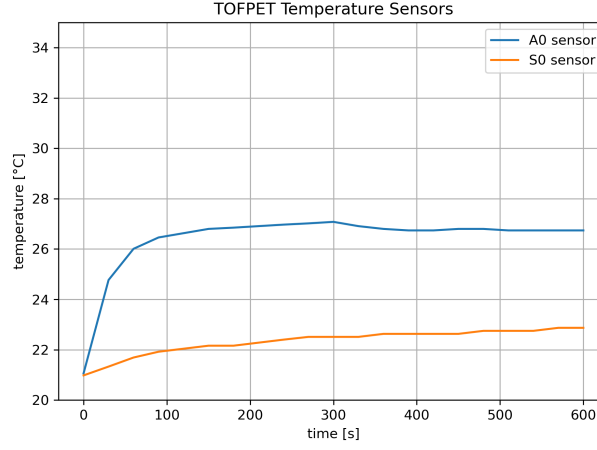
Figure 4.13: Exemplary temperature curves from the two inbuilt sensors of the TOFPET front-end module.

Thus, no discrete peak structure can be observed in the obtained charge histogram in figure 4.14, where the 2×2 Broadcom SiPM was biased with 45 V. The measurement was done with the single threshold trigger T1 described in section 2.5.2. The LSB value for the D_T1 discriminator was set to 60 and the DAC V_{th_T1} for the discriminator threshold was set to 20 which corresponds to a threshold level below the 1p.e. amplitude. The default integration time of 290 ns was used.
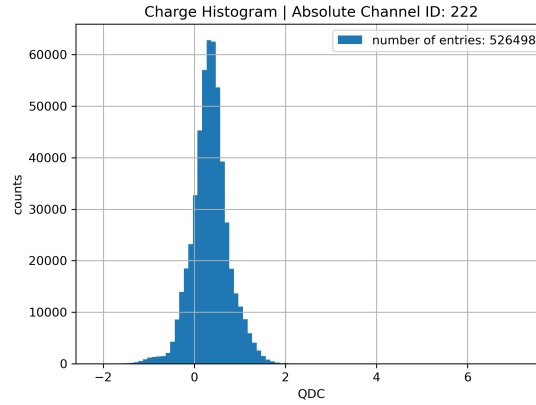

Figure 4.14: Charge histogram of the 2×2 Broadcom SiPM measured in QDC mode with the TOFPET ASIC.

4.3.3 Dark Count Measurements with TOFPET in ToT Mode

A histogram obtained in ToT mode with the same settings as in the previous subsection can be seen in figure 4.15 on the left. In contrast to the QDC histogram, a discrete peak structure is observable. Unlike the charge of a SiPM signal, the ToT of a waveform for a given threshold does not behave linearly with the detected photon number. Thus the distance between two consecutive photon peaks is not constant in figure 4.15, but higher p.e. peaks are closer together and lower p.e. peaks are more distant to each other.

The ToT measurement depends on the threshold V_{th_T1}. A comparison between ToT histograms obtained for different thresholds can be seen in figure 4.15 on the right side. Evidently, the lower the threshold the higher the measured ToT values, since for a lower threshold level, the first time stamp is taken earlier and the second time stamp is taken later.

Since every measurement is assigned a time stamp in the data acquisition with TOFPET, it is possible to extract information about the inter-time distribution as well, i.e. the distribution of the time distance between two consecutive dark count events. This might give rise to the opportunity to differentiate between different correlated noise contributions such as afterpulses, prompt cross talk and delayed cross talk which differ in
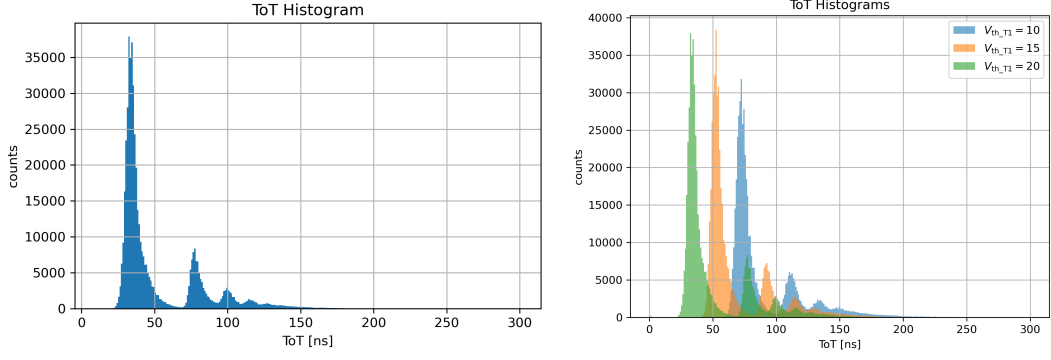
Figure 4.15: Charge histograms of the 2×2 Broadcom SiPM measured in ToT mode with the TOFPET ASIC. On the left side is a single spectrum for $V_{\text{th\_T1}} = 20$. On the right side is a comparison of ToT spectra for different threshold settings.

amplitude and inter-time with which they occur. The possibility to tell these contributions apart has been reported e.g. by [29] whose results are displayed in figure 4.16. In the following, an attempt is made to obtain similar results.
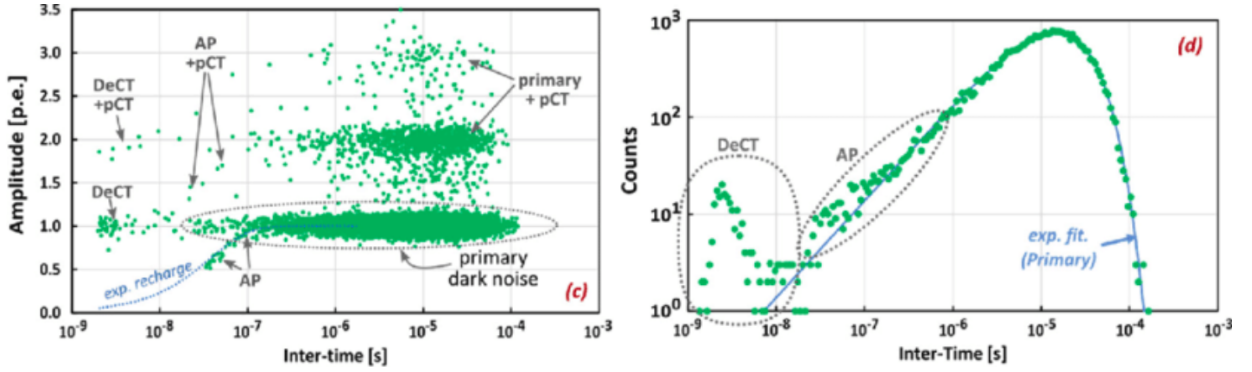

Figure 4.16: An exemplary scatter plot for SiPM signal amplitude versus inter-time (left) and a histogram of the inter-time distribution in double-log scale [29, p. 6]. Different noise contributions can be differentiated. AP stand for afterpulses, pCT for prompt cross talk and DeCT for delayed cross talk.

The TOFPET ASIC cannot determine the voltage amplitude of the SiPM signals as it was done for the scatter plot in figure 4.16. Figure 4.17 shows a scatter plot where the ToT measurement was plotted against the inter-time for the same data as in figure 4.15. The same peak structure is re-observable in the form of multiple layers where each layer corresponds to a certain photon number. The scatter points on the lowest layer correspond to the primary dark count events (1p.e. layer), while points on the layers above belong to prompt cross talk events. Afterpulses are not evident in this scatter plot. They would accumulate slightly below the 1p.e. layer at small inter-times, i.e. in the lower left corner.

Dark Counts originate from a Poisson process. Thus, the number of dark count events in a given time interval $(0, t]$ follows the Poisson distribution in (2.33) with $\lambda = R_{\text{DC}}t$, i.e.

$$P_{R_{\text{DC}}t}(k) = \frac{(R_{\text{DC}}t)^k e^{-R_{\text{DC}}t}}{k!}, \tag{4.1}$$

where R_{DC} is the average DCR. The probability to find no dark count event in the interval $(0, t]$ is hence given by:

$$P_{R_{\text{DC}}t}(0) = e^{-R_{\text{DC}}t} \tag{4.2}$$

Let T be the time at which a dark count event occurs, i.e. the inter-time assuming that a previous event
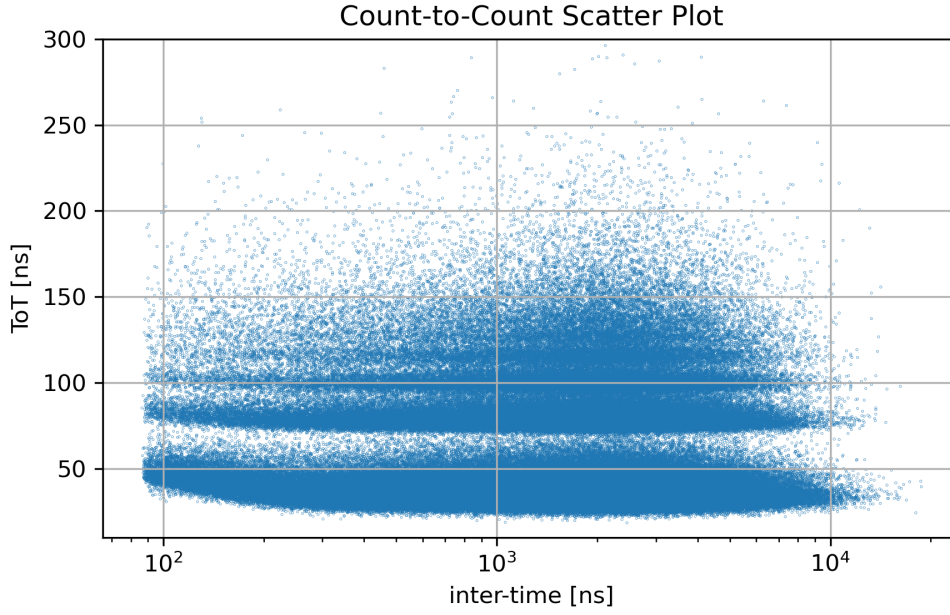
Figure 4.17: Scatter plot of the ToT measurement with the inter-time for the 2×2 Broadcom.

happened at time 0. Equation (4.2) can be re-interpreted as the probability that T is bigger than t. Thus:

$$P(T > t) = P_{R_{DC}t}(0) = e^{-R_{DC}t} \tag{4.3}$$

$$\Rightarrow P(T \leq t) = 1 - e^{-R_{DC}t} \tag{4.4}$$

This implies that (4.4) is the CDF F_T of the inter-time T as its random variable

$$F_T(t) = P(T \leq t) = 1 - e^{-R_{DC}t} \tag{4.5}$$

from which follows the PDF with:

$$f(t) = \frac{dF_T}{dt}(t) = R_{DC} \cdot e^{-R_{DC}t} \tag{4.6}$$

In conclusion, the inter-time distribution of dark count events follows an exponential distribution, which means that a histogram of the inter-time measurements will also follow an exponential distribution as long as the bin width is constant. This distribution is often referred to as the *inter-arrival time distribution* in a Poisson process. The obtained inter-time distribution for the same data as in figure 4.14 from the QDC measurement is displayed in figure 4.18.

The distribution for inter-times above 2000 ns is exponential as described in equation (4.6). Inter-times below 2000 ns do not follow the exponential distribution suggesting that the inter-time is not accurately determined in this regime by the data acquisition system. Correlated noise like afterpulses or delayed cross talk however occurs with low inter-times below 1 µs, which consequently cannot be captured in this form of analysis. Additionally, inter-times below 300 ns are not measured at all in this specific case, since the integration window for the QDC measurement was set ot 290 ns, which means that there is a dead time due to the internal triggering logic. A function of the form

$$N(T) = A \cdot e^{-R_{DC}T} \tag{4.7}$$

with parameters A and R_{DC} was fitted to the exponential part of the data. The DCR obtained from this fit is $R_{DC} = (0.722 \pm 0.002)$ Mcps.
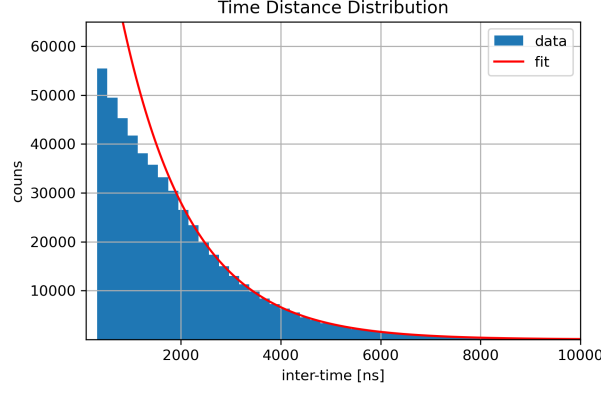
Figure 4.18: The distribution of the inter-time for the 2×2 Broadcom.

By choosing a logarithmic binning, the bin width is not constant any more but latter bins are much larger and thus accumulate more events. Hence the distribution is not described by equation (4.6). Instead the CDF in equation (4.5) has to be derived logarithmically giving:

$$f_{\log}(t) = \frac{\mathrm{d}F_T}{\mathrm{d}\log(t)}(t) = \frac{\mathrm{d}F_T}{\mathrm{d}t}(t)\frac{\mathrm{d}t}{\mathrm{d}\log(t)} \tag{4.8}$$

Since $t = 10^{\log(t)} \Rightarrow \frac{\mathrm{d}t}{\mathrm{d}\log(t)} = t$, this leads together with equation (4.6) to:

$$f_{\log}(t) = R_{\mathrm{DC}}t \cdot e^{-R_{\mathrm{DC}}t} \tag{4.9}$$

The same data from figure 4.18 is displayed in a double log-scale in figure 4.19. A fit using the model

$$N(T) = AT \cdot e^{-R_{\mathrm{DC}}T} \tag{4.10}$$

with parameters A and R_{DC} was performed to the data with inter-times above 2000 ns. A discrepancy from the expected distribution is again observable below 2000 ns. The DCR obtained from this fit is $R_{\mathrm{DC}} = (0.756 \pm 0.013)$ Mcps.
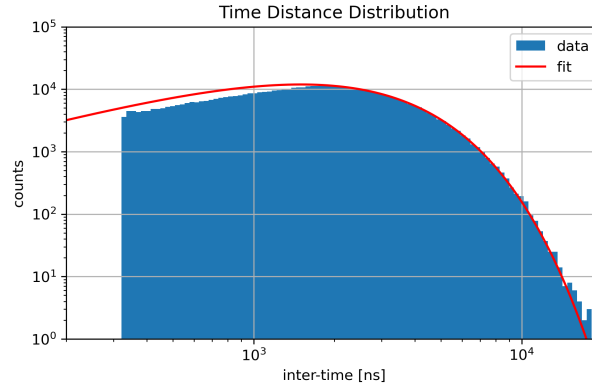

Figure 4.19: Time distribution of the inter-time for the 2×2 Broadcom in double log-scale.

Both observed DCR values are larger than the value of 0.5 Mcps given by the manufacturer. However, the temperature of the SiPM might have been larger than the reference temperature of $25\,°C$ during the measurement.

38

4.4 Staircase Plots

The noise behaviour of the SiPMs can be studied in more details in so-called staircase plots. These plots are acquired through a threshold scan, where the rate of dark count events is measured for different threshold levels. The TOFPET ASIC can perform such a threshold scan by iterating through all 64 threshold values of the V_{th_T1} DAC (while keeping the LSB value constant) in steps of one. For each threshold setting, the event rate is measured four times out of which an average rate is calculated. In these threshold scans, the DAC value of the threshold behaves inverted against the actual voltage threshold at the discriminator, i.e. the larger the DAC value the smaller the actual threshold.
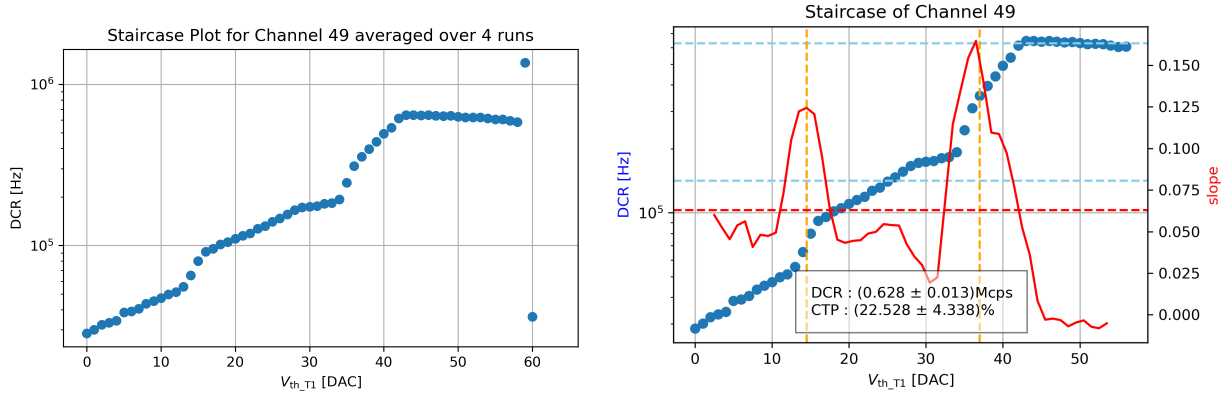

Figure 4.20: Staircase plot for the 2×2 Broadcom SiPM obtained from a threshold scan with TOFPET using an LSB value of 57 and a bias voltage of 45 V. On the right side is an analysis of this stair. The slope (red) is used to determine plateau-regions and edges within the staircase structure. The dashed red line indicates a pre-defined level to identify the position and width of the edges. Edge positions are highlighted with an orange dashed line. The light blue dashed lines indicate the determined plateaus.

An exemplary staircase plot for the 2×2 Broadcom SiPM can be seen in figure 4.20 on the left side. Threshold intervals are evident, in which the DCR is hardly changing. In between these intervals, there is a rapid increase in the DCR. This results in the staircase-like structure with plateau regions and edges. An edge occurs when the threshold level reaches an amplitude of the SiPM signal that corresponds to a certain photon number. Since the peak heights of SiPM signals are vastly discrete, changing the threshold level in between these discrete levels has little effect on the detected DCR.

The staircase plot on the left side of figure 4.20 can be analysed to extract important noise quantities of the SiPM such as the DCR and the CTP. In order to perform an analysis, the plateau regions and edges of the staircase structure need to be identified. When plotting the slope between data points of the stair, the slope peaks around the edges (see right side of figure 4.20). A pre-defined level is used to determine the start and the end of an edge which is highlighted by a dashed red line in figure 4.20. Every data point that falls into a region where the slope exceeds this level is considered to belong to an edge. The remaining data points are thus divided into plateau regions that are separated from each other by gaps where the edges have been identified. The first plateau corresponds to the rightmost plateau region. The DCR corresponding to a plateau is then determined by taking the average of all the data points that are assigned to the specific plateau region. An error is estimated by taking the standard deviation. The pre-defined slope level is set by eye. If the level is set too high, edges are determined to be narrow which leads to data points with a large slope being assigned to a plateau region which increases especially the standard deviation and thus the error on the estimation of DCR of the plateau.

The CTP p_{CT} describes the probability that a primary event, which in this case will be a dark count event, induces a secondary event. The probability to have an n-p.e. signal is then given by

$$P(n) = p_{CT}^{n-1} q, \tag{4.11}$$

where $q = 1 - p_{CT}$ is the counter probability of the CTP. The first plateau corresponds to the sum of all dark

count events regardless of their peak height, since the threshold is below the 1p.e. amplitude. Thus the first plateau gives the overall DCR. The ratio between the second and first plateau is equal to

$$\frac{\text{DCR}_{\text{2nd}}}{\text{DCR}_{\text{1st}}} = \frac{\sum_{n=2}^{\infty} P(n)}{\sum_{n=1}^{\infty} P(n)} = \frac{q \cdot \sum_{n=2}^{\infty} p_{\text{CT}}^{n-1}}{q \cdot \sum_{n=1}^{\infty} p_{\text{CT}}^{n-1}} = \frac{p_{\text{CT}} \cdot \sum_{n=0}^{\infty} p_{\text{CT}}^{n}}{\sum_{n=0}^{\infty} p_{\text{CT}}^{n}} = p_{\text{CT}} \tag{4.12}$$

using an index shift. Hence the ratio of second and first plateau gives the CTP. The uncertainties on the plateaus DCR_{1st} and DCR_{2nd} propagate into an uncertainty of the CTP measurement.

For the 2×2 Broadcom SiPM with the staircase plot in figure 4.20, the following values were obtained at room temperature with a bias voltage of 45 V:

$$\text{DCR}_{\text{1st}} = (0.63 \pm 0.02) \text{ Mcps} \tag{4.13}$$
$$\text{DCR}_{\text{2nd}} = (0.14 \pm 0.03) \text{ Mcps} \tag{4.14}$$
$$p_{\text{CT}} = (22.5 \pm 4.4) \% \tag{4.15}$$

These values match quite well with the values given by the manufacturer in the data sheet (see table 4.1).

The same analysis was also performed for the 4×4 Broadcom SiPM as well (see the left side of figure 4.21), where

$$\text{DCR}_{\text{1st}} = (1.23 \pm 0.09) \text{ Mcps} \tag{4.16}$$
$$\text{DCR}_{\text{2nd}} = (0.51 \pm 0.04) \text{ Mcps} \tag{4.17}$$
$$p_{\text{CT}} = (41.6 \pm 4.1) \% \tag{4.18}$$

was found. While the obtained DCR matches quite well to the data from the data sheet, the CTP is almost twice as large. The DCR of the 6×6 Broadcom SiPM exceeds the maximum rate detectable with the TOFPET, which is capped below 1.4 MHz. Thus, this type of analysis is impossible for the 6×6 Broadcom SiPM with the TOFPET v2c ASIC. A result from a threshold scan is displayed on the right side of figure 4.21. No staircase structure is evident.
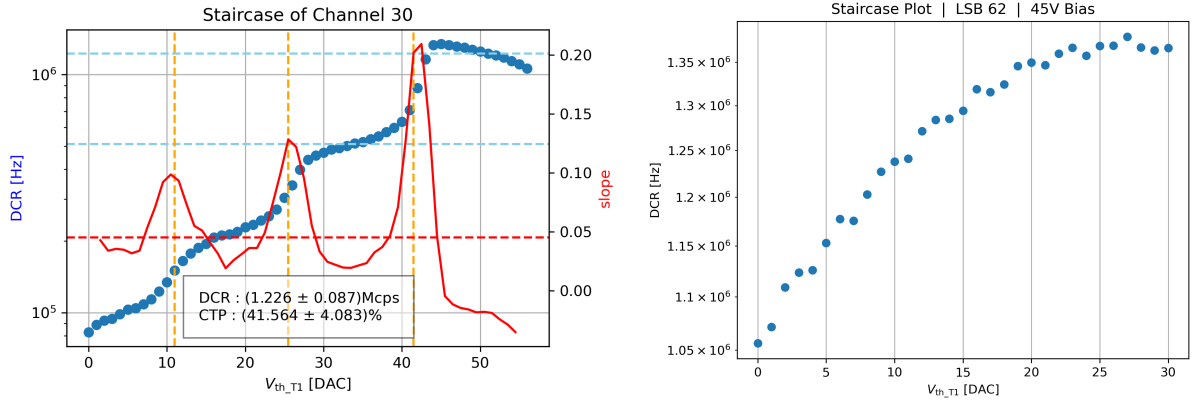

Figure 4.21: Left: Analysed staircase plot for the 4×4 Broadcom SiPM using an LSB value of 59 and a bias voltage of 45 V. Right: Staircase plot for the 6×6 Broadcom SiPM using an LSB value of 62 and a bias voltage of 45 V.

Finally, the same analysis was applied to threshold scans of the Hamamatsu SiPM array. Two analysed stairs of different SiPM channels from the array are displayed in figure 4.22. It is observable, that the channels behave quite differently. While the 1p.e. edge in the stair for channel 6 is at an DAC value of 42, it is at 39 for channel 14. This suggests that threshold levels are to be fine-tuned channel-wise for precise measurements across multiple channels in the future. The obtained noise characteristics of both SiPMs are slightly different as well. For channel 6

$$\text{DCR}_{\text{1st}} = (0.70 \pm 0.02) \text{ Mcps} \tag{4.19}$$
$$\text{DCR}_{\text{2nd}} = (0.18 \pm 0.02) \text{ Mcps} \tag{4.20}$$
$$p_{\text{CT}} = (25.6 \pm 2.9) \% \tag{4.21}$$

was obtained and

$$DCR_{1st} = (0.79 \pm 0.03) \text{ Mcps} \tag{4.22}$$

$$DCR_{2nd} = (0.21 \pm 0.02) \text{ Mcps} \tag{4.23}$$

$$p_{CT} = (27.0 \pm 2.8) \% \tag{4.24}$$

for channel 14. While the obtained DCRs match well with the values given in the data sheet, the measured CTPs are much higher than expected.
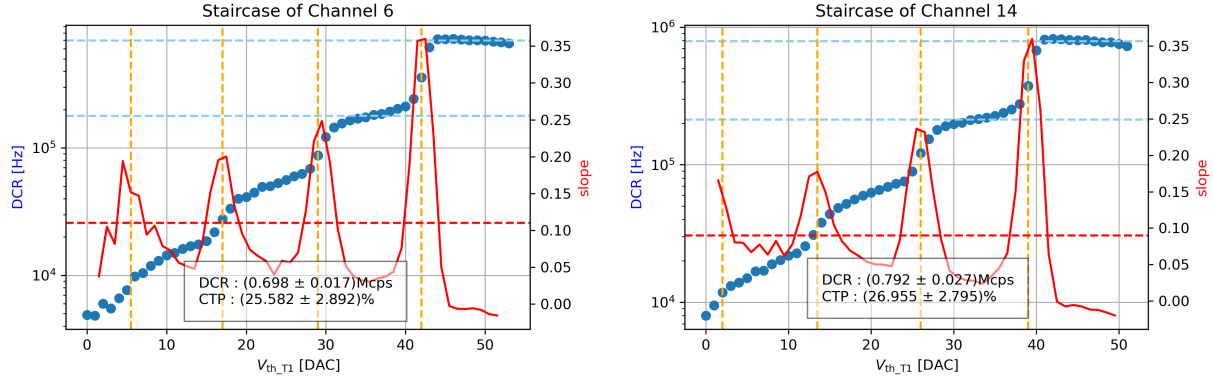

Figure 4.22: Analysed staircase plots for two channels of the Hamamatsu SiPM array using an LSB value of 59 and a bias voltage of 56 V. On the left is a stair from channel 6 and on the right is a stair from channel 14.

4.4.1 Influence of the LSB Value

The LSB value of one of the discriminators explained in section 2.5.1 determines what voltage threshold the LSB of the DAC corresponds to, i.e. what the step size is in which the threshold level at a discriminator can be changed by the DAC. The LSB values can be set by changing the variables `disc_lsb_T1`, `disc_lsb_T2` and `disc_lsb_E` in the `config.ini` file. The higher the value of these variables the smaller the voltage that corresponds to the LSB of the DAC, hence the smaller the step size. This can be observed in figure 4.23. Since a small LSB value implies a large step size between threshold levels, one can reach higher threshold levels and capture more of the stair by reducing the LSB value. On the other hand, the edges of a stair are mapped more accurately and with more data points when using a large LSB value.

Which voltage an LSB value corresponds to can be estimated from the position of the edges in a staircase plot assuming that the n-p.e. amplitude of a SiPM is known. For the 2×2 Broadcom SiPM biased with 45 V, the 1p.e. amplitude is known to be 2.3 mV such that any other amplitude can be assumed to be a multiple of that.

Table 4.2 gives an overview over detected edge positions for different LSB values in staircase plots of the 2×2 Broadcom SiPM. From these values, the difference in voltage that corresponds to one DAC value can be estimated simply by dividing the n-p.e. amplitude by the n'th edge position. In case multiple edges are detected, the average of these ratios was taken leading to table 4.3. However, these step sizes listed in table 4.3 can only be used for an estimated conversion of DAC values into voltage threshold levels, since the relation is not necessarily linear and the edge positions in a staircase plot can vary between readout channels as it was observed in figure 4.22.

4.4.2 Influence of the Baseline Parameter

Another variable parameter that can be changed in the `config.ini` file is `baseline_T`. It controls an offset in the T-branch of a readout channel. The analogous parameter for the E-branch is `baseline_E`. The default value for the `baseline_T` parameter which was used in all previous staircase plots and TOFPET measurements is 61. By decreasing the offset, the effective threshold level at the discriminator is decreased
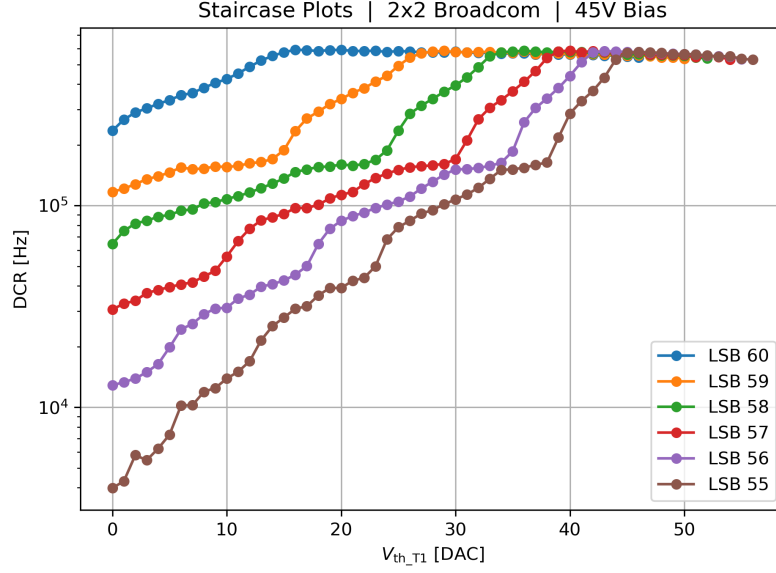
Figure 4.23: Staircase plots of the 2×2 Broadcom SiPM for different LSB values of the D_T1 discriminator. Indicated in the legend is the value of the `disc_lsb_T1` variable. The SiPM was biased with 45 V.

as well which means that higher DAC values are needed to achieve the same effect. Hence reducing the offset leads to a shift of the stair towards higher threshold levels. The influence of the offset parameter on the recording of staircase plots as well as the position of the 1p.e. threshold level can be seen in figure 4.24.
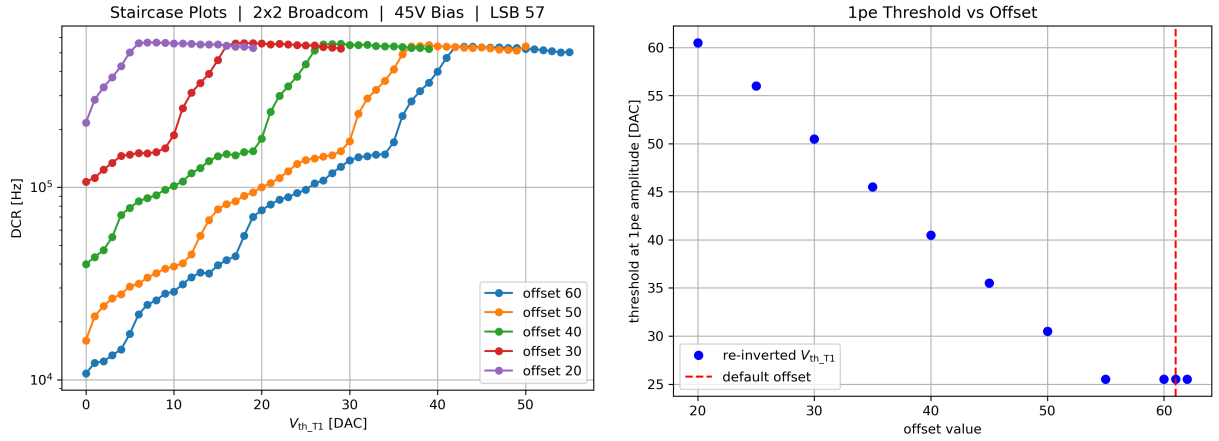

Figure 4.24: Left: Staircase plots of the 2×2 Broadcom biased with 45 V recorded for different offset values. Indicated in the legend is the value of the `baseline_T` variable. Right: The threshold value of the DAC that corresponds to the 1p.e. amplitude against the offset parameter.

For all following measurements with TOFPET, the parameter `baseline_T` is kept at its default value.

4.4.3 Influence of the Bias Voltage on the Noise Behaviour

Both noise characteristics, the DCR as well as the CTP, are strongly dependent on the bias voltage. To investigate the influence of the bias voltage on the noise behaviour of the 2 × 2 Broadcom SiPM, multiple staircase plots have been recorded under stable temperature conditions but for different bias voltages.

For each staircase plot, the DCR and CTP was determined. The result can be seen in figure 4.26. Both noise characteristics reduce a lot when the SiPM is biased with lower voltages. At 40 V bias, the DCR is reduced by approx. 30% and the CTP is only half as large compared to when using a bias voltage of 45 V

disc_lsb_T1	n-p.e. amplitude [mV]	n'th edge position [DAC]	re-inverted position [DAC]
55	2.3	40.5	22.5
	4.6	23.5	39.5
	6.9	12.5	50.5
56	2.3	37	26
	4.6	18	45
	6.9	5	58
57	2.3	31.5	31.5
	4.6	10.5	52.5
58	2.3	25	38
59	2.3	20	43
60	2.3	8.5	54.5

Table 4.2: The position of the n'th edge that is corresponding to the n-p.e. amplitude of the 2×2 Broadcom SiPM for different LSB values. Since the DAC threshold values are inverted in the threshold scans with TOFPET, the values are re-inverted in the last column.

disc_lsb_T1	average voltage step size [$\frac{mV}{DAC}$]
55	0.109
56	0.095
57	0.080
58	0.061
59	0.053
60	0.042

Table 4.3: Estimated average change in the voltage threshold level on discriminator D_T1 for a change of one DAC value using the results in table 4.2.

which is the recommended bias voltage according to Broadcom.

4.5 Efficiency Measurements with LEDs

As demonstrated in the previous section, it is beneficial to reduce the bias voltage for low noise performance. However, the PDE of the SiPM strongly depends on the bias voltage as well and might demand for higher voltage settings. Thus, the behaviour of the PDE against the bias voltage has to be investigated in order to find an optimum for the operation of the SiPM. In addition, this dependence of the PDE on the bias voltage may change for different photon wavelengths. For the detection of Cherenkov photons in the scattering layer, small wavelengths in the UV and NUV range are of special interest. The goal is to investigate whether a lower bias voltage setting than recommended by Broadcom can be used.

Unfortunately, the means that are necessary to measure the PDE directly are not available in the scope of this thesis. Though, a pulsed LED signal can be used to shine short light pulses of a narrow wavelength range onto the SiPM, from which the mean detected photon number can be determined. When keeping other settings stable in this setup, the behaviour of the PDE against the bias voltage can be investigated indirectly from the mean detected photon number.

4.5.1 Experimental Setup for LED Measurements

The setup for an offline charge integration with the oscilloscope described in section 4.2.1 was used for the measurement of LED signals. The 2×2 Broadcom SiPM was used for all measurements in this section. An LED was inserted in the pinhole of the lid of the 3D printed setup in figure 4.4. The LED was pulsed with the output of a pulse generator[5], which was split by a T-peace and simultaneously connected to the
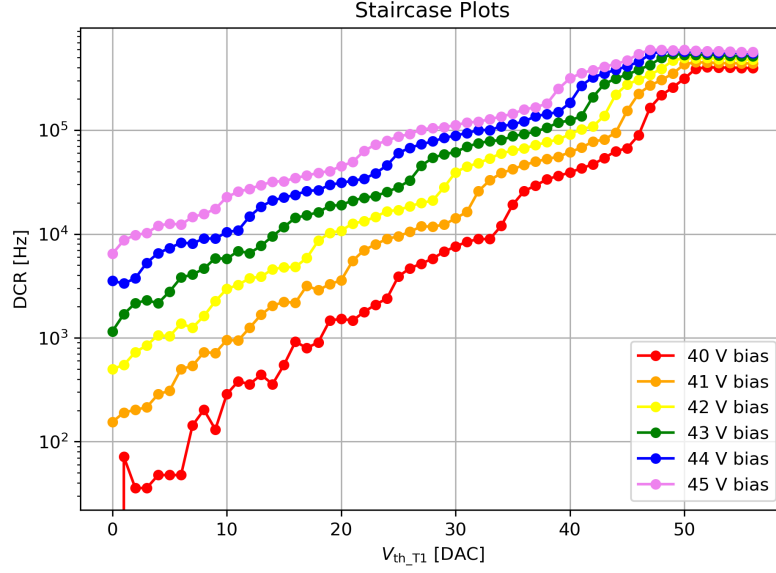
---

[5]Keysight 33250A Waveform Generator

Figure 4.25: Staircase plots of the 2×2 Broadcom SiPM recorded at different bias voltages.
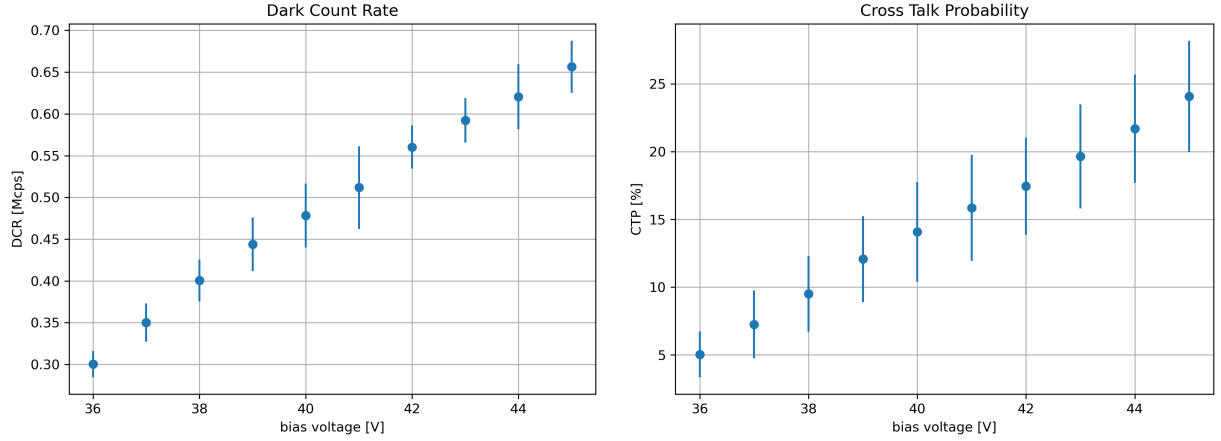

Figure 4.26: DCR (left) and CTP (right) of the 2×2 Broadcom SiPM measured at different bias voltages. The data points were determined by analysing staircase plots.

oscilloscope. The setup is summarized in figure 4.27. Multiple LEDs are available covering a large range of photon wavelengths (see table 4.4).

The amount of light that is emitted per pulse depends on the amplitude and width of the pulse. The frequency of the pulse generator was set to 100 kHz and the width of the pulse signal was set to 12 ns with an edge time of 5 ns. Different pulse amplitudes are needed for different LEDs. The output of the pulse generator is used as an external trigger on the oscilloscope, which means that a waveform is captured each time the LED emits a light pulse.

4.5.2 Analysis of the LED Measurements

A series of measurements was performed for every LED in table 4.4. In each series, 10,000 waveforms per bias voltage setting were captured with the oscilloscope. Only the bias voltage was changed within a series, all other settings were kept constant. Every waveform was integrated over using the python code described in section 4.2.2 in order to obtain a charge measurement.

An example for an obtained charge spectrum is displayed in figure 4.28. Since the SiPM has a certain PDE, there is always a chance that no photons are detected at all. In such a case, only the baseline is
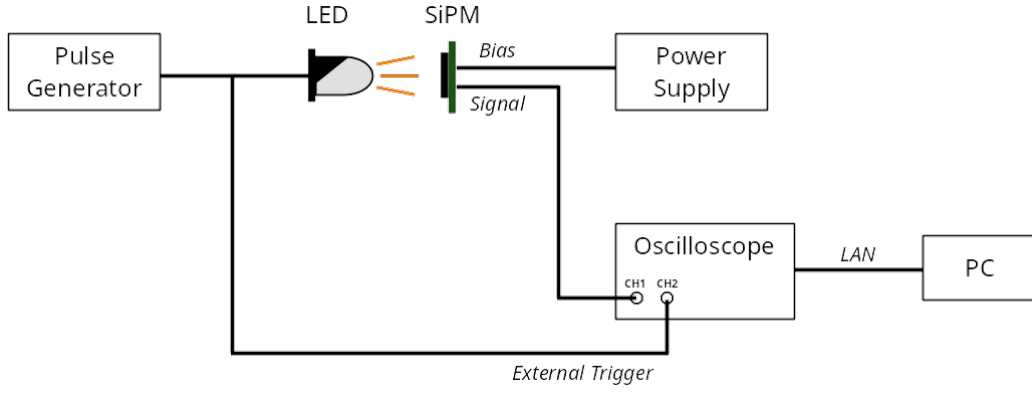
Figure 4.27: Schematic of the experimental setup for the LED measurements.

LED colour	Wavelength in nm
Red	625
Amber Yellow	585
Green	540
Blue	460
NUV	420
UV_1	375
UV_2	355
UV_3	300 - 320
UV_4	260 - 270

Table 4.4: Color and emitted wavelengths of the LEDs available.

recorded and the integration value consequently ends up around a charge of 0 nVs in an ideal case. In reality, the integration in such cases tends to result in charge values that are slightly shifted towards the negative because the baseline is overestimated due to signal residuals in the baseline region. This leads to the left most peak in the spectrum in figure 4.28, which also often referred to as the *pedestal*. The pedestal corresponds to a detected photon number of zero. In this specific case, peaks up to the 4p.e. peak are visible and the pedestal is around a charge value of −0.016 nVs.

A multi-Gaussian function of the form

$$N(q) = \sum_{n=0}^{n_{\max}} A_n \cdot e^{-\frac{(q-\mu_n)^2}{2\sigma_n^2}} \tag{4.25}$$

with A_n, μ_n and σ_n being the parameters of the n-p.e. peak and $n_{\max}$ being the number of clearly visible peaks in the spectrum was used for the fit. Let $\hat{N}(n)$ be the number of entries in the n-p.e. peak, which can be calculated by integrating:

$$\hat{N}(n) = \int_{-\infty}^{+\infty} A_n \cdot e^{-\frac{(q-\mu_n)^2}{2\sigma_n^2}} \, dq \tag{4.26}$$

Defining $A_n = \frac{k_n}{\sqrt{2\pi\sigma_n^2}}$ with a real-valued scale factor k_n leads to

$$\hat{N}(n) = \int_{-\infty}^{+\infty} \frac{k_n}{\sqrt{2\pi\sigma_n^2}} \cdot e^{-\frac{(q-\mu_n)^2}{2\sigma_n^2}} \, dq = k_n, \tag{4.27}$$

since the Gaussian distribution in equation (2.34) is normalised. From this follows:

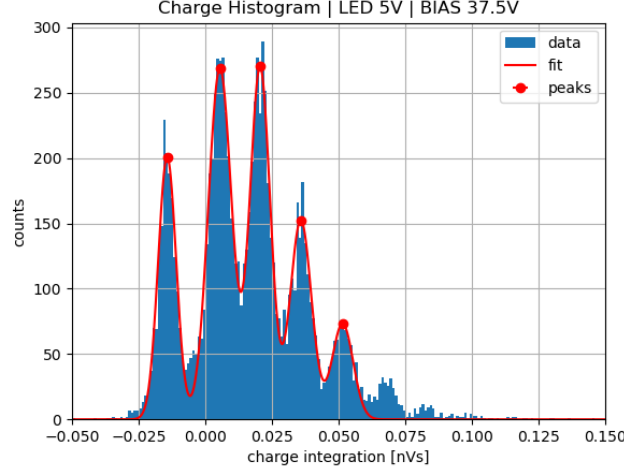$$\Rightarrow \hat{N}(n) = A_n \cdot \sqrt{2\pi\sigma_n^2} \tag{4.28}$$

Figure 4.28: Obtained charge spectrum for the UV$_4$ LED at 37.5 V bias. The pulse amplitude was set to 5 V and an integration window of 200 ns was used. A Gaussian fit was performed for every peak that is clearly visible in the spectrum.

The number of entries $\hat{N}(n)$ is equivalent to the number of times the SiPM detected n photons. The peaks in figure 4.28 are very close to each other such that they interfere with each other which makes the use of a multi-Gaussian fit function necessary. However, the multi-Gaussian model only considers peaks up to the n_{max}-p.e. peak which in this case is the 4p.e. peak. The 4p.e. peak is yet still interfered by the subsequent 5p.e. peak which is not captured in the fit model. Thus, it is useful to fit to the n_{max}-p.e. peak in order to include the interference with the $(n_{\mathrm{max}} - 1)$-p.e. peak in the model, but the n_{max}-p.e. peak itself is omitted for further analysis.

The variable $\hat{N}(n)$ is Poisson distributed which can be observed in figure 4.29 where the detected photon number n is plotted against the number of times that photon number was detected for the same data as in figure 4.28 together with a Poisson fit. The average detected photon number can be extracted from the parameter λ of the Poisson fit. In this case, an average photon number of $\lambda = 1.749 \pm 0.010$ was detected. Only statistical errors from the fit parameters are considered in this analysis.
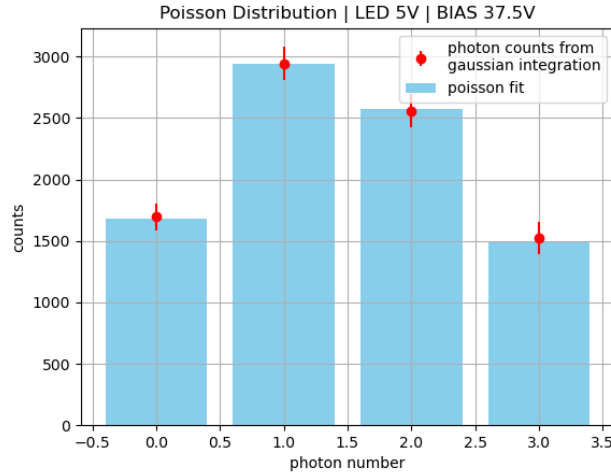

Figure 4.29: The detected photon number against the number of times that photon number was detected. The data follows a Poisson distribution.

This analysis was applied to the waveforms of every bias voltage setting. For each bias voltage, a mean detected photon number $\lambda(V_{\mathrm{bd}})$ was determined. The results from the series of measurements for the UV$_4$

LED can be seen in figure 4.30. The PDE of a SiPM is generally increasing with the bias voltage, but there is a saturation effect such that the PDE is plateauing for high bias voltages. Figure 4.30 gives a qualitative understanding of how the PDE behaves with different bias voltages and helps optimizing the bias voltage for the purpose of UV light detection. In this case, a saturation plateau can be identified for voltages above 38 V. The saturation plateau is determined as the mean of all data points in the plateau region. A threshold level is defined at 90% of the saturation plateau. The data point with the lowest bias voltage that is still above this threshold level is identified as an optimal operation voltage (37 V in this case). Increasing the bias voltage above 37 V hardly improves the PDE but strongly increases the noise behaviour as seen in section 4.4.3. Decreasing the bias voltage below 37 V would have a strong effect on the PDE.
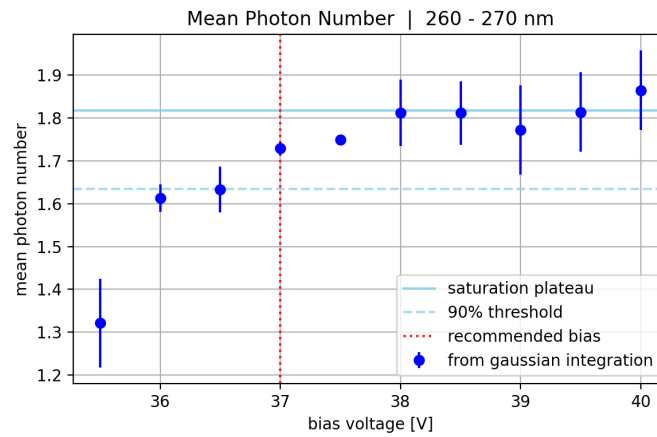

Figure 4.30: The mean detected photon number extracted from Poisson fits versus the bias voltage for the UV$_4$ LED.

This analysis method was performed for all LEDs listed in table 4.4. Plots with the behaviour of the mean detected photon number against the bias voltage for the other wavelengths can be found in the appendix. The recommended bias voltages that resulted from these analyses are summarized in figure 4.31. Generally, the lower the photon wavelength the lower the optimal bias voltage.

As it can be seen in figure 2.9, Cherenkov photons are dominantly emitted with wavelengths below 400 nm. For the blue LED with 460 nm wavelength, an optimal bias voltage of 40 V was determined. Wavelengths above this blue LED are less interest. Thus for the SiPMs in the scattering layer of the Compton camera, a bias voltage of 40 V could be ideal, when using the 2×2 Broadcom SiPM.
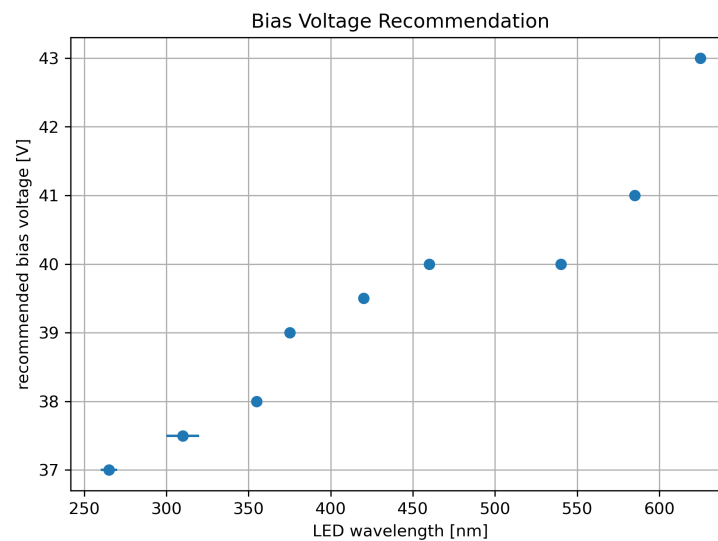

Figure 4.31: Recommended bias voltages for different photon wavelengths.

4.6 Conclusion of the SiPM Characterisation

The obtained noise characteristics of the different SiPMs measured at the recommend bias voltages (45 V for the Broadcom SiPMs and 56 V for the Hamamatsu SiPM) are listed in table 4.5. The Hamamatsu SiPM array and the 2×2 Broadcom SiPM show a similar CTP and DCR. However, the active area of the Hamamatsu SiPMs is more than twice as big such that the DCR per area is much better compared to the 2×2 Broadcom SiPM. The CTP measured for the 4×4 Broadcom SiPM is significantly larger than for the other two SiPM products but the DCR per area is close to that of the Hamamatsu SiPMs. The noise behaviour of the 6×6 Broadcom SiPM could not be measured in this chapter.

	Broadcom 2×2	**Broadcom** 4×4	**Hamamatsu** 3×3
Active Area [mm^2]	2×2	3.72×3.62	3×3
DCR [Mcps]	0.63 ± 0.02	1.23 ± 0.09	0.70 ± 0.02
CTP [%]	22.5 ± 4.4	41.6 ± 4.1	25.6 ± 2.9
DCR per Area [$\frac{\text{kcps}}{\text{mm}^2}$]	157.0 ± 3.3	91.0 ± 6.5	77.6 ± 1.9

Table 4.5: Obtained noise characteristics for the different SiPMs measured at 45 V bias for the Broadcom products and at 56 V bias for the Hamamatsu products.

The 2×2 Broadcom SiPM has proven to be a promising candidate for the construction of a SiPM matrix for the scattering layer of the Compton camera. It is evidently responsive to UV and NUV light down to at least 260 nm. Its noise behaviour for a bias voltage of 40 V, which is ideal for the detection of Cherenkov light, was measured to be

$$DCR = (0.48 \pm 0.04) \text{ Mcps} \tag{4.29}$$

$$p_{CT} = (14.1 \pm 3.7) \text{ \%} \tag{4.30}$$

which is a significant improvement compared to the values for the initially recommended 45 V. Even better noise behaviour can be achieved by cooling the SiPM in the future. The SiPM is well suitable for the detection of small photon numbers and has decent dimensions in order to achieve a good spatial resolution for the detection of the Cherenkov cone. The biggest downside of this SiPM is the comparably small fill factor due to its packaging. Whether one of the available SiPMs is suitable for the detection of scintillation light in the absorption layer has to be further investigated in the next chapter.

As demonstrated, the TOFPET ASIC struggles with the detection of small photon numbers in QDC mode. In ToT mode, small photon numbers are resolvable but the ToT measurement does not behave linear with the photon number and hence the system struggles to detect photon numbers above four. Thus the TOFPET ASIC is not ideal for the readout of the SiPM matrix in the scattering layer. An alternative ASIC is the KLauS chip that was developed at the University of Heidelberg [23] and which has to be investigated in the future and its performance has to be compared to the performance of the TOFPET ASIC.

5 | Scintillation Light Readout

Scintillators are needed for the construction of the absorption layer of the SCoKa device. Ideally, the scattered photon of the Compton scattering process is absorbed in the scintillation material and a light signal is induced. In the absorption layer, both the energy of the scattered photon as well as the absorption point have to be detected on the basis of this produced scintillation light.

There are three types of scintillation materials currently available in the lab. One scintillation crystal is a Lutetium Gadolinium Oxyorthosilicate $Lu_{2-x}Gd_xSiO_5$ (LGSO) crystal. Additionally, there are two similar version of Gadolinium Aluminium Gallium Garnet $Gd_3Al_2Ga_2O_{12}$ (GAGG) scintillators, the GAGG-T and the GAGG-HR version. The LGSO crystal was produced by the company *Oxide* and it has a smaller footprint compared to the GAGG crystals, that were produced by the company *Epic-Crystal*. The two smaller square faces of the GAGG crystals are polished. One face is polished with a higher quality providing a good surface for the coupling to a SiPM. The faces of the LGSO crystals were not polished but etched. All crystals are doped with cerium. A comparison of some properties of the available scintillator crystals are listed in table 5.1.

	LGSO	GAGG-T	GAGG-HR
Dimensions [mm^3]	$4 \times 4 \times 20$	$6 \times 6 \times 20$	
Density [g/cm^3]	7.3 - 7.4	6.6	
Light Output [$\frac{ph}{MeV}$]	N/A	42,000	50,000
Decay Constant [ns]	40 - 42	90	150
Energy Resolution[1] [%]	8	6	N/A
Emission Peak [nm]	410	530	
Hydroscopic		no	
Self-radiation	yes	no	
Data Sheet	[30]	[31]	N/A

Table 5.1: Properties of the available scintillators. Due to low sales figures of the GAGG-HR crystal, Epic-Crystal does not provide a data sheet on its website.

5.1 Source Measurements

By coupling a scintillator crystal to a SiPM, an energy spectrum can be measured as described in section 2.4.2. These spectra give rise to an analysis of many properties of the scintillators and also provide the means to perform exemplary calibrations which will later be necessary for an energy measurement. In order to understand the energy spectra of the available radioactive sources, their decay scheme and radiation will be studied in the following.

The sources that are available for test measurements are listed in table 5.2. They provide a variety of gammas with different energies as well as conversion electrons and electrons emitted in a beta decay. Spectra can be recorded using both the oscilloscope with an offline analysis and the TOFPET ASIC with an online

---

[1] at 662 keV measured with ^{137}Cs

[2] Activity calculated with: $A(T_{now}) = A_0 \cdot 2^{-\frac{T_{now}-T_0}{T_{1/2}}}$

Source	Activity (when bought)	Date of Purchase	Half-life $T_{1/2}$	Activity (01.01.2025)[2]
^{22}Na	40.7 MBq	12.03.1998	2.60 a	32.21 kBq
^{60}Co	370 kBq	01.07.2005	5.27 a	28.47 kBq
^{90}Sr	370 kBq	01.09.2018	28.81 a	317.69 kBq
^{137}Cs	370 kBq	01.07.2005	30.13 a	236.23 kBq
^{207}Bi	37 kBq	21.01.2008	31.55 a	25.50 kBq
^{241}Am	370 MBq	13.05.1993	432.2 a	351.69 MBq

Table 5.2: Available sources.

charge integration. In case the TOFPET ASIC was used, the trigger mode was set to the triple threshold trigger with fast dark count rejection.

5.1.1 Experimental Setup

Silicone grease[3] is used to optically couple one of the scintillator crystals to a SiPM avoiding reflections at the intersection between scintillator and SiPM. The scintillator is wrapped in polytetrafluoroethylene (PTFE) on every face of the crystal that is not coupled to the SiPM such that optical photons created inside the scintillator are reflected towards the SiPM.
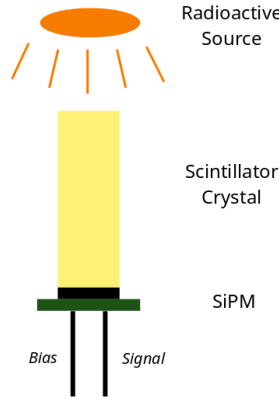
Figure 5.1: Schematic of the setup for a source measurement using a scintillator and a SiPM.

For measurements with the oscilloscope, the 3D printed setup in figure 4.4 is used. The radioactive source can be placed on top of the 3D printed lid. An issue in the setup for measurements with the TOFPET ASIC is the cooling by the fan that is needed for the operation of the ASIC. The fan can blow off the scintillator from the SiPM or displace it slightly during the data taking process and thus ruin the measurement. A 3D printed setup (see figure 5.2) provides shielding from the wind for the scintillator-SiPM-coupling but still allows the ASIC to be cooled by the fan.

The energy spectra in the following subsections were recorded using the oscilloscope setup. 50,000 waveforms have been captured for each spectrum using the 6×6 Broadcom SiPM biased with 43 V and the GAGG-HR scintillator. Unlike waveforms of small photon numbers as they occur in dark count or LED measurements, the waveforms from a scintillation light readout are much larger and more stretched out in time, since in a typical inorganic scintillator multiple thousands of photons are emitted in the detection of a high energetic photon. Additionally, the photons do not arrive simultaneously but the time distribution of the light emission is characterised by the decay time of the scintillator as described in section 2.4. For the analysis of the waveforms, an integration window of 440 ns with 40 ns pregate was used. Figure 5.3 shows an exemplary waveform detected from a scintillator.

---

[3]BC-630 silicone grease from *SAINT-GOBAIN CRYSTALS* with a refractive index of 1.465 [32]
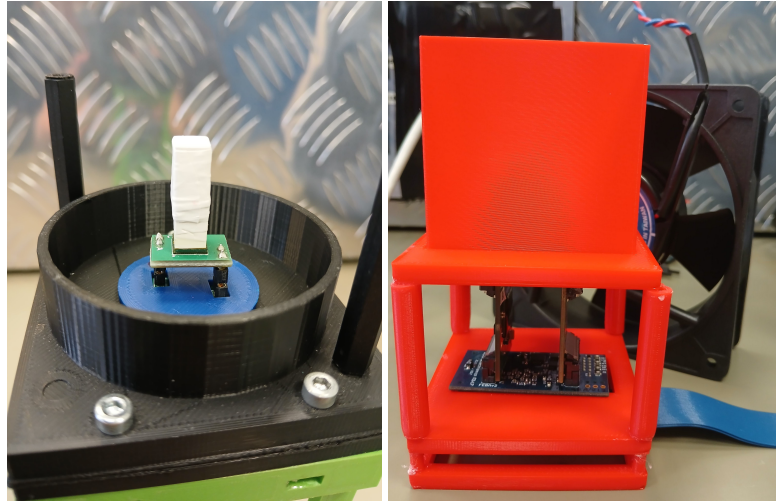
Figure 5.2: Left: Scintillator coupled to the 6×6 Broadcom SiPM on the 3D printed setup for oscilloscope measurements. The source can be placed on top of the 3D printed lid. Right: The TOFPET front-end module with an 3D printed setup to shield the SiPM area from wind. The setup averts a scintillator crystal from being blown over by the fan.
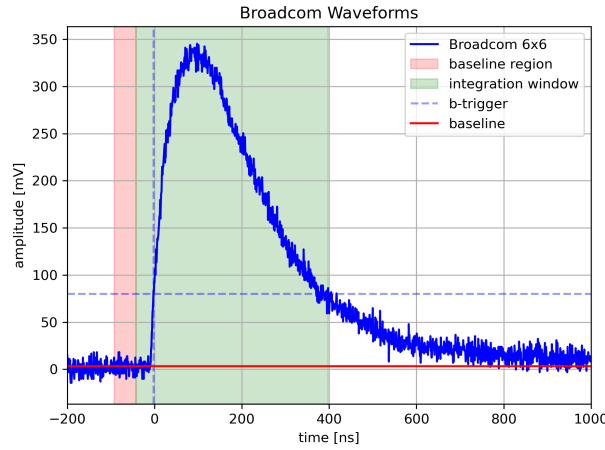

Figure 5.3: Exemplary waveform of a scintillation light flash detected with the 6×6 Broadcom SiPM and the GAGG-HR crystal. The integration window and baseline region are highlighted.

5.1.2 Sodium-22

The ^{22}Na isotope decays into ^{22}Ne via β^+-decay with BR(β^+) = 89.96% and via electron capture with BR(EC) = 10.04%. In case of a β^+-decay, a position is created with an average energy of 216.01 keV, that annihilates with an electron of the surrounding matter which leads to the creation of two 511 keV photons. In both cases, the daughter isotope ^{22}Ne is much more likely produced in an excited state (99.94%) than in a stable ground state immediately, which leads to an emission of of a 1.27 MeV photon. In summary, the most intense radiation is [33]:

Type	Energy [keV]	Intensity [%]
β^+	$< E \mathrel{>}= 216.01$	89.96
γ	511.00	179.90
γ	1274.54	99.94

The decay scheme is displayed in figure A.9 in the appendix. A recorded energy spectrum can be seen in figure 5.4. Two gamma peaks are visible. As expected, the 511 keV gammas, which are the most intense radiation contribution, produce a very pronounced gamma peak around approx. 130 nVs. The 1.27 MeV

gamma peak can be seen at approx. 280 nVs. For both gamma lines, a corresponding Compton continuum with Compton edge is identifiable. Using equation (2.32), the Compton edges are located at

$$T_{\text{max}}(511\,\text{keV}) = 340.67\,\text{keV} \tag{5.1}$$

$$T_{\text{max}}(1.27\,\text{MeV}) = 1.06\,\text{MeV} \tag{5.2}$$

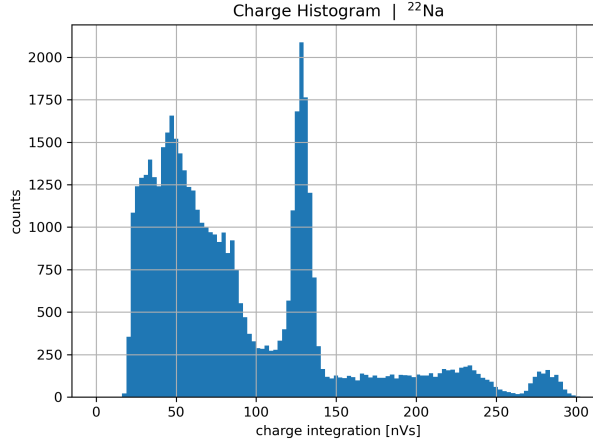corresponding to approx. 85 nVs and 240 nVs in the spectrum.

Figure 5.4: Energy spectrum of the ^{22}Na source recorded with the 6×6 Broadcom SiPM and GAGG-HR.

5.1.3 Cobalt-60

The ^{60}Co isotope decays into ^{60}Ni via β^--decay with BR(β^-) = 100%. The daughter isotope ^{60}Ni is dominantly produced in an excited state with $J^P = 4^+$ (BR = 99.88%) which decays in 99.97% of all cases into an excited state with $J^P = 2^+$ under the emission of a 1.17 MeV gamma. The $J^P = 2^+$ state decays into the stable ground state of ^{60}Ni under the emission of a 1.33 MeV gamma. The average energy of the emitted electron from the dominant initial β-decay mode is 95.77 keV. In summary, the most intense radiation is [33]:

Type	Energy [keV]	Intensity [%]
β^-	$< E > = 95.77$	99.88
γ	1173.23	99.85
γ	1332.49	99.98

The decay scheme is displayed in figure A.10 in the appendix. A recorded energy spectrum can be seen in figure 5.5. Two gamma peaks are visible on the high energy end of the spectrum corresponding to the two gamma lines in the table above. The 1.17 MeV line is visible at approx. 265 nVs and the 1.33 MeV line at approx. 300 nVs. As expected, they occur with a similar intensity. Both gamma lines should produce Compton continua with Compton edges at:

$$T_{\text{max}}(1.17\,\text{MeV}) = 0.96\,\text{MeV} \tag{5.3}$$

$$T_{\text{max}}(1.33\,\text{MeV}) = 1.12\,\text{MeV} \tag{5.4}$$

The Compton edge of the lower energetic gamma peak is clearly visible at approx. 230 nVs together with a continuum. The energy of the second Compton edge is very close to the energy of the first gamma peak such that the edge is masked.
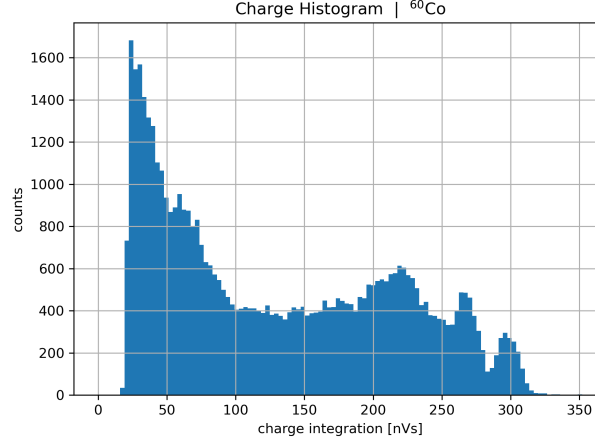
Figure 5.5: Energy spectrum of the ^{60}Co source recorded with the 6×6 Broadcom SiPM and GAGG-HR.

5.1.4 Strontium-90

The ^{90}Sr isotope decays into ^{90}Y via β^--decay with BR(β^-) = 100%. The electron of this decay is emitted with an average energy of 195.7 keV. The daughter isotope ^{90}Y itself is decaying via β^--decay into ^{90}Zr with BR(β^-) = 100% again. In 99.99% of all cases, ^{90}Y immediately decays into the ground state of ^{90}Zr such that there is no intense gamma radiation in the decay chain of ^{90}Sr. The average electron energy of the second β-decay is 932.4 keV. In summary, the most intense radiation is [33]:

Type	Energy [keV]	Intensity [%]
β^-	$< E >=$ 195.7	100.00
β^-	$< E >=$ 932.4	99.99

Both decay schemes of ^{90}Sr and ^{90}Y are displayed in figure A.11 in the appendix. A recorded energy spectrum can be seen in figure 5.6. The overlay of two beta spectra corresponding to a higher and a lower average electron energy are visible. As expected, no gamma peaks can be identified.
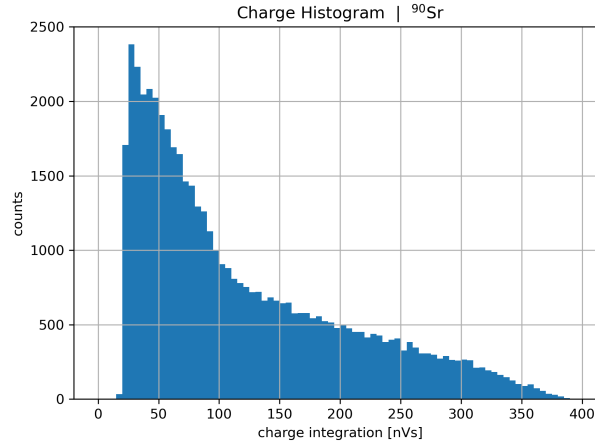
Figure 5.6: Energy spectrum of the ^{90}Sr source recorded with the 6×6 Broadcom SiPM and GAGG-HR.

5.1.5 Caesium-137

The ^{137}Cs isotope decays into ^{137}Ba via β^--decay with BR(β^-) = 100%. The daughter isotope ^{137}Ba is dominantly produced in an excited state with $J^P = 11/2^-$ (BR = 94.7%) which decays in 89.86% of all cases into the ground state of ^{137}Ba under the emission of a 661.66 keV gamma. Alternatively, the excited

^{137}Ba state can decay via internal conversion. In 8.23% of all cases, the excited ^{137}Ba state decays under the emission of a 624.22 keV conversion electron from the K-shell. The average energy of the emitted electron from the dominant initial β-decay mode is 174.32 keV. In summary, the most intense radiation is [33]:

Type	Energy [keV]	Intensity [%]
β^-	$< E >= 174.32$	94.70
γ	661.66	85.10
CE K	624.22	7.79

The decay scheme is displayed in figure A.12 in the appendix. A recorded energy spectrum can be seen in figure 5.7. The gamma peak corresponding to the 611.66 keV gamma line is clearly visible at approx. 160 nVs. It produces a Compton edge at

$$T_{\max}(661.66\,\text{keV}) = 477.34\,\text{keV} \tag{5.5}$$

corresponding to approx. 120 nVs in the spectrum. An additional peak at approx. 145 nVs can be identified which most likely corresponds to the energy of the K-shell conversion electrons with an energy of 624.22 keV. The interaction probability of electrons in scintillation material is higher compared to that of gammas. Thus, the peak of the K-shell conversion electron is only slightly less intense than the 661.66 keV gamma peak in the spectrum in figure 5.7 although the expected emission intensity of K-shell conversion electrons is much lower (as listed in the table above).
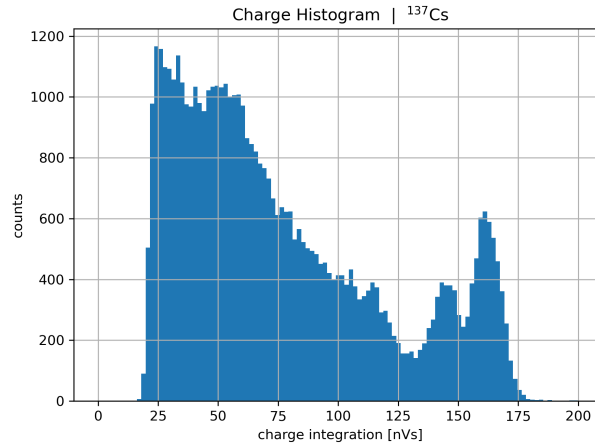
Figure 5.7: Energy spectrum of the ^{137}Cs source recorded with the 6×6 Broadcom SiPM and GAGG-HR.

5.1.6   Bismuth-207

The ^{207}Bi isotope decays into ^{207}Pb via β^+-decay with BR(β^+) = 0.038% and via electron capture with BR(β^+) = 99.962%. The decay mode via electron capture is consequently much more dominant and the creation of photons by position-electron annihilation can be neglected. In both cases, the daughter isotope ^{207}Pb is produced in excited states. The lowest of these energy levels with $J^P = 5/2^+$ (BR = 8.99%) decays dominantly (97.9%) under the emission of a 569.7 keV photon or alternatively via internal conversion. The K-shell conversion electron of this decay has an energy of 481.69 keV and the L-shell conversion electron of about 555 keV. In the dominant decay mode of the initial β-decay (BR = 84%), the daughter isotope is produced in an excited state with $J^P = 13/2^+$, which in 88.7% of all cases decays into the $J^P = 5/2^+$ state under the emission of a 1.06 MeV photon. With BR = 7.03% the ^{207}Pb isotope is produced in an even higher energy level with $J^P = 7/2^-$ which decays with a probability of 97.72% in the $J^P = 5/2^+$ state as well while emitting a 1.77 MeV photon. The emission of a K-shell conversion electron with an energy of 975.65 keV and a L-shell conversion electron with an energy of about 1049 keV can also occur in the decay process of ^{207}Bi. Additionally, X-rays can be emitted from atomic transitions such as a 21.71 keV photon

from a K-L$_2$ transition or a 36.5 keV photon from a K-L$_3$ transition. In summary, the most intense radiation is [33]:

Type	Energy [keV]	Intensity [%]
γ	569.70	97.75
γ	1063.66	74.50
γ	1770.23	6.87
CE K	481.69	1.54
CE L	~ 555	0.442
CE K	975.65	7.08
CE L	~ 1049	1.84
X-ray K-L$_2$	72.81	21.71
X-ray K-L$_3$	74.97	36.50

The decay scheme is displayed in figure A.13 in the appendix. A recorded energy spectrum can be seen in figure 5.8. The 569.7 keV gamma line is the most pronounced gamma peak at approx. 145 nVs. Another gamma peak is visible at approx. 250 nVs corresponding to the 1.06 MeV gamma line. The 1.77 MeV gamma peak is not visible and would be out of range for the spectrum in figure 5.8. The two visible gamma peaks produce Compton edges at

$$T_{\text{max}}(569.7\,\text{keV}) = 393.31\,\text{keV} \tag{5.6}$$

$$T_{\text{max}}(1063.66\,\text{keV}) = 857.65\,\text{keV} \tag{5.7}$$

$$\tag{5.8}$$

corresponding to approx. 100 nVs and approx. 200 nVs in the spectrum. An additional peak at approx. 220 nVs in-between gamma peak and Compton edge of the 1.06 MeV gamma line can be identified which most likely corresponds to the most intense conversion electron radiation with an energy of 975.65 keV. Other peaks from conversion electrons are not visible. At the low energy end of the spectrum, a pronounced peak is visible that is partially cut out in this case due to the trigger level. This peak is created by the X-ray radiation from which there are the two most intense radiation lines listed in the table above. These two lines are energetically very close to each other (within 2 keV) and thus not distinguishable in the spectrum. A weighted average energy can be calculated based on the intensities of the X-ray lines:

$$E_{\text{K}\alpha} = \frac{I_{\text{K-L}_2}E_{\text{K-L}_2} + I_{\text{K-L}_3}E_{\text{K-L}_3}}{I_{\text{K-L}_2} + I_{\text{K-L}_3}} = 74.16\,\text{keV} \tag{5.9}$$

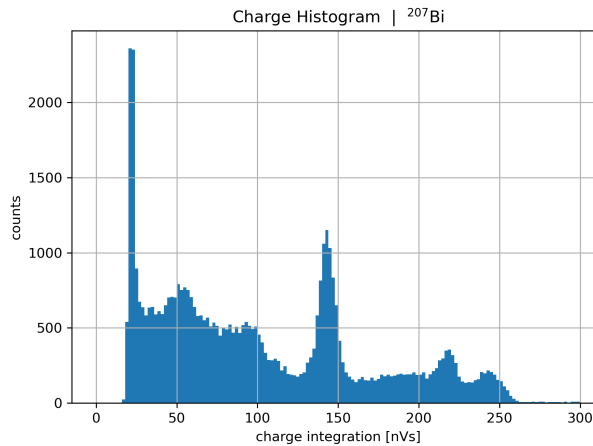This averaged energy can be assigned to the peak on the low energy end of the spectrum in figure 5.8.

Figure 5.8: Energy spectrum of the ^{207}Bi source recorded with the 6×6 Broadcom SiPM and GAGG-HR.

5.1.7 Americium-241

The ^{241}Am isotope decays into ^{237}Np via α-decay with BR(α) = 100%. The decay scheme of ^{237}Am is very complex. In the dominant α-decay mode, a 5.49 MeV α-particle is emitted and the daughter isotope ^{237}Np is created in an excited state with $J^P = 5/2^-$ that dominantly decays into the ground state under the emission of a 59.54 keV. Besides many other possible gamma transitions, there is a variety of conversion electrons that can be emitted in the ^{237}Am decay. The most intense radiation is [33]:

Type	Energy [keV]	Intensity [%]
α	5485.56	84.8
γ	59.54	35.9
γ	26.34	2.27
CE L	~ 13	17.4
CE L	~ 39	30.2

A recorded energy spectrum can be seen in figure 5.9. The 59.54 keV gamma line can be clearly identified at approx. 14 nVs. Other radiation contributions have even lower energies, such that they produce signals close to the noise level. Thus, other peaks cannot be identified in the spectrum.
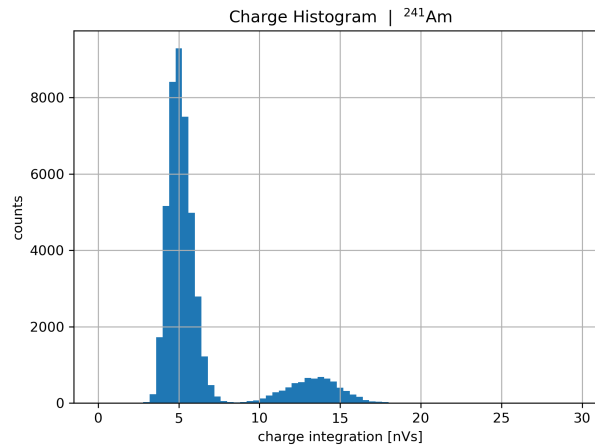
Figure 5.9: Energy spectrum of the ^{241}Am source recorded with the 6×6 Broadcom SiPM and GAGG-HR.

5.2 Scintillator Comparison

Important properties of the three scintillators available are listed in table 5.1. In the following, the emission spectrum, the light output, the decay constant and the energy resolution of the crystals will be compared and investigated. All of these are relevant properties that would play a crucial role for the construction of a Compton camera prototype.

5.2.1 Emission Spectra

While the emission spectrum of the two GAGG crystal versions is essentially identical, there is a huge difference between the emission of the GAGG crystals and the LGSO crystal. The GAGG crystals are opaque and appear in a yellow colour. Their emission peaks at a wavelengths of 530 nm [31]. The LGSO crystal on the other hand appears light grey and its emission spectrum peaks at 410 nm [30]. The emission spectrum of LGSO is similar to that of LYSO.

A picture of a GAGG and LGSO crystal is displayed in figure 5.10 on the left side. A comparison between the emission spectra of GAGG and LYSO can be found next to it in figure 5.10 as well.

The LGSO scintillator emits shorter wavelengths matching slightly better the spectral sensitivity of the Broadcom SiPMs depicted in figure 4.1 which peaks at about 420 nm. The dominantly yellow emission of
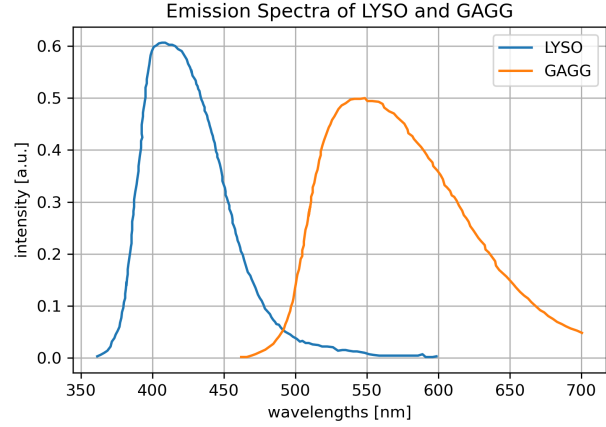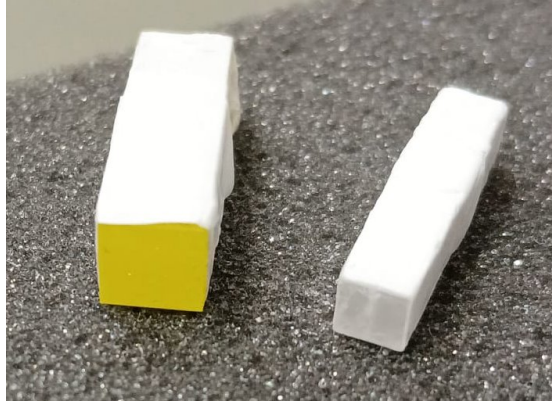
Figure 5.10: Left: Picture of a GAGG and LGSO crystal. Right: Comparison of the emission spectrum of GAGG and LYSO. The data for the GAGG spectrum was taken from [34] and for the LYSO spectrum from [35].

the GAGG scintillator matches slightly better with the spectral sensitivity of the Hamamatsu SiPMs which peaks at about 450 nm. However, both SiPM product types show generally good efficiency in the range of the emission spectra of both scintillators. The Broadcom SiPMs can reach slightly larger PDE values.
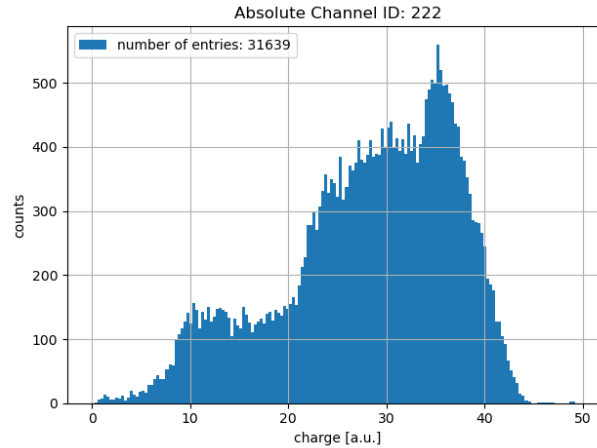
Figure 5.11: Charge spectrum of the LGSO background recorded using the TOFPET ASIC and the 4×4 Broadcom SiPM biased with 39 V. The spectrum was measured for a period of 5 min.

Unlike the GAGG scintillators, LGSO scintillators are self-radiative, thus there is an intrinsic background spectrum whenever an energy spectrum is recorded. A background spectrum was taken in figure 5.11. About 6,000 background events can be expected per minute.

5.2.2 Light Output Comparison

The light output is a crucial characteristic of a scintillator. As explained in section 2.4, it describes the amount of light emitted per unit energy that is deposited by the impinging particle. Generally, a high light output is beneficial since it improves the energy resolution. However, SiPMs or readout ASICs can only handle light signals within their dynamic range. Hence, a large light output might limit the detectable energy range, since the detection systems runs into saturation effects. To overcome this problem, the light output of a scintillator can be distributed to multiple SiPMs such that the signal is spread over multiple channels reducing the signal amplitude per channel. In such a case, the measurements of several coincident measurements have to be grouped together, which is further investigated in section 5.4.

The light output cannot be measured directly with the means available in this thesis, but the light output

can be compared between the three scintillators by taking energy spectra of the same source under equivalent operation parameters and comparing the measured charge values. Such a comparison can be made in figure 5.12 where three ^{137}Cs spectra a displayed taken with different scintillators but under otherwise identical conditions.
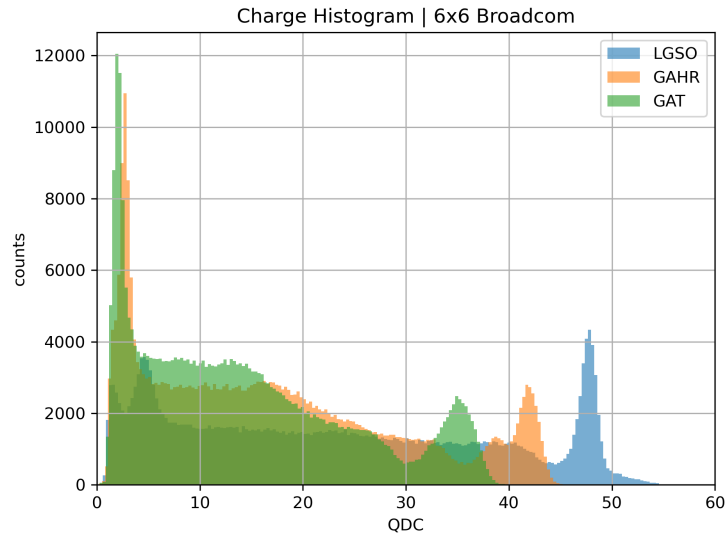

Figure 5.12: Comparison of the ^{137}Cs spectra recorded with the three different scintillators LGSO, GAGG-HR and GAGG-T using the 6×6 Broadcom SiPM biased with 39 V. The spectra were taken with the TOFPET ASIC for a measurement periode of 5 min.

In all three spectra, a gamma peak corresponding to an energy of 661.66 keV is visible. This suggests that LGSO has the largest light output followed by GAGG-HR. Evidently, GAGG-T has the lowest light output. For the LGSO scintillator, the exact light output value is not given in the data sheet [30]. The comparison in figure 5.12 implies that its light output is $> 50,000 \frac{\text{ph}}{\text{MeV}}$. However, one has to consider that the PDE of the SiPM depends on the wavelengths of the photons and that bias voltage settings are not equivalent across different wavelengths as demonstrated in section 4.5. This heavily limits the meaningfulness of the direct comparison between the GAGG spectra and the LGSO spectrum, especially since the 6×6 Broadcom SiPM has a higher PDE for the LGSO emission spectrum leading to higher charge measurements.

5.2.3 Decay Constant Comparison

The decay constant is a relevant parameter for the construction of a Compton camera, because it has an influence on the CTR of the camera. In the SCoKa prototype, coincidences between events in the scattering and absorption layer have to be detectable with a precision of about 1 ns. Hence, the detector to be constructed would profit from a small decay constant since this implies a fast scintillator response.

The means to measure the decay constant of a scintillator directly are currently not available, but comparative measurements can be done again by comparing the scintillation waveforms of the scintillators under identical conditions. Figure 5.13 shows 1,000 waveforms for each scintillator captured with the same settings and experimental setup. The exponential decay of the these waveforms which starts after about 100 ns is an overlay of the scintillator decay and the exponentially decaying SiPM signals itself. Let τ_D be the decay constant of this exponential. The model

$$V(t) = V_0 \cdot e^{-\frac{t}{\tau_\text{D}}} \tag{5.10}$$

was used and fitted to the data in figure 5.13 for $t > 100$ ns to obtain τ_D as a fit parameter for each wave. The distribution of these decay constants are displayed in figure 5.14 for all three scintillators.

The decay constant of the GAGG-HR crystal is longer than that of the GAGG-T crystal and the LGSO crystal has by far the fastest exponential decay. This is to be expected given the values in table 5.1. Since it
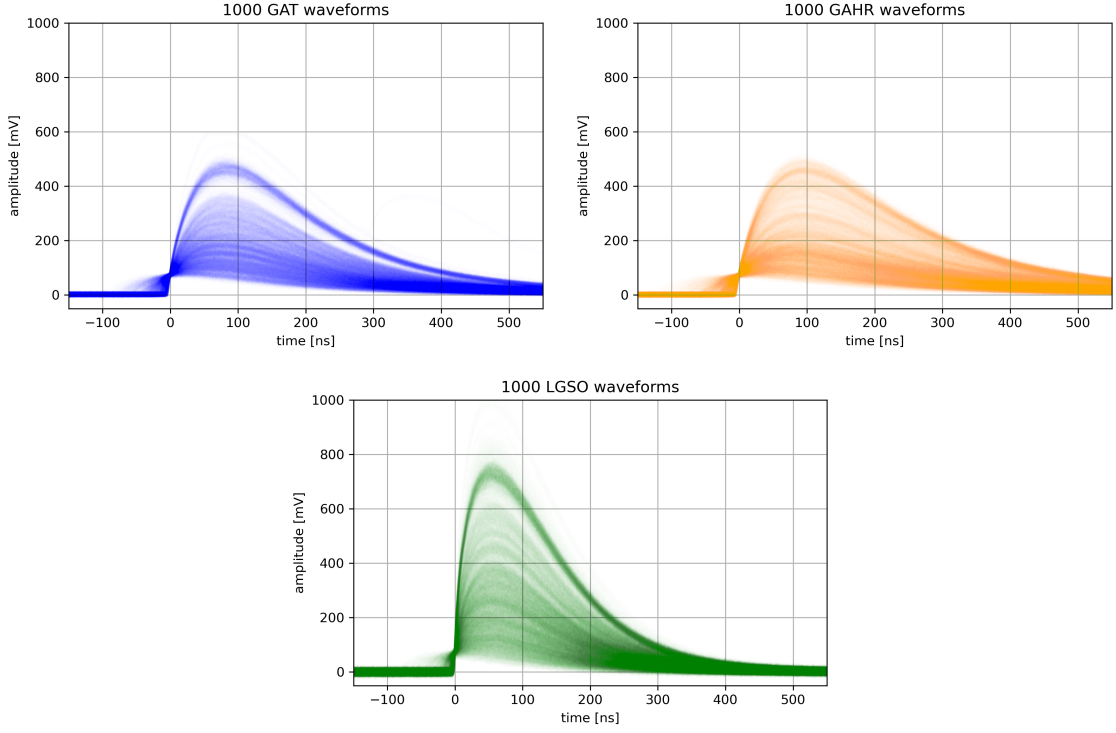
Figure 5.13: Overlays of 1,000 waveforms captured with the oscilloscope using the GAGG-T scintillator (blue), the GAGG-HR scintillator (orange) and the LGSO scintillator (green). The 6×6 Broadcom SiPM was biased with 41 V to capture waveforms of the ^{137}Cs source.

is not the decay constant of the scintillator directly that is measured but an overlay with the SiPM decay, the measured decay constants are generally bigger than the values given in table 5.1.

5.2.4 Energy Resolution Comparison

The energy resolution of the scintillator will determine the energy resolution of the absorption layer of the SCoKa device and thus the resolution on the measurement of the energy of the scattered photon. Due to equation (3.1), this energy resolution will contribute directly to the angular resolution of the camera. Thus the energy resolution is a very crucial scintillator characteristic. It is strongly related to the light output discussed in section 5.2.2, since the energy is measured by determining the number N of scintillation photons and the uncertainty of this number scales with $\sqrt{N}$, such that:

$$\frac{\Delta E}{E} \sim \frac{\Delta N}{N} = \frac{\sqrt{N}}{N} = \frac{1}{\sqrt{N}} \tag{5.11}$$

Hence the energy resolution improves for a larger light output.

The energy resolution can be measured from a gamma peak of a source spectrum by fitting a Gaussian distribution to the peak. When μ_{QDC} is the fit parameter corresponding to the mean of the Gaussian distribution, the energy resolution can be calculated from the FWHM with:

$$\frac{\Delta E}{E} = \frac{\text{FWHM}}{\mu_{\text{QDC}}} \tag{5.12}$$

However, equation (5.12) only holds for a linear behaviour between charge or QDC values and energy, which is not necessarily given as it will be demonstrated in section 5.3. Additionally, this relation only holds, if there is no offset in the calibration function, i.e. $b = 0$ for equation (5.15). Although the parameter b is generally small, it is nevertheless unequal to zero in many cases. Due to both of these aspects, the
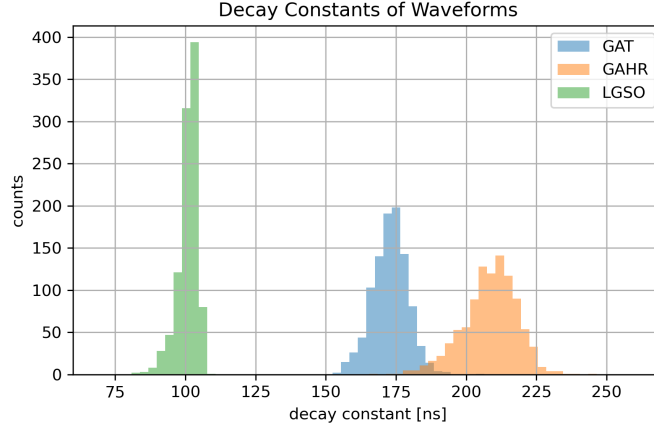
59

Figure 5.14: Comparison of the histograms for the obtained decay constants of the scintillation waveforms for GAGG-T and GAGG-HR.
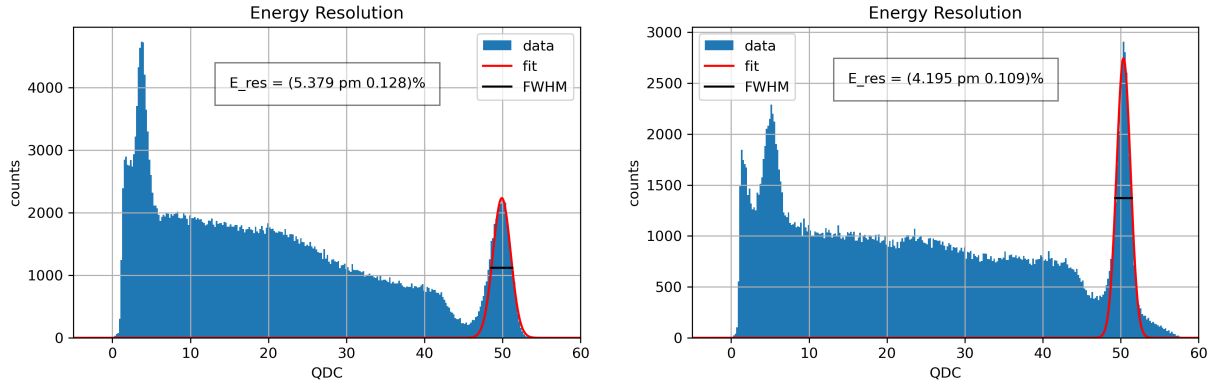

Figure 5.15: Energy spectra of ^{137}Cs recorded using GAGG-T (left) and LGSO (right). Both spectra were recorded using the TOFPET ASIC and the 6×6 Broadcom SiPM. For the LGSO spectrum, a bias of 39 V was used. For the GAGG-T spectrum, a bias of 41.5 V was used.

resolution defined in equation (5.12) is not an accurate measurement of the energy resolution, but still gives a grasp of the order of magnitude and can serve for comparative measurements between the scintillators.

It is common practice to measure the energy resolution at an energy of 662 keV using the pronounced gamma peak of a ^{137}Cs peak (see e.g. [36]). Under identical conditions, the 662 keV gamma peak in the LGSO spectrum is at the highest QDC values out of all the available scintillators as it could already be observed in figure 5.12. Since the LGSO and the GAGG emission spectrum is very different and bias voltage settings are not comparable for different wavelengths, completely identical settings do not lead to a meaningful comparison. As a general tendency, the detection of larger wavelengths also requires a higher bias voltage (see figure 4.31). Hence, the 6×6 Broadcom SiPM was biased with a larger voltage for the GAGG crystal in figure 5.15, such that the 662 keV gamma peak is around a QDC value of 50 in both spectra. The obtained resolutions

$$\frac{\Delta E}{E}(\text{GAGG-T}) = (5.4 \pm 0.2) \% \tag{5.13}$$

$$\frac{\Delta E}{E}(\text{LGSO}) = (4.2 \pm 0.1) \% \tag{5.14}$$

are close to each other and close to the resolution given in table 5.1. The resolution of the LGSO crystal is slightly better, but it has to be stressed again that the meaningfulness of this comparison is limited due to the reasons mentioned above.

The behaviour of the energy resolution at different energies can be explored by applying the same procedure to other peaks in the spectra of other radioactive sources. Results for the GAGG-T and LGSO scintillator are displayed in figure 5.16. The energy resolution was determined using equation (5.12) for each peak. Naturally, the resolution scales with $\frac{\Delta E}{E} \sim E^{-1}$.
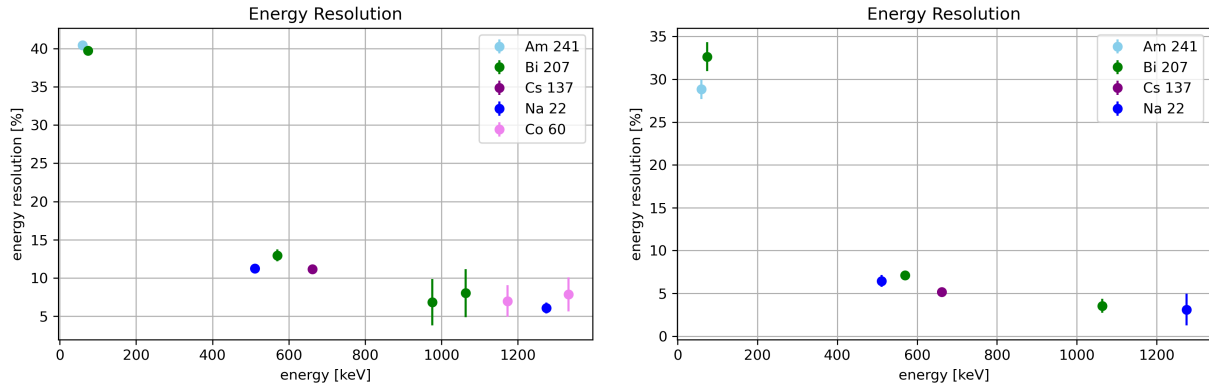

Figure 5.16: Energy resolution measured at different energies for the GAGG-T scintillator using the 6×6 Broadcom SiPM biased with 39 V (left) and the LGSO scintillator using the 6×6 Broadcom SiPM biased with 39 V (right).

5.3 Energy Calibration

The energy of a gamma will be measured in the absorption layer. However, the readout system (which is in this case the TOFPET ASIC) measures in values of QDC. Thus, a relation has to be determined translating these QDC values into an energy measurement.

An energy calibration for a system out of scintillator, SiPM and readout ASIC can be performed by measuring source spectra as demonstrated in section 5.1. The peaks in the spectra of the various sources need to be identified and assigned to an energy. In the previously discussed source measurements using the oscilloscope and the GAGG-HR scintillator, up to eleven radiation lines were intense enough to be detectable as a peak in a spectrum. They are listed in table 5.3. However, not all of these peaks are visible for every combination of scintillator and SiPM. For instance, it is impractical to measure the ^{60}Co source spectrum using the LGSO scintillator, because the background event rate of the crystal is higher than the rate of detected source events, hence only background-dominated spectra can be recorded. In addition, while peaks from conversion electrons are visible in spectra recorded with GAGG-HR, they do not appear in LGSO spectra.

Source	Type	Energy [keV]	Intensity [%]
^{22}Na	γ	511.00	176.90
	γ	1274.54	99.94
^{60}Co	γ	1173.23	99.85
	γ	1332.49	99.98
^{137}Cs	γ	661.66	85.10
	CE K	624.22	7.79
	γ	569.70	97.75
^{207}Bi	γ	1063.66	74.50
	CE K	975.65	7.08
	X-ray Kα	74.16	58.21
^{241}Am	γ	59.54	35.9

Table 5.3: Detectable energy peaks in the spectra of the available radioactive source with their corresponding energy.

The QDC value that corresponds to the energy of a peak can be found by fitting a Gaussian function to that specific peak. Peaks that are very close together, such as the two gamma lines of the ^{60}Co source, require the use of a multi-Gaussian fit function to model the overlay of the adjacent peaks as well. Each peak gives a data point for the estimation of an energy calibration function that relates QDC values to measured energy.

All components, the scintillator, the SiPM and the readout ASIC can have non-linear effects. The light output of the scintillator can be assumed to be widely linear with energy, thus non-linear effects are neglected for the scintillation light output in the scope of this thesis. The non-linear behaviour of SiPMs has been described in section 2.3.5. Due to a limited amount of SPADs in the SiPM, there is a saturation effect in the detected photon number for larger light signals.
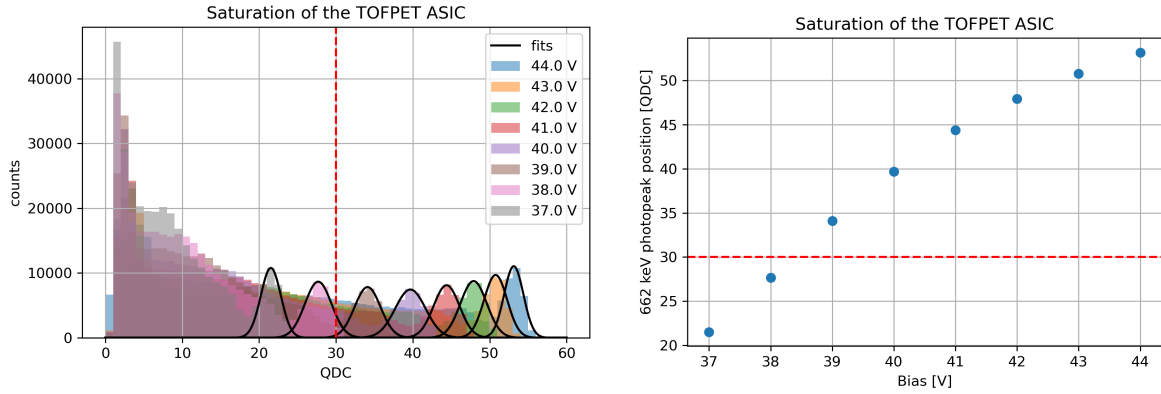
Figure 5.17: Demonstration of the saturation effect of the TOFPET ASIC. Left: An overlay of many ^{137}Cs spectra measured at different bias voltages is displayed together with the determined positions of the 662 keV photopeaks. For QDC values above 30, the spectrum is squeezed. Right: The 662 keV photopeak position versus the bias voltage.

The TOFPET ASIC also suffers from saturation effects for QDC values above 30 similar to the SiPM behaviour. This can be observed in figure 5.17. Multiple spectra of the ^{137}Cs source have been recorded using the GAGG-T scintillator and the 6×6 Broadcom SiPM read out with the TOFPET ASIC. The bias voltage was gradually increased to reach larger signal amplitudes and thus observe the saturation behaviour of the ASIC. For QDC values above 30, the high energy end of the ^{137}Cs spectrum becomes increasingly compressed. Gaussian functions were fitted to the 662 keV photopeaks of each spectrum to determine the peak position in units of QDC. The result is displayed in figure 5.17 on the right side demonstrating that the relation between energy and QDC is not linear any more for QDC > 30 since these values are out of the dynamic range of the TOFPET ASIC.

The saturation behaviour of the ASIC can be modelled in the same fashion as the behaviour of the SiPMs. Thus the overlay of both non-linear effects can be capture in a calibration function similar to equation (2.30)

$$\text{QDC}(E) = A \cdot \left(1 - e^{-k \cdot E}\right) + b, \tag{5.15}$$

where A, k and b are real parameters. An exemplary fit to data points obtained from the analysis of energy spectra using the 6×6 Broadcom SiPM and the GAGG-T scintillator can be seen in figure 5.18. In this case, the fit parameters

$$A = (65.36 \pm 1.32) \text{ QDC} \tag{5.16}$$

$$k = (10.77 \pm 0.47) \cdot 10^{-4} \text{ keV}^{-1} \tag{5.17}$$

$$b = (-0.68 \pm 0.40) \text{ QDC} \tag{5.18}$$

were obtained. The saturation level $A = (66.34 \pm 1.32)$ QDC indicates the limit up to which QDC values can be measured by the detection system. The calibration function asymptotically approaches this level, which consequently also limits the energy range that can be measured. The closer the measured QDC value is to the saturation level, the worse is the energy resolution.
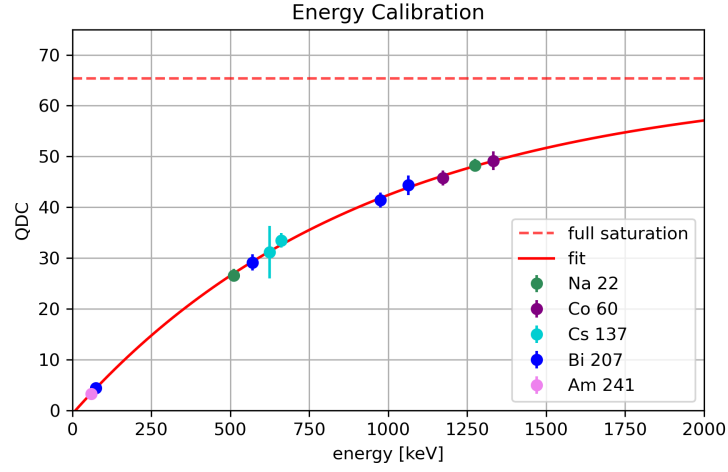
Figure 5.18: Energy calibration of the 6×6 Broadcom SiPM and GAGG-T scintillator.

For the SCoKa project, the detection of high energetic photons is of special interest. An incident photon will lose a large portion of its energy in the scattering layer such that the scattered photon which is to be detected in a scintillator-based absorption layer will already be less energetic. Still, in order to achieve an imaging for photons above 1 MeV, a good energy resolution around 1 MeV and preferably even above is essential. Thus, this saturation behaviour and calibration functions under different settings are to be investigated in more detail in the following subsections.

The inverse function of equation (5.15)

$$E(\text{QDC}) = \frac{1}{k} \cdot \ln\left(\frac{A}{A + b - \text{QDC}}\right) \tag{5.19}$$

can be used to transfer QDC values into the measured energy. In figure 5.19, a charge spectrum of the ^{22}Na was converted into an energy spectrum using the obtained parameters in equation (5.16) to (5.18).
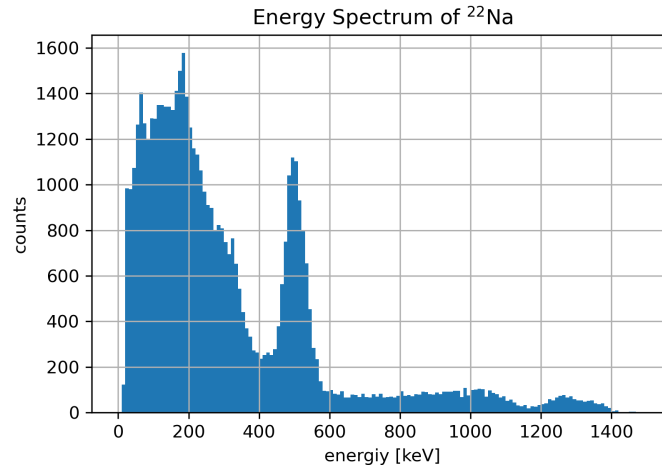
Figure 5.19: Measured energy spectrum of ^{22}Na.

5.3.1 Calibration for Different SiPMs

Figure 5.20 displays the results from an energy calibration of the two larger sized Broadcom SiPMs and the Hamamatsu SiPM. In all cases, the GAGG-T scintillator was used. The saturation behaviour towards higher energies is clearly observable. Interestingly, both Broadcom SiPM calibration functions have a similar

saturation level although the 4×4 Broadcom SiPM has only about 37% of the SPADs of the 6×6 Broadcom SiPM.

$$A_{6x6}^{GAT} = (65.36 \pm 1.32) \text{ QDC} \tag{5.20}$$

$$A_{4x4}^{GAT} = (64.92 \pm 3.36) \text{ QDC} \tag{5.21}$$

Additionally, in the range of measured radiation lines, the calibration function of the 4×4 Broadcom SiPM behaves approximately linear while the measured QDC values are mostly below 30. This suggests, that the saturation effect mainly originates from the ASIC and not from the SiPMs in these cases.
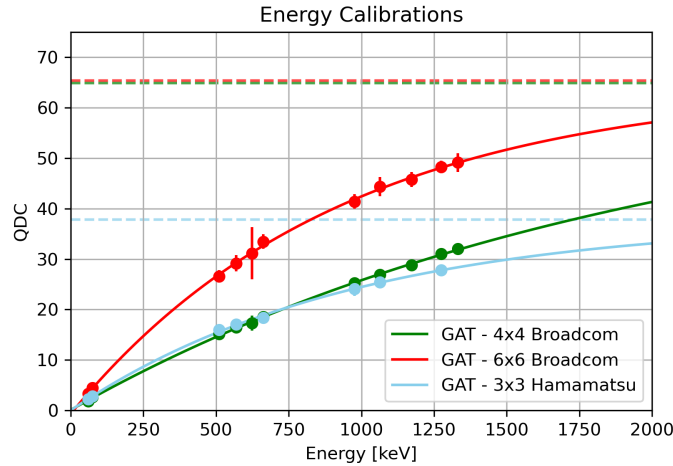
Figure 5.20: Comparison between the energy calibration of the 4×4 and the 6×6 Broadcom SiPMs biased with 39 V as well as the 3×3 Hamamatsu SiPM biased with 56 V. The GAGG-T scintillator was used in all cases.

The calibration function of a 3×3 Hamamatsu SiPM is displayed in figure 5.20 as well. In this calibration function however, a much lower saturation level is observable with $A_{3x3}^{GAT} = (37.83 \pm 1.17)$ QDC. The calibration function behaves non-linearly even below QDC values of 30 where all the data points have been measured. This implies that in this case the saturation behaviour originates mainly from the SiPM. The Hamamatsu SiPM has a smaller total area and relatively large SPAD size compared to the Broadcom products (75 µm compared to 40 µm) such that the 3×3 Hamamatsu SiPM has only about 19% of the number of SPADs of the 4×4 Broadcom SiPM. Thus, the two Broadcom SiPMs show a much more desirable saturation behaviour than the Hamamatsu SiPM.

5.3.2 Calibration for Different Scintillators

Calibration functions obtained for different scintillators can be compared in figure 5.21. Comparing the two functions determined for the 6×6 Broadcom SiPM, both the function for the GAGG-T (red) and of the GAGG-HR (blue) scintillator have a very similar behaviour with similar saturation levels:

$$A_{6x6}^{GAT} = (65.36 \pm 1.32) \text{ QDC} \tag{5.22}$$

$$A_{6x6}^{GAHR} = (64.67 \pm 1.48) \text{ QDC} \tag{5.23}$$

Since the light output of the GAGG-HR crystal is larger than that of the GAGG-T crystal, the QDC values of the GAGG-HR function are generally higher as well.

Using the 4×4 Broadcom SiPM, the calibration function of GAGG-T (green) has a similar saturation level as the previously discussed functions with $A_{4x4}^{GAT} = (64.92 \pm 3.36)$ QDC, although the saturation level is reached much slower. The calibration function of the LGSO crystal (yellow) saturates at a level of $A_{4x4}^{LGSO} = (48.60 \pm 0.39)$ QDC already which is far below the saturation level of the other scintillators. However, less data points are available for the calibration of an LGSO-based detection system since conversion electrons cannot be identified in the LGSO spectra and the ^{60}Co source cannot be used at all. Thus, the saturation behaviour is scanned less precise especially in the high energy range.
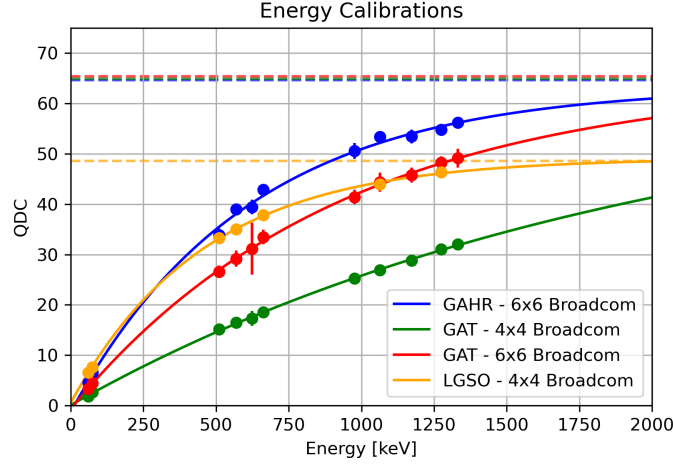
Figure 5.21: Comparison between energy calibrations using the 6×6 and 4×4 Broadcom SiPMs biased with 39 V and different scintillators.

5.3.3 Calibration for Different Bias Voltages

The influence of the bias voltage on the energy calibration can be observed in figure 5.22 where calibration functions of the LGSO scintillator read out by the 4×4 Broadcom SiPM are compared. The higher the bias voltage, the higher are the amplitudes of the SiPM signals. Consequently, QDC values are higher for larger bias voltages such that the saturation level is reached faster.
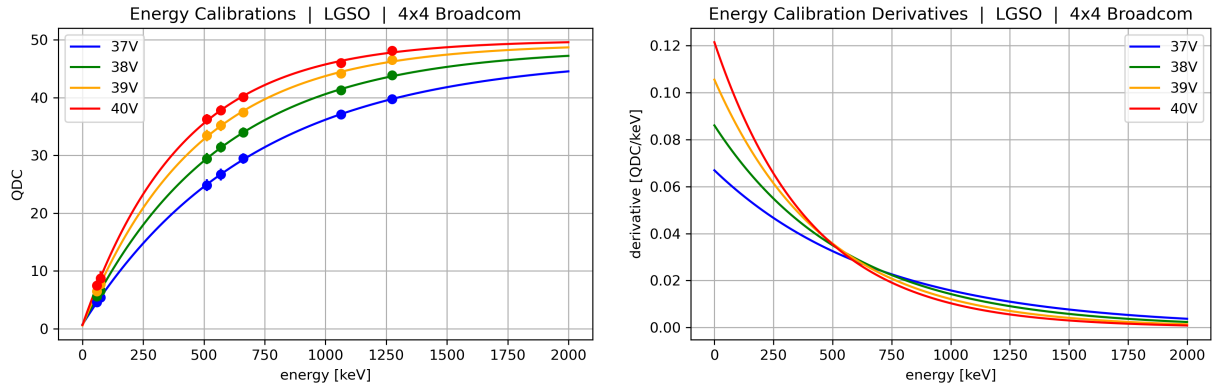
Figure 5.22: Left: Comparison between energy calibrations using the 4×4 Broadcom SiPM and the LGSO crystal but different bias voltages. Right: Derivatives of the calibration functions.

The resolution of the translation of QDC values into energies improves if the slope of the calibration function is large. To compare energy regions, in which a certain bias voltage setting might be beneficial, the derivative of the function in equation (5.15)

$$\frac{\mathrm{d}}{\mathrm{d}E}\mathrm{QDC}(E) = Ak \cdot e^{-kE} \tag{5.24}$$

was plotted in figure 5.22 as well. While larger bias voltages are generally better at resolving small energies, a reduced bias voltage delays the saturation of the system and is thus slightly beneficial for the measurement of larger energies. In this case, a bias voltage of 37 V outperforms voltages $\geq$ 38 V for energies above 750 keV. However, the bias voltage cannot be reduced arbitrarily low since the PDE of the system depends on the bias voltage too, which effects the energy resolution as well. It has only been shown that reducing the bias voltage can counteract the saturation behaviour to some degree.

5.4 Light Signal Spread with the Hamamatsu SiPM Array

The footprint of the scintillator crystals is bigger than the dimensions of the Hamamatsu SiPMs. The GAGG-T crystal with a footprint of 6×6 mm^2 can cover four SiPMs of the 4×4 array completely. Thus, the light signal of the scintillator is spread over multiple SiPMs. In a possible design of the absorption layer, a matrix of scintillators is coupled to a matrix of SiPMs with a light spreading material in-between. The Hamamatsu SiPM array gives rise to the opportunity to already study the light signal propagation of one scintillator onto multiple SiPMs.

The reconstruction of the light signal distribution is possible since the TOFPET ASIC assigns a time stamp to every measurement as well as a channel number. The time stamp can be interpreted as the time-of-arrival (ToA). Table 5.4 shows the arrangement of channel IDs that is needed to map the channel number to its position in the array. Depending on which port the TOFPET module is connected to the FPGA, the channel ID might differ from the *absolute* channel ID. One FEB/D front-end board provides eight ports (port F1 to F8) for the connection of TOFPET modules. Each module can host up to two ASICs. Thus, up to 16 ASICs can be evaluated by a single FEB/D front-end board. The slave and port ID provide the possibility to differentiate between multiple interconnected FEB/D boards and DAQ ports. In the scope of this thesis, only one FEB/D board is used such that the slave and the port ID are always 0. The absolute channel ID can then be calculated by:

$$\text{Absolute Channel ID} = \text{Channel ID} + 64 \times \text{Chip ID} \tag{5.25}$$

Thus, depending on which port is used, a multiple of 64 might need to be added to the channel IDs in table 5.4.

58	62	44	55	17	13	2	4
60	56	49	59	24	11	0	3
63	61	35	45	21	29	9	5
57	53	39	43	23	27	7	1
52	46	37	41	19	25	8	14
54	40	33	47	15	31	6	20
32	48	51	34	28	30	26	10
36	42	38	50	12	18	22	16

Table 5.4: Arrangement of the channel IDs in the TOFPET readout system.

The bias voltage can be set for each ASIC individually. This allows to read out different types of SiPMs simultaneously with the FEB/D board, which might be necessary in the future. The bias settings can be changed in the `bias_settings.tsv` file. However, to identify the ASIC, a slot ID is needed instead of the chip ID. The correlation of the slot and chip ID for the different ports is listed in table 5.5.

	Port F1	Port F2	Port F3	Port F4	Port F5	Port F6	Port F7	Port F8
1st Chip ID	0	2	4	6	8	10	12	14
2nd Chip ID	1	3	5	7	9	11	13	15
1st Slot ID	6	4	2	0	14	12	10	8
2nd Slot ID	7	5	3	1	15	13	11	9

Table 5.5: Arrangement of the chip and slot IDs on the FEB/D front-end board.

With table 5.4, it is possible to reconstruct the position of each SiPM and create hitmaps. For the plots in figure 5.23, the GAGG-T scintillator was placed on different positions of the 4×4 SiPM array of Hamamatsu. The scintillator was aligned with each corner. The scintillator covered four SiPMs of the array completely. The scintillator position is reflected in the hitmaps in figure 5.23, since the SiPMs that are directly facing the scintillator detect most of the signal. Some scintillation light is evidently also detected by neighbouring

channels which implies that there is a small light spread which probably mainly originates from the coupling with the silicone grease.
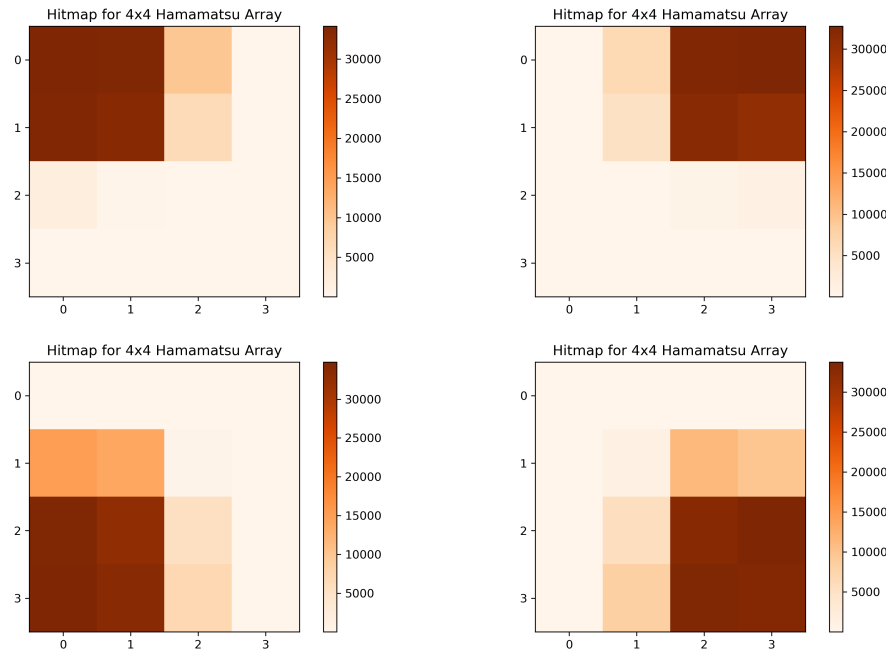

Figure 5.23: Hitmaps for an the array of 4×4 SiPMs from Hamamatsu. The position of the scintillator that was placed on top of the SiPM array can be reconstructed.

In the future, it might be beneficial to deliberately increase the signal spread, i.e. to distribute the scintillation light over more SiPMs, to avoid reaching the saturation level of the ASIC or SiPM and hence to improve the resolution of the energy measurement as it was discussed in section 5.3. In addition, the signal spread over several channels can improve the reconstruction of the interaction position (i.e. of the absorption point) in the future. A light spreading material can be inserted between scintillator and SiPM array. The scintillator was placed in a central position covering the four innermost SiPMs of the array. Figure 5.24 shows a comparison between a hitmap with and without light spreader, where the effect can be observed that events are detected slightly less dominantly in the central region and slightly more frequently in peripheral channels.
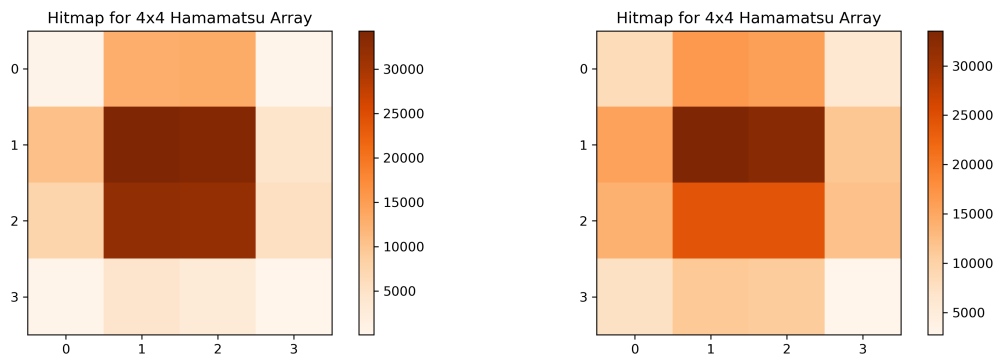
Figure 5.24: Hitmaps for a central scintillator position without (left) and with (right) light spreading material between scintillator and SiPM array.

5.4.1 Time of Arrival

Since the light signal is spread over multiple SiPMs, it is necessary to analyse the ToA of each measurement in order to find measurements that belong to the same event of scintillation light emission. A coincidence time window needs to be determined, i.e. a time frame in which measurements are considered to originate from the same event. It is desirable to keep this time window as small as possible in order to reduce the probability that dark count events are included in the measurement. Also, one has to be able to find coincidences between the scattering and absorption layer with a 1 ns precision in the future Compton camera prototype.
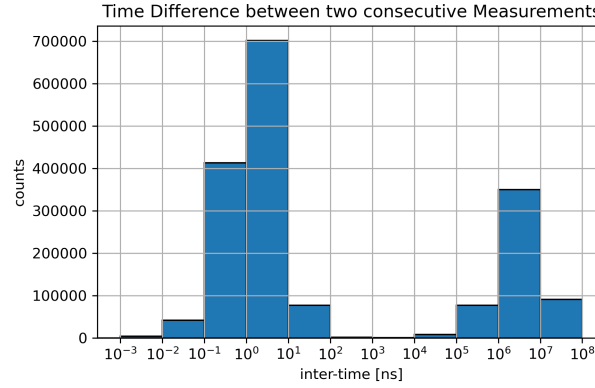
Figure 5.25: Inter-time distribution of a source measurement done with the GAGG-T scintillator placed in the middle of the 4×4 Hamamatsu SiPM array.

The GAGG-T scintillator was placed on top of the four central SiPMs of the Hamamatsu SiPM array. The ^{207}Bi source was measured for 1000 s in QDC mode with this setup. The SiPMs were biased with 56 V. The inter-time is determined by taking the difference of two consecutive ToA stamps. The obtained distribution of the inter-time can be seen in figure 5.25. It can be seen that the inter-time distribution can be divided into a fast and a slow region. The slow region ($> 10^4$ ns) corresponds to time distances between two consecutive scintillation light events. Inter-times in the fast region ($< 10^2$ ns) mainly belong to two measurements of the same event spread into different SiPM channels. The fast region is plotted with linear binning in figure 5.26. It can be observed that most inter-times are measured below 10 ns. Thus, events that arrive within a 10 ns time window will be considered to be coincident in the following.
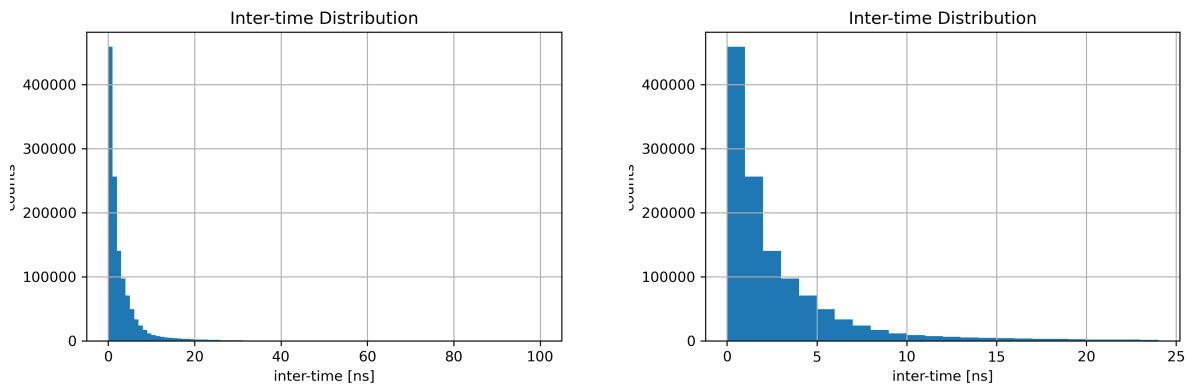
Figure 5.26: Inter-time distribution in linear binning focusing on the fast region below 100 ns.

Figure 5.27 displays the number of hit SiPM channels within the coincidence window. Measurements that are not coincident with another measurement (i.e. when no other measurement was found within the next 10 ns) were discarded for this plot. Imposing that no channel can contribute two measurements in the same coincidence time window leads to an additional condition. It can be seen that the signal is spread

mostly between three or four SiPM channels. Since the scintillator was placed directly above the four central SiPMs, these channels have the highest probability of measuring an event. Occasionally, the signal is spread to even more SiPMs as it is also observed in figure 5.23. In addition, dark count events could have occurred in some coincidence time windows as well.
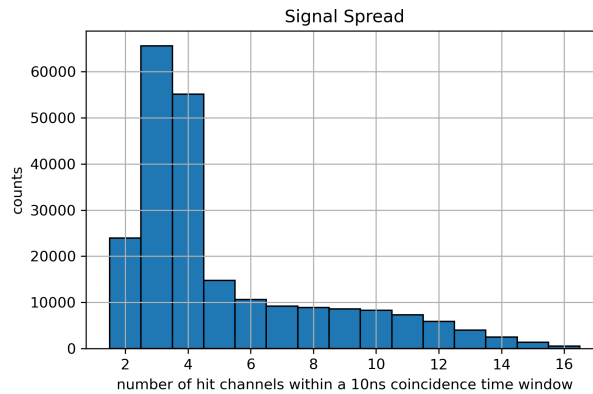

Figure 5.27: Number of hit channels within the coincidence time window of 10 ns

5.4.2 Data Grouping in a SiPM Array

Since the signal is spread out over multiple SiPMs, coincident measurements need to be combined in order to capture the full information of the scintillation light signal. The PETsys GUI provides an in-built data processing function that groups data in a certain coincidence time window simply by summing the data up. However, the sum of coincident QDC measurements is only meaningful, if the relation between QDC values and energy can be assumed to be linear which is not the case as it was extensively demonstrated in section 5.3. Instead, the saturation behaviour of the detection system would lead to larger QDC values if the light signal is more spread out compared to the case where the same light signal is entirely captured by one SiPM channel only.

Thus, coincident QDC measurements have to be re-weighted based on the calibration function before summing them. Each QDC measurement is converted to a re-weighted QDC value using the inverse function in equation (5.19). These re-weighted QDC values can be arbitrarily scaled, since another energy calibration would be needed to assign a direct physical meaning to them. A scaling factor of 1/4 was applied. The data is then grouped by summing these re-weighted and re-scaled QDC values.
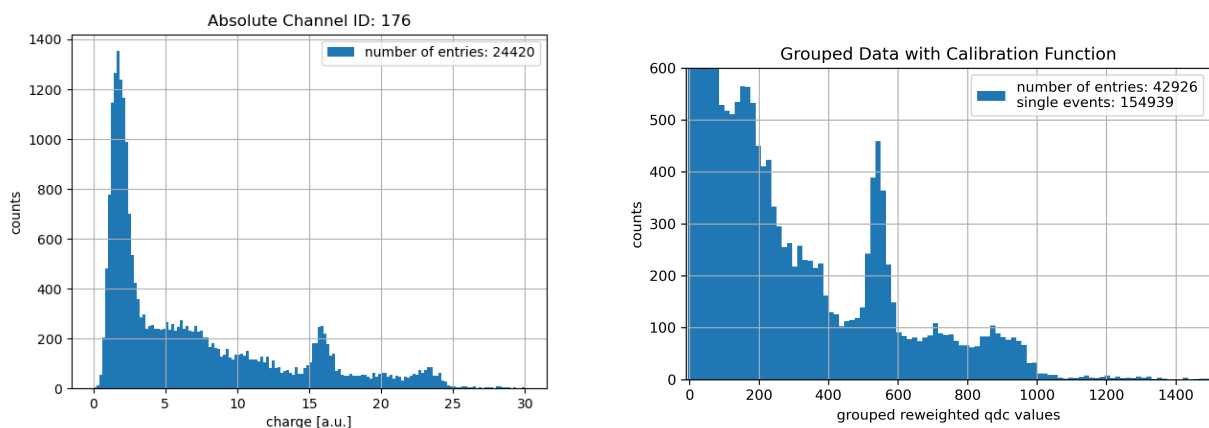
Figure 5.28: Left: Spectrum of the ^{207}Bi source using a single SiPM channel that was completely covered by the GAGG-T crystal. Right: A spectrum using the same data but grouping coincident measurements of all SiPM channels.

69

Figure 5.28 shows exemplary spectra of the ^{207}Bi source. The spectrum on the left side was recorded by a single channel. The spectrum on the right resulted from the data grouping process described above. The characteristic photopeak at an energy of 570 keV is more defined in the spectrum of the grouped data. However, neither the 1064 keV photopeak and nor the peak created by 976 keV conversion electrons is clearly identifiable in both spectra. One issue of the grouping process that is still to be solved is that the different SiPM channels require different calibration functions. The saturation behaviour varies between different channels and thus QDC measurements have to be re-weighted with a channel-specific calibration function. Determining a calibration function for all 16 SiPM channels of the Hamamatsu SiPM array would be required to improve the spectrum in figure 5.28. With the current approach, the spectrum is dependent on the scintillator position as it can be seen in the comparison in figure 5.29. The 570 keV photopeak is clearly at different QDC positions in the two spectra that are compared.
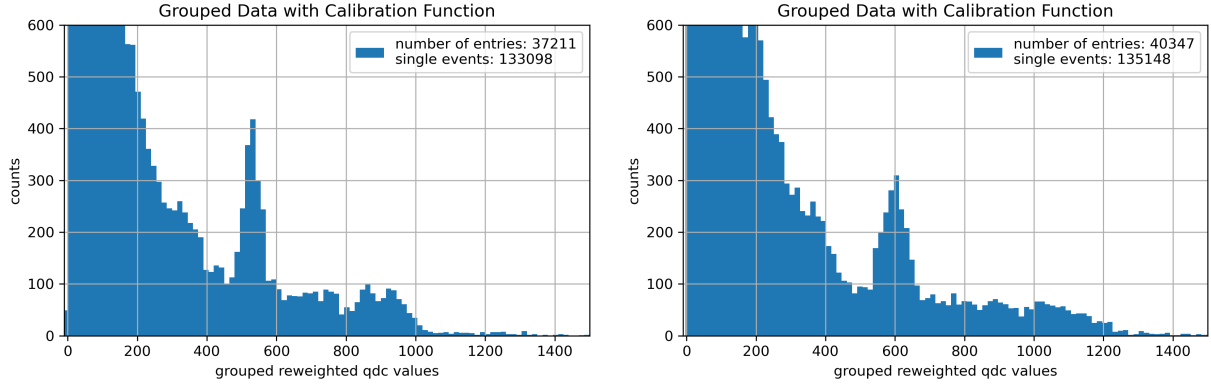
Figure 5.29: Spectra of the ^{207}Bi source obtained for the explained data grouping process. The left spectrum was obtained by putting the scintillator in one of the corners of the array, the right spectrum by placing it in a central position.

5.5 DOI Measurements

The absorption layer has to measure the energy as well as the absorption point of the scattered photon. There are many concepts for the reconstruction of the absorption point. The currently planned design of the Compton camera prototype intents to use segmented scintillator crystals in a matrix structure for the construction of the absorption layer. The x and y position of the absorption point can be determined e.g. by the centre of gravity method. A z coordinate could be estimated e.g. by taking the ratio between the sum of all SiPM signals and the maximum signal as it was done e.g. in [37]. The precision of this method is however rather limited.

In order to get a more precise information about where in the scintillator an interaction has happened, one can use a double-sided SiPM readout method. By comparing the pulse height on both sides, the depth of interaction (DOI), i.e. the position of the interaction along the axis between both SiPMs (z-axis), can be determined.

The pulse height ratio (PHR) depends on the point of interaction due to attenuation in the scintillator material, which is described by the attenuation law in equation (2.1). Together with the characteristic attenuation length l_0 of the scintillator, the number of photons that reaches the left and right SiPM can be determined with

$$N_{\text{left}} = N \cdot e^{-\frac{l/2-s}{l_0}} \tag{5.26}$$

$$N_{\text{right}} = N \cdot e^{-\frac{l/2+s}{l_0}} \tag{5.27}$$

where l is the length of the scintillator and s is the offset position, i.e. the distance of the interaction point from the centre of the scintillator. Let Q_{left} and Q_{right} be the measured QDC value of the left and right SiPM

channel respectively. For the PHR, a reference SiPM has to be defined, e.g. the left SiPM, such that:

$$\text{PHR} = \frac{Q_{\text{left}}}{Q_{\text{left}} + Q_{\text{right}}} \tag{5.28}$$

Since $Q_i \sim N_i$, the PHR is described through the following function of the offset s:

$$\text{PHR}(s) = \frac{N_{\text{left}}}{N_{\text{left}} + N_{\text{right}}} = \frac{e^{-\frac{l-2s}{2l_0}}}{e^{-\frac{l-2s}{2l_0}} + e^{-\frac{l+2s}{2l_0}}} = \frac{e^{\frac{s}{l_0}}}{e^{\frac{s}{l_0}} + e^{-\frac{s}{l_0}}} \tag{5.29}$$

Exemplary PHR functions for different attenuation lengths l_0 are displayed in figure 5.30. For offset values $s \ll l_0$, the PHR function can be approximated by a linear function.
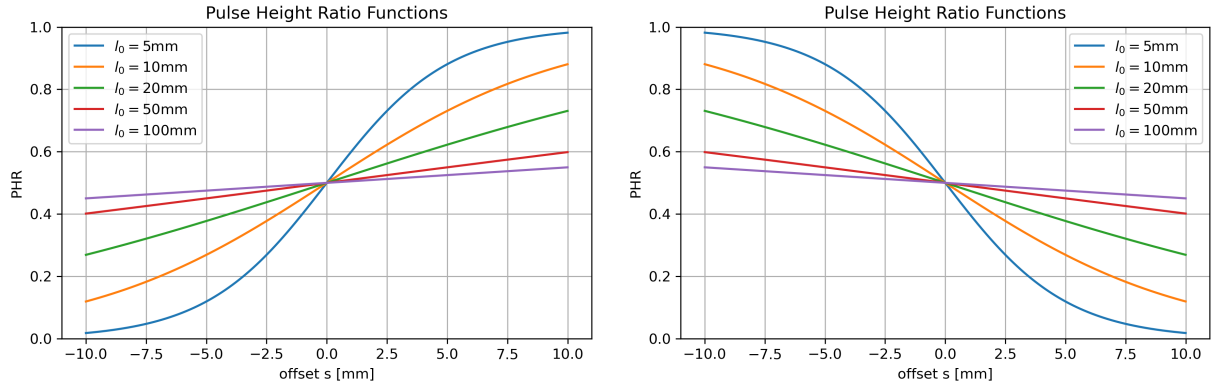
Figure 5.30: PHR functions as formulated in equation (5.29) for different characteristic attenuation lengths l_0. For the functions on the left side, the left SiPM is defined as the reference SiPM. For the functions on the right side, the right SiPM is defined as the reference SiPM.

5.5.1 Experimental Setup for DOI Measurements

The experimental setup for the DOI measurements is depicted in figure 5.31. The GAGG-T scintillator was readout on both sides by two 6×6 Broadcom SiPMs biased with $39\,\text{V}$ each. The SiPMs were read out by the TOFPET ASIC in QDC mode. Each measurement is hence assigned to a ToA which was used to find coincidences in a $10\,\text{ns}$ time window between the two attached SiPMs.
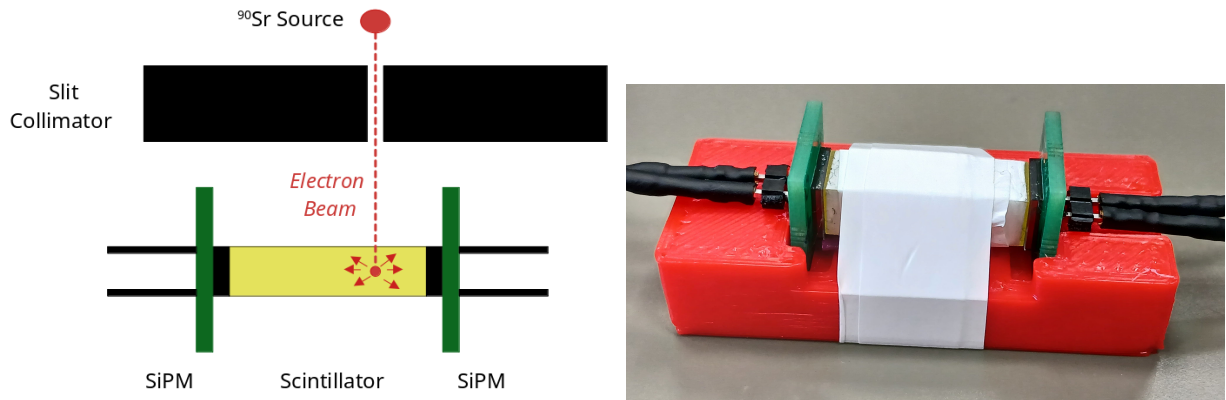
Figure 5.31: Schematic of the setup for DOI measurements (left) and picture of the 3D print for the stability of the SiPM-scintillator coupling (right).

A dedicated 3D-printed setup was designed to keep the SiPMs closely coupled to the scintillator and to avoid measurement errors due the a displacement of the scintillator crystals. The SiPMs together with the

scintillator were attached onto a screw slide table where the position along an axis can be changed with a 100 μm precision.

A ^{90}Sr source was used to create interactions in the scintillator material. The ^{90}Sr source used in these measurements is already collimated by its packaging but was further collimated using a slit collimator. Two thick lead blocks were aligned to form the slit collimator. The ^{90}Sr was chosen over the other sources for this type of measurement since electrons are easier to screen compared to gamma radiation such that an β-source can be collimated more effectively. For the success of the measurement, it is essential that the particle beam is collimated as narrow as possible so that the interaction point in the scintillator is precisely determined.
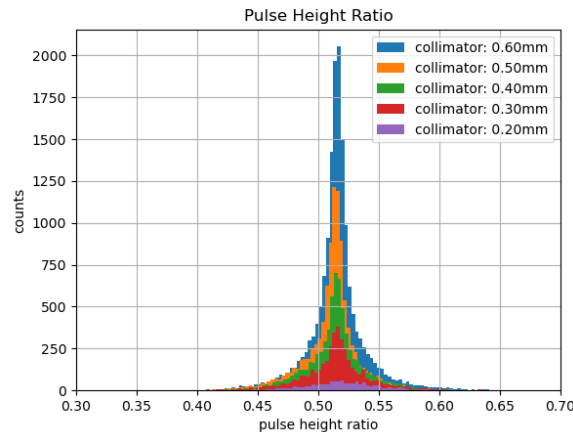
Figure 5.32: Pulse height spectra recorded for different collimator slit sizes.

For test purposes, the centre of the scintillator was aligned with the collimator slit (corresponding to $s = 0$) and pulse height spectra, i.e. histograms of the obtained PHRs, were recorded for different collimator slit sizes with a measurement period of 5 min each. The result can be seen in figure 5.32. For a slit size of 0.2 mm, almost no electrons from the ^{90}Sr source reach the scintillator such that hardly any coincidences are detected. For future measurements, the collimator slit was set to 0.5 mm as a compromise between a narrow electron beam and sufficient statistics.

5.5.2 DOI Measurement Results

DOI measurements were performed by recorded pulse height spectra for different source positions. Results are displayed in figure 5.33. The offset position was changed in steps of 2 mm. The left side shows the obtained pulse height spectra. In order to determine the mean PHR, a Gaussian function was fitted to the pulse height spectrum which is then plotted against the different offset positions on the right side. The error bars include the peak width σ from the Gaussian fit.

The PHR obtained for $-6\,\text{mm} \leq s \leq 6\,\text{mm}$ follows a linear function. This is to be expected. The characteristic attenuation length of GAGG was measured to be $l_0 = (645 \pm 26)$ mm in [34]. Thus $s \ll l_0$ should be valid for the entire dimension of the scintillator crystal. The measurement becomes less precise towards the edges of the scintillator. For $s = 10\,\text{mm}$ and $s = -10\,\text{mm}$, the electron beam was shot directly onto the scintillator's edge. For $s = 12\,\text{mm}$ and $s = -12\,\text{mm}$, the electron beam was shot past the scintillator in a 2 mm distance. Figure 5.34 shows the number of detected coincidences, which is constant for $-6\,\text{mm} \leq s \leq 6\,\text{mm}$ but falls off towards the edges. While significantly less coincidences have been measured for $s = 12\,\text{mm}$ and $s = -12\,\text{mm}$, there are still around 3,000 coincidences evident implying that the electron beam profile is still quite wide.

An additional issue is that the two faces of the GAGG-T crystal are not equally well polished, which effects the quality of the DOI measurement as well. The results in figure 5.33 suggest that a double-sided SiPM readout is not worth the effort, especially when considering that it would require twice the amount of SiPMs and readout channels (and thus double the costs). Currently, the peak width of the PHR distribution is bigger than the change of the mean PHR within 2 mm. Thus, the additional spatial information that can
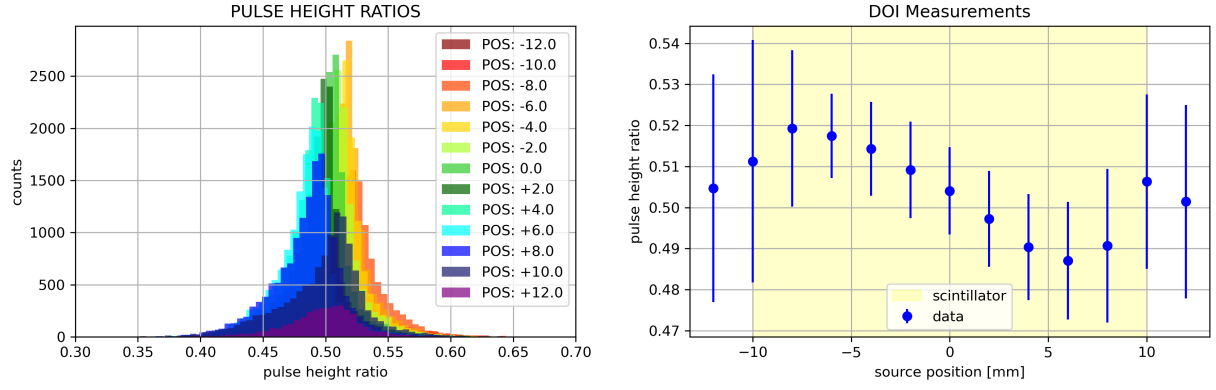
Figure 5.33: Left: Pulse height spectra obtained for different offset positions. Right: Determined mean PHR versus the source position.

be gained from this is very limited. However, groups using similar setups have reported to achieve a spatial resolution of 2 mm, e.g. [37], in their DOI measurements. In the future, this has to be re-investigated again, using a scintillator with two equally well polished sides and an improved collimation of the electron beam.
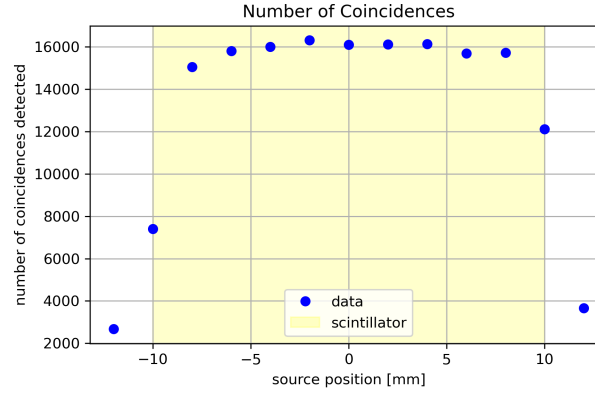

Figure 5.34: Number of coincidences detected at different offset positions.

5.5.3 Optical Cross Talk Increase

The optical cross talk can increase in a double-sided SiPM readout method. Photons that are created in an avalanche in an APD can propagate through the scintillator and reach the other SiPM. This effect was investigated by irradiating the double-sided SiPM readout setup with the ^{137}Cs source. The measurement was done three times. The first time, both SiPMs were biased. The second time, the left SiPM was turned off (but still coupled to the scintillator) so that only the right SiPM was recording a source spectrum. Lastly, the left SiPM was biased again and the right SiPM was turned off. The obtained spectra for each case are displayed in figure 5.35. The optical cross talk between the two SiPMs is clearly visible. Both SiPM channel measured larger QDC values in case both SiPMs were biased and producing avalanches.

5.6 Conclusion of the Scintillation Light Readout

Both, the LGSO and the GAGG crystals show promising characteristics for the use in the SCoKa absorption layer, combining a large light output and good energy resolution with a fast time response. In addition, both the 6×6 and the 4×4 Broadcom SiPMs can be used for an effective readout of the scintillation light. The 2×2 Broadcom SiPM is unsuitable because of its small fill factor.
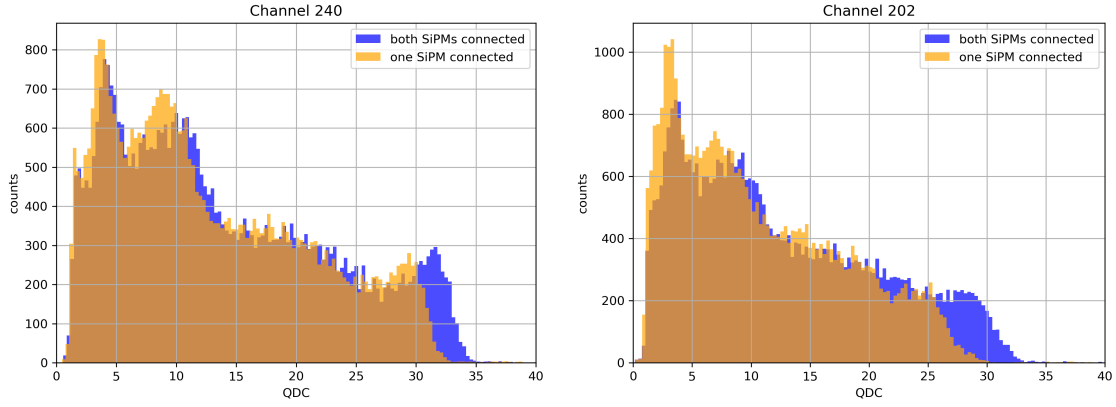
Figure 5.35: Spectra of the ^{137}Cs source recorded in a double-sided SiPM readout setup where both SiPMs were biased and only SiPM was biased respectively demonstrating the increase of optical cross talk.

Good results have been obtained using the TOFPET ASIC. It can provide multi-channel readout and gives rise to the opportunity to analyse the ToA of signals and group data within a coincidence time window. A drawback is the limited dynamic range of the ASIC which already saturates for light signals corresponding to energies below 1 MeV. The saturation level of the ASIC is reached less quickly when distributing the light of one scintillator to several SiPMs which is beneficial for the detection of high energetic photons.

Other ASICs might outperform the dynamic range of the TOFPET v2c which has to be investigated in the future. A possible alternative is the KLauS chip which can be adjusted to the application of scintillation light readout by selecting a suited charge integration stage. In the long term, PETsys Electronics is developing a new version of the TOFPET ASIC called TOFPET v3 which is announced to have an increased dynamic range capable of handling larger charge measurements.

The 3×3 Hamamatsu SiPM has shown a saturation level even below the saturation level of the ASIC due to its small number of SPADs. Thus it is not suitable for the SCoKa absorption layer. However, the Hamamatsu SiPM array has given rise to the opportunity to already study the data grouping process for a signal that is spread out over multiple SiPM channels and analyse the ToA of the scintillation light signals. A coincidence time of 10 ns was found to be suitable for data grouping.

Performing DOI measurements using a double-sided SiPM readout method is currently not practical due to the bad resolution of the DOI measurement and since this method would double the amount of SiPMs and readout channels in the absorption layer. The main issues are currently unequally well polished scintillator faces on both ends and an electron beam that is not collimated narrow enough. However, a better resolution was reported from other groups with similar setups and a better result is expected to be obtained in future measurements.

6 | Summary and Future Outlook

In this thesis, hardware components for the construction of a Compton camera prototype capable of an imaging for photon energies above 1 MeV have been characterised and compared. An offline and an online method for the readout of SiPM signals could be established. The noise behaviour of possible SiPM products was investigated with charge spectra, inter-time distributions and staircase plots. The operating bias voltage of the 2×2 Broadcom SiPM was optimised for the detection of Cherenkov light by evaluating efficiency measurements with LEDs. An optimal bias was found to be around 40 V. Comparative measurements for different scintillators have been performed studying the light output, decay constant and energy resolution. Systems out of scintillator, SiPM and readout ASIC were used to conduct energy calibrations and investigate the saturation behaviour of the hardware components. The Hamamatsu SiPM array was used to study the ToA of the scintillation light signal and run first test for the grouping process of measurements for light signals that are spread over multiple SiPM channels. A coincidence time window of 10 ns was identified. Lastly, DOI measurements using a double-sided SiPM setup have been carried out as well.

Promising hardware components for the construction of the SCoKa device could be identified. The SiPM matrix of the scattering layer can be constructed with the 2×2 Broadcom SiPMs. LGSO and GAGG crystals coupled to the 4×4 Broadcom SiPM and read out by the TOFPET ASIC are suitable for the construction of the absorption layer.

Next steps towards the construction of a prototype would involve characterising test measurements with the KLauS chip. A SiPM plane needs to be constructed step by step using the 2×2 Broadcom SiPMs. Currently a matrix of 20×20 SiPMs in the final version of the scattering layer is planned. It is advisable to start with smaller matrix sizes, e.g. a 3×3 matrix, to run first tests with the KLauS chip and then enlarge the matrix gradually to implement a synchronisation of multiple readout chips and evaluate whether the performance of the chip is influenced by the number of equipped SiPM channels.

For the absorption layer, DOI measurements have to be repeated under improved conditions. Other scintillator crystals such as a ceramic version of the GAGG crystal could be investigated. The performance of the KLauS chip for the readout of scintillation light has to be compared with the performance of the TOFPET ASIC discussed in this thesis. Based on these further measurements, a design for two absorber blocks has to be developed.

Once the scattering layer is constructed, it can already be tested. A collimated β-emitter can be used to radiate electrons onto the PMMA and validate the reconstruction of the Cherenkov cone which is the innovative heart of the SCoKa project.
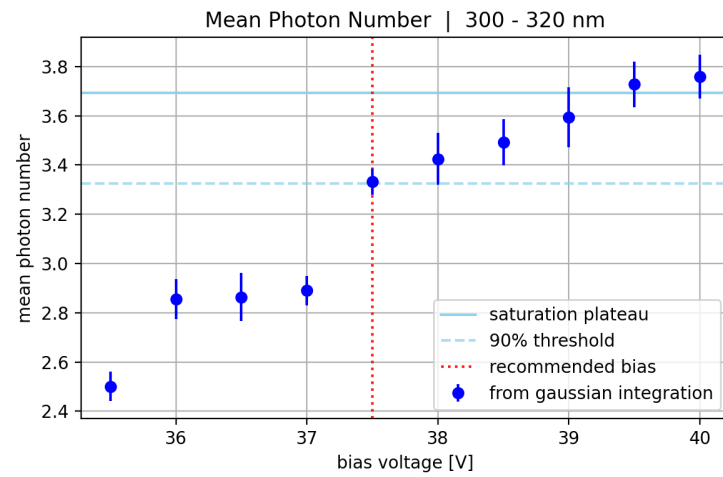
A | Appendix

A.1 LED Measurements

Figure A.1: Mean detected photon number against the bias voltage for the UV_3 LED. See section 4.5 for more information.
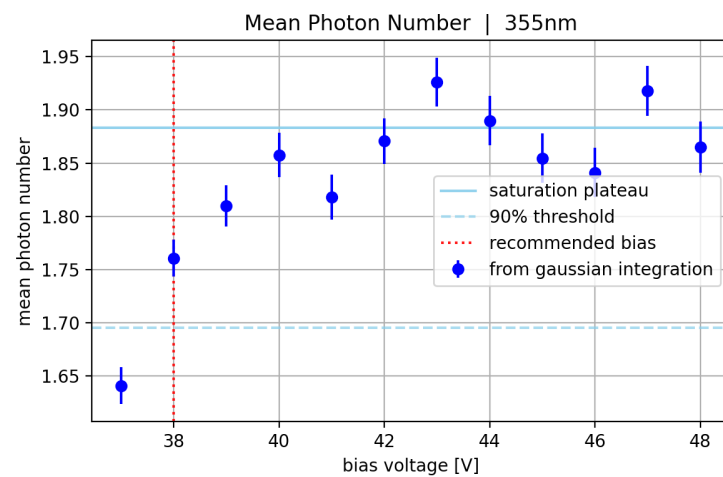

Figure A.2: Mean detected photon number against the bias voltage for the UV_2 LED. See section 4.5 for more information.
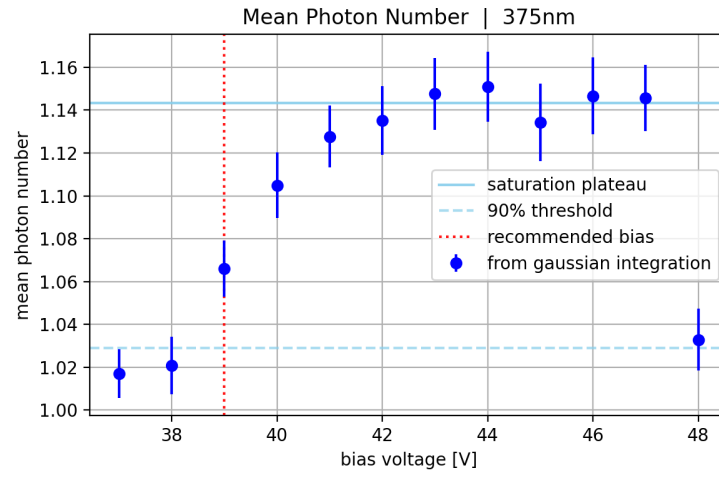
Figure A.3: Mean detected photon number against the bias voltage for the UV$_1$ LED. See section 4.5 for more information.
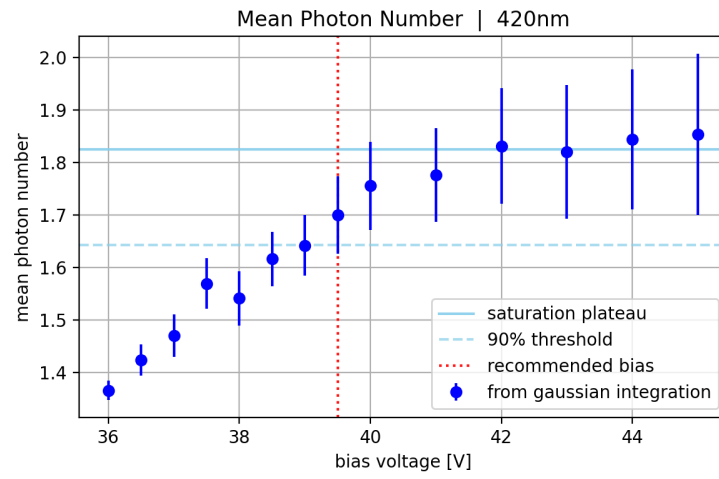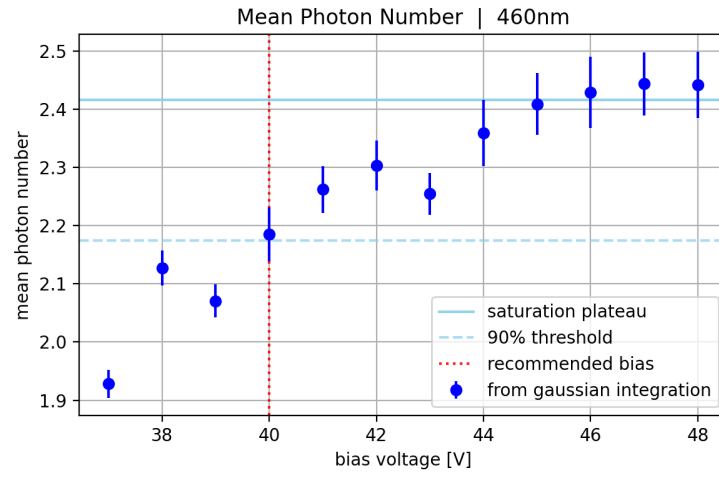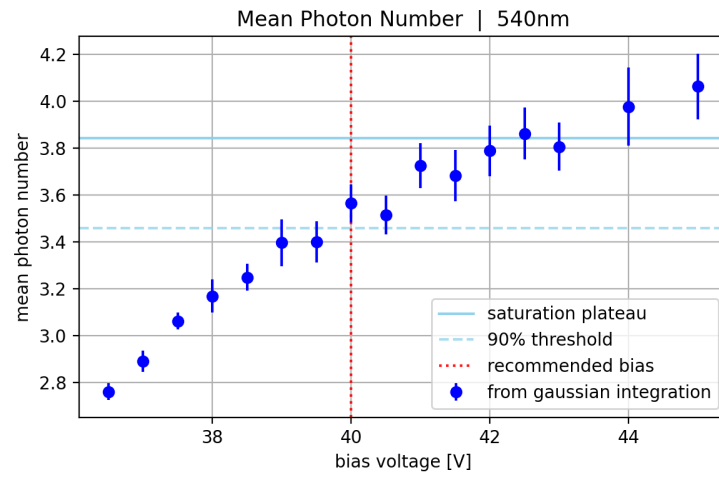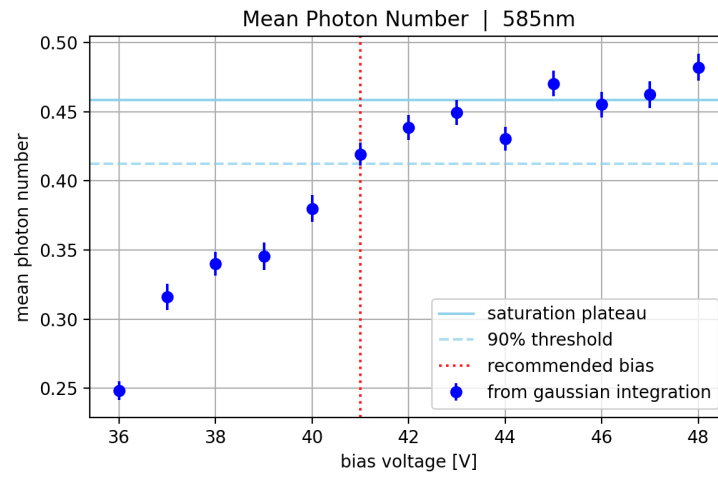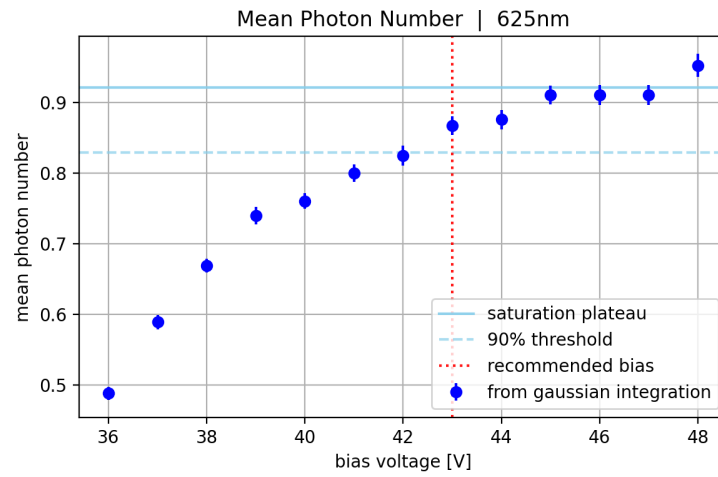

Figure A.4: Mean detected photon number against the bias voltage for the NUV LED. See section 4.5 for more information.

Figure A.5: Mean detected photon number against the bias voltage for the blue LED. See section 4.5 for more information.

Figure A.6: Mean detected photon number against the bias voltage for the green LED. See section 4.5 for more information.

Figure A.7: Mean detected photon number against the bias voltage for the amber yellow LED. See section 4.5 for more information.

Figure A.8: Mean detected photon number against the bias voltage for the red LED. See section 4.5 for more information.

A.2 Source Measurements
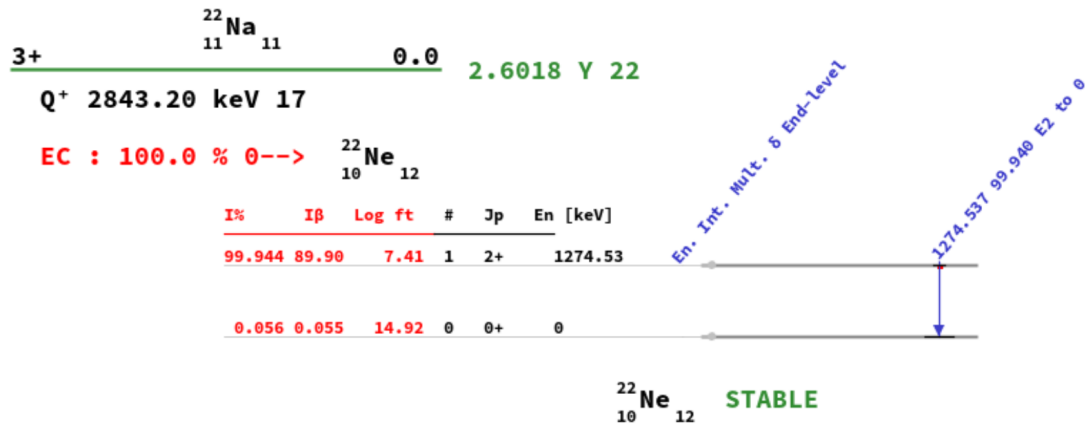
Figure A.9: Decay scheme of ^{22}Na [33]. See section 5.1.2 for more information.
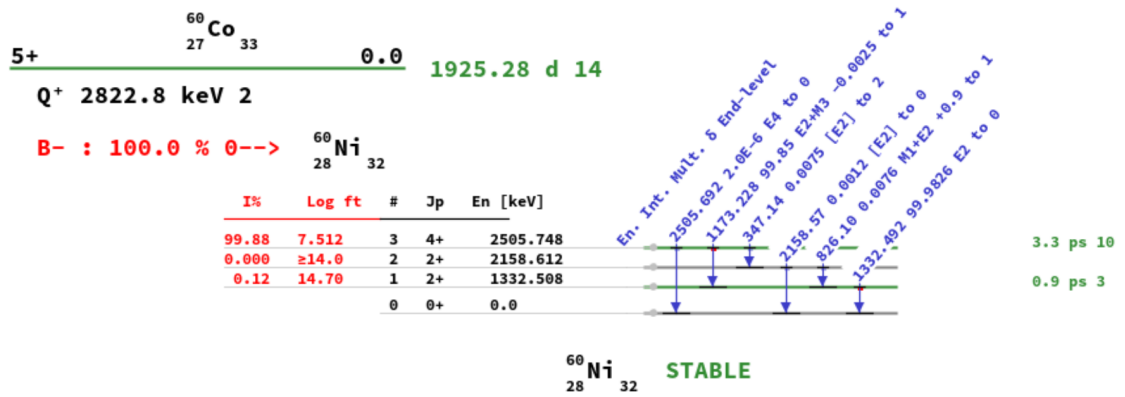
Figure A.10: Decay scheme of ^{60}Co [33]. See section 5.1.3 for more information.
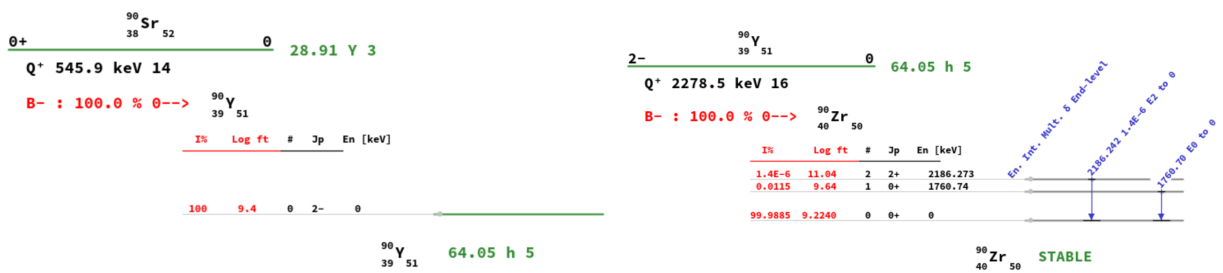
Figure A.11: Decay scheme of ^{90}Sr and the daughter isotope ^{90}Y [33]. See section 5.1.4 for more information.
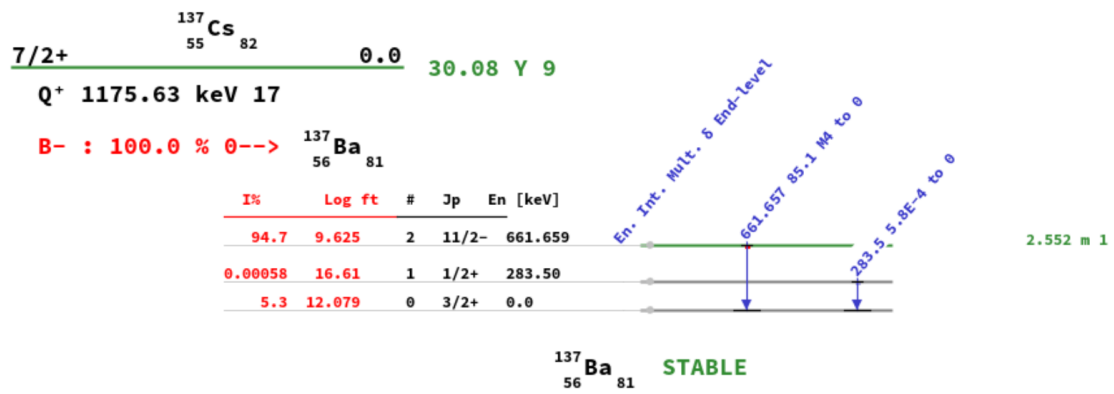
Figure A.12: Decay scheme of [137]Cs [33]. See section 5.1.5 for more information.
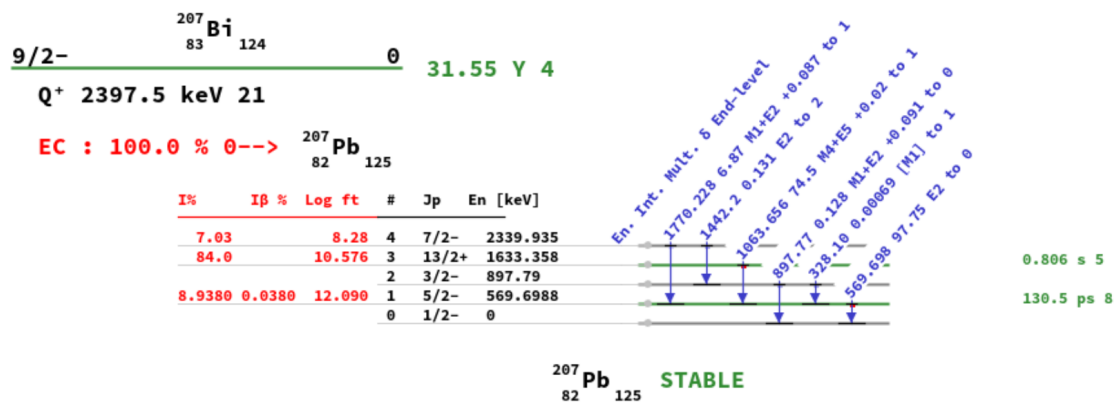
Figure A.13: Decay scheme of [207]Bi [33]. See section 5.1.6 for more information.

Bibliography

[1] Claus Grupen and Boris Shwartz. *PARTICLE DETECTORS*. Cambridge University Press, 2nd edition, 2008. ISBN 978-0-521-84006-4.

[2] Fabio Sauli. *Gaseous Radiation Detectors - Fundamentals and Applications*. Cambridge University Press, 2014. ISBN 978-1-107-04301-5.

[3] Hermann Kolanoski, Norbert Wermes. *Particle Detectors - Fundamentals and Applications*. Cambridge University Press, 2020. ISBN 978–0–19–885836–2.

[4] Reimund Bayerlein. *Coincident Detection of Cherenkov Photons for Medical Applications*. PhD thesis, Universität Siegen, 2020. Available at https://www.hep.physik.uni-siegen.de/pubs/diss/bayerlein-dr.pdf.

[5] D. Renker, E. Lorenz. Advances in solid state photon detectors. *IOP Publishing*, April 2009. Available at https://iopscience.iop.org/article/10.1088/1748-0221/4/04/P04004.

[6] Stefan Gundacker, Arjan Heering. The silicon photomultiplier: fundamentals and applications of a modern solid-state photon detector. *IOP Publishing*, 2020. Available at https://iopscience.iop.org/article/10.1088/1361-6560/ab7b2d.

[7] Orlando Soto, Rimsky Rojas, Sergey Kuleshov, Hayk Hakobyan, Alam Toro, William K. Brooks. Characterization of novel Hamamatsu Multi Pixel Photon Counter (MPPC) arrays for the GlueX experiment. *ELSEVIER*, June 2013. Available at https://www.sciencedirect.com/science/article/pii/S0168900213009042?via%3Dihub.

[8] Patrick Eckert, Hans-Christian Schultz-Coulon, Wei Shen, Rainer Stamen, Alexander Tadday. Characterisation studies of silicon photomultipliers. *ELSEVIER*, January 2010. Available at https://www.sciencedirect.com/science/article/pii/S0168900210008156?via%3Dihub.

[9] Broadcom. *AFBR-S4XX Brief Introduction to Silicon Photomultipliers*, 2024. Available at https://www.aptechnologies.co.uk/images/Data/Broadcom/SiPMs/AN101_AFBR-S4XX_BriefIntroToSiPMs_29Jan24.pdf.

[10] PETsys Electronics, Oeiras, Portugal. *TOFPET2: a high-performance ASIC for time and amplitude measurements of SiPM signals in time-of-flight applications*. Available at https://www.petsyselectronics.com/web/website/docs/products/product1/TOFPET2_Overview.pdf.

[11] R. Bugalho, A. Di Francesco, L. Ferramacho, C. Leong, T. Niknejad, L. Oliveira, M. Rolo, J. C. Silva, R. Silva, M. Silveira, S. Tavernier, J. Varela. Experimental characterization of the TOFPET2 ASIC. Technical report, LIP, PETsys Electronics, DEE, CTS-UNINOVA FCT-UNL, INFN, Vrije Universiteit Brussel, 2019. Available at https://www.petsyselectronics.com/web/website/docs/products/product1/TOFPETv2%20characterization%20paper.pdf.

[12] PETsys Electronics, Oeiras, Portugal. *PETsys TOFPET 2C ASIC - Datasheet*. rev. 16.

[13] Susan Dean and Barbara Illowsky, adapted by Riyanti Boyd and Natalia Casper. *INTRODUCTORY STATISTICS*. OpenStax College, 4th edition, 2021.

[14] Sikandar Shaikh. PET-CT Imaging and Applications. *IntechOpen*, April 2022. Available at `https://www.researchgate.net/publication/360062996_PET-CT_Imaging_and_Applications`.

[15] R. W. Todd, J. M. Nightingale, D. B. Everett. A proposed γ camera. *Nature*, September 1974. Available at `https://www.nature.com/articles/251132a0`.

[16] Daisuke Matsuura, Kei Genba, Yoshikatsu Kuroda, Hiroshi Ikebuchi, Tetsuya Tomonaka. "ASTRO-CAM 7000HS" Radioactive Substance Visualization Camera. Technical report, Mitsubishi Heavy Industries, Ltd., 2024. Available at `https://www.mhi.co.jp/technology/review/pdf/e511/e511068.pdf`.

[17] Shin Watanabe, Hiroyasu Tajima, Yasushi Fukazawa, Yuto Ichinohe, Shin'ichiro Takeda, Teruaki Enoto, Taro Fukuyama, Shunya Furui, Kei Genba, Kouichi Hagino, Atsushi Harayama, Yoshikatsu Kuroda, Daisuke Matsuura, Ryo Nakamura, Kazuhiro Nakazawa, Hirofumi Noda, Hirokazu Odaka, Masayuki Ohta, Mitsunobu Onishi, Shinya Saito, Goro Sato, Tamotsu Sato, Tadayuki Takahashi, Takaaki Tanaka, Atsushi Togo, Shinji Tomizuka. The Si/CdTe semiconductor Compton camera of the ASTRO-H Soft Gamma-ray Detector (SGD). *arXiv*, September 2015. Available at `https://arxiv.org/abs/1509.00588`.

[18] J. Kataoka, A. Kishimoto, T. Nishiyama, T. Fujita, K. Takeuchi, T. Kato, T. Nakamori, S. Ohsuka, S. Nakamura, M. Hirayanagi, S. Adachi, T. Uchiyama, K. Yamamoto. Handy Compton camera using 3D position-sensitive scintillators coupled with large-area monolithic MPPC arrays. *ELSEVIER*, 2013. Available at `https://www.sciencedirect.com/science/article/pii/S0168900213009947`.

[19] Christian Lang. *Design of a Compton camera for medical imaging and characterization of its components*. PhD thesis, Ludwig-Maximilians-Universität München, 2015. Available at `https://edoc.ub.uni-muenchen.de/18918/`.

[20] A. Takada, K.Hattori, H.Kubo, K.Miuchi, T. Nagayoshi, H.Nishimura, Y. Okada, R. Orito, H. Sekiya, A. Takeda, T. Tanimori. Development of an advanced Compton camera with gaseous TPC and scintillator. *arXiv*, October 2018. Available at `https://arxiv.org/abs/astro-ph/0412047`.

[21] Y. Yoshihara, K. Shimazoe, Y. Mizumachi, H. Takahashi, K. Kamada, A. Takeda, T. Tsuru, Y. Arai. Development of electron-tracking Compton imaging system with 30-μm SOI pixel sensor. *IOP Publishing*, January 2017. Available at `https://iopscience.iop.org/article/10.1088/1748-0221/12/01/C01045`.

[22] T. E. Peterson, A. B. Brill, A. H. Walenta. High Energy Gamma-Ray Imaging Using Cherenkov Cone Detection - A Monte Carlo Study with Application to a Compton Camera System. *IEEE*, 2013. Available at `https://ieeexplore.ieee.org/document/6551741`.

[23] Konrad Briggl, Wei Shen, Tobias Harion, Rene Hagdorn, Patrick Eckert, Thorwald Klapdor-Kleingrothaus, Markus Dorn, Hans-Christian Schultz-Coulon. Characterization results and first applications of KLauS - an ASIC for SiPM charge and fast discrimination readout. *IEEE*, 2014. Available at `https://ieeexplore.ieee.org/document/6829778`.

[24] Broadcom. *AFBR-S4N22P014M NUV-MT Silicon Photomultiplier Array*, 2024. Available at `https://www.broadcom.com/products/optical-sensors/silicon-photomultiplier-sipm/afbr-s4n22p014m`.

[25] Broadcom. *AFBR-S4N44P014M NUV-MT Silicon Photomultiplier*, 2024. Available at `https://www.broadcom.com/products/optical-sensors/silicon-photomultiplier-sipm/high-performance-sipm-nuv-mt/afbr-s4n44p014m`.

[26] Broadcom. *AFBR-S4N66P014M NUV-MT Silicon Photomultiplier*, 2023. Available at https://www.broadcom.com/products/optical-sensors/silicon-photomultiplier-sipm/high-performance-sipm-nuv-mt/afbr-s4n66p014m.

[27] Hamamatsu. *MPPC (multi-pixel photon counter) - S13360 series*, 2024. Available at https://www.hamamatsu.com/content/dam/hamamatsu-photonics/sites/documents/99_SALES_LIBRARY/ssd/s13360_series_kapd1052e.pdf.

[28] Broadcom. *AFBR-S4NXX SiPM Waveform and Bandwidth Consideration Version 1.0*, 2023. Available at https://docs.broadcom.com/doc/AFBR-S4NXX-AN.

[29] Fabio Acerbi, Giovanni Paternoster, Massimo Capasso, Marco Marcante, Alberto Mazzi, Veronica Regazzoni, Nicola Zorzi, Alberto Gola. Silicon Photomultipliers: Technology Optimizations for Ultraviolet, Visible and Near-Infrared Range. *MDPI Instruments*, December 2018. Available at https://www.researchgate.net/publication/331070642_Silicon_Photomultipliers_Technology_Optimizations_for_Ultraviolet_Visible_and_Near-Infrared_Range.

[30] OXIDE. *LGSO - Key Scintillator Materials for Novel Radiation Detectors*, 2021. Available at https://www.opt-oxide.com/en/products/lgso/.

[31] Epic-Crystal. *GAGG(Ce) Crystal*, 2023. Available at https://www.epic-crystal.com/scintillation-crystals/gaggce-crystal.html.

[32] Saint-Gobain Crystals, 17900 Great Lakes Parkway, Hiram, OH, 44234, US. *Detector Assembly Materials*, 2016. Available at https://seltokphotonics.com/upload/iblock/25e/25e2f99e5cdd45cb8e87748ed840eeb3.pdf.

[33] IAEA - International Atomic Energy Agency. Live Chard of Nuclides - nuclear structure and decay data, March 2025. https://www-nds.iaea.org/relnsd/vcharthtml/VChartHTML.html.

[34] Nagomi Uchida, Hiromitsu Takahashi, Masanori Ohno, Tsunefumi Mizuno, Yasushi Fukazawa, Masao Yoshino, Kei Kamada, Yuui Yokota, Akira Yoshikawa. Attenuation characteristics of a Ce:$Gd_3Al_2Ga_3O_{12}$ scintillator. *ELSEVIER*, 2021. Available at https://www.sciencedirect.com/science/article/pii/S0168900220311220.

[35] Lisa Lopez, Pierre Pichon, Pascal Loiseau, Bruno Viana, Rachid Mahiou, Frederic Druon, Patrick Georges, François Balembois. Ce:LYSO, from scintillator to solid-state lighting as a blue luminescent concentrator. *Nature*, May 2023. Available at https://www.nature.com/articles/s41598-023-32689-z.

[36] Daiki Nobashi, Kazutaka Yamaoka, Hiroyasu Tajima, Kazuya Ito. Performance evaluation of GAGG(Ce)/LFS scintillator + MPPC array readout with ASIC. *arXiv*, September 2021. Available at https://arxiv.org/abs/2109.07362.

[37] John Barrio, Neus Cucarella, Marta Freire, Efthymios Lamprou, Sergio Aguilar, Celia Valladares, Victor Ilisie, Jose M. Benlloch, Antonio J. Gonzalez. PET Detector based on a Semi-Monolithic Crystal with DOI and TOF Capabilities. *IEEE*, 2020. Available at https://ieeexplore.ieee.org/document/9508047.

Acknowledgements

Erklärung

Ich versichere, dass ich die schriftliche Ausarbeitung selbständig angefertigt und keine anderen als die angegebenen Hilfsmittel benutzt habe. Alle Stellen, die dem Wortlaut oder dem Sinn nach (inkl. Übersetzungen) anderen Werken entnommen sind, habe ich in jedem einzelnen Fall unter genauer Angabe der Quelle (einschließlich des World Wide Web sowie anderer elektronischer Datensammlungen) deutlich als Entlehnung kenntlich gemacht. Dies gilt auch für angefügte Zeichnungen, bildliche Darstellungen, Skizzen und dergleichen. Ich nehme zur Kenntnis, dass die nachgewiesene Unterlassung der Herkunftsangabe als versuchte Täuschung gewertet wird.

_____-   _____-
           Ort, Datum   Unterschrift